# Applications of the sol-gel method for the synthesis of novel catalytic materials

Ph.D. Thesis

Ákos Kukovecz

UNIVERSITY OF SZEGED

2001

TABLE OF CONTENTS 2

1. INTRODUCTION 4

2. CONCEPTUAL BACKGROUND 7

2.1 The sol-gel method 7
2.1.1 History 7
2.1.2 How does it work? 8
2.1.3 Controlling the properties of the gel 11
2.1.4 Applications 13

2.2 Morphology in heterogeneous catalysis 14

2.3 Reactions of interest 15
2.3.1 Carbon nanotube synthesis 15
2.3.2 Diels-Alder type reactions 16

3. EXPERIMENTAL 17

3.1 Synthesis 17
3.1.1 Mesoporous materials 17
3.1.2 Macroporous materials 19

3.2 Characterisation 20
3.2.1 Elemental analysis 20
3.2.2 Sample features on the molecular scale 20
3.2.3 Acidity 21
3.2.4 Electron microscopy 22
3.2.5 Adsorption behaviour 22
3.2.6 Effects of mechanical pressure 22

3.3 Catalytic experiments 22
3.3.1 Synthesis of carbon nanotubes 22
3.3.2 Isomerisation of 1-butene 23
3.3.3 Diels-Alder reactions 23

3.4 Computational methods 24

3.4.1 Pore structure characterisation 24
3.4.2 Calculation of the fractal dimension 26
3.4.3 Quantum chemical calculations 27
3.4.4 Statistical background 27

**4. RESULTS AND DISCUSSION 28**

**4.1 Mesoporous materials 28**
4.1.1 Materials containing transition metals 28
4.1.2 Materials containing phosphotungstic acid 36

**4.2 Macroporous materials 55**
4.2.1 Silica nanotubes 55
4.2.2 Silica foams 61

**4.3 General considerations concerning fractal dimension 68**

**5. SUMMARY 71**

**6. ACKNOWLEDGEMENT 73**

**7. REFERENCES 74**

**8. APPENDIX 78**

## 1. INTRODUCTION

Ever since the very beginnings of modern chemistry, heterogeneous catalysis has always been a major driving force of development, because it was a discipline that helped to satisfy the needs of the masses and could improve the general quality of human life. By as early as the 1820s, over a million items were sold from the first commercial heterogeneous catalytic instrument, Döbereiner's "tinderbox" — a device that was used for lighting a flame by directing a jet of hydrogen from a miniature Kipp's apparatus onto a platinum sponge. In the 1850s, Phillips patented the use of platinum for oxidising $SO_2$ to $SO_3$ with air. In 1871, the Deacon process was developed for the oxidation of HCl to $Cl_2$ over a clay brick impregnated with cupric salts. In the last decades of the 19$^{th}$ century the basics of catalytic hydrogenation over metallic nickel had been worked out by Sabatier, Normann and Mège-Mouries. Ostwald realised that ammonia could be catalytically oxidised into oxides of nitrogen (which can then be turned into nitric acid) over a platinum gauze in 1903.

A landmark in the history of applied catalysis is 1909, when Haber succeeded in finding an adequate catalyst (later to be perfected by Bosch and Mittasch) for the synthesis of ammonia from $N_2$ and $H_2$ [1]. This discovery can be regarded as the origin of modern, conscious catalyst design and development. In 1923 the first synthetic methanol plant operating with zinc oxide — chromium oxide catalyst was commissioned. Shortly afterwards, the cobalt and iron catalysts of the Fischer-Tropsch process were developed. The 1930s brought the selective, silver-catalysed oxidation of ethylene, the first catalytic cracking plants using acid-treated montmorillonite, and the introduction of "silico-phosphoric acid" by Ipatieff and Pines. The career of synthetic zeolites skyrocketed after World War II thanks to the work of Rabo, Milton, Barrer, Plank, Hall and many other researchers. Further important achievements of the last few decades are precisely planned bifunctional catalysts, sulphur and nitrogen tolerant catalysts, three-way automotive exhaust catalysts, asymmetric catalysis, immobilised enzymes etc. All in all, heterogeneous catalysis has always been about finding, or even better, designing new materials that are able to speed up the reactions considered to be important by the contemporary chemical industry.

The present day is no exception, of course. One of the current focuses of interest is catalysis in the mesoporous range. Albeit zeolites usually make splendid catalysts for reactions where the kinetic diameter of the partners does not exceed 8-10 Å, they fail to operate on molecules whose primary size is 10-20 Å (and more). This is a serious handicap, as the attention of the industry is slowly turning towards larger molecules partially because of necessity (as oil reserves run low, bigger and bigger molecules have to be processed into

motor fuels) and partially because they open new fields of application (e.g. stereoselective catalytic reactions without size limitations). Even though the discovery of the M41S type of materials in 1992 [2] promised a quick solution to the pore size problem, the scientific community is not content and is constantly looking for new routes to prepare tailor-made mesoporous catalysts.

The term "sol-gel method" refers to the controlled hydrolysis of soluble metal sources (primarily alkoxides). During the reaction the system is transformed from a real solution into a three dimensional solid structure, while passing through numerous stages of aggregation. Originally a technique known to the ceramics industry, the sol-gel method was re-discovered by heterogeneous catalysis in the 1980s. The process witnessed an enormous increase in popularity in the 1990s and is considered to be one of the leading new synthesis methods of the discipline. The main reason for such an expansion is that the sol-gel keyword is "versatility". Catalyst morphology, porosity and functionality can all be varied quasi independently to a considerable extent and with admirable simplicity. Therefore, many researchers pondering over the difficulties mentioned in the previous paragraph find that sol-gel derived materials may possess just the type of features they were looking for.

Nowadays, the main important and challenging goal of heterogeneous catalysis is to approach 100 % selectivity, practically irrespective to the conversion level. Billions of dollars are invested into the investigations of nanostructured metal catalysts possessing metals in nanometer sized homodisperse distribution. These catalysts are expected (i) to exhibit a uniform catalytic behaviour resulting in 100 % selectivity, and (ii) to speed up the development of sophisticated analytical methods and instruments to assure the precise analysis of the products of such transformations.

The present dissertation describes my experiences with synthesising, characterising and testing sol-gel derived meso- and macroporous functionalised silica composites. As the technique was completely unknown to our research group prior to my work, it was my goal to find as many connections between the offerings of the sol-gel technique and the needs of our Department as I could. Therefore, this PhD thesis is constructed as a loosely linked system of smaller projects sharing two common features: (i) they all investigate certain properties of silica-based composite materials, and (ii) they are designed with the global research interests of our group in mind.

The following areas were investigated in particular:

- controlling the porosity of the material by preparing mesoporous silica, silica nanotubes and silica foams,
- functionalising the material by building transition metals, heteropoly acid molecules or structural aluminum into it,
- testing the activity of the prepared catalysts in the reactions of carbon nanotube synthesis, 1-butene isomerisation and a Diels-Alder type cycloaddition.

I trust that my work has helped to pinpoint the areas of sol-gel based heterogeneous catalysis that are worth exploring in more detail as long term research projects in the future.

# 2. CONCEPTUAL BACKGROUND

## *2.1 The sol-gel method*

Sol-gel processing has become so popular in the last few decades that writing a compact yet comprehensive introduction to the subject is as easy a task as summarising inorganic chemistry in two pages. Therefore, the following Sections do not even attempt to do so. My primary goal is just to give a quick overview of the field, especially about the topics related to my PhD research.

### 2.1.1 History

Interest in the sol-gel processing of inorganic ceramic and glass materials began as early as the mid-1800s with Ebelmen's [3] and Graham's [4] studies on silica gels. These early investigators observed that the hydrolysis of tetraethyl orthosilicate under acidic conditions yielded $SiO_2$ in the form of a "*glass-like material*". Unfortunately, little technological interest was raised by these studies due to the extremely long drying times required to obtain large monolithic pieces. Gels regained the attention of chemists for a period from the late 1800s through the 1920s because of the phenomenon of Liesegang rings [5], investigated by as noted researchers as Ostwald and Lord Rayleigh. Despite the huge volume of descriptive literature published about these studies, the physical-chemical properties of gels were only sparsely understood.

The second renaissance of the technique came through the work of Roy and co-workers [6] who recognised the potential for achieving very high levels of chemical homogeneity in colloidal gels. They established the place of the sol-gel method in the arsenal of the ceramic industry in the 1950s and 1960s by synthesising a large number of novel ceramic oxide compositions (Al, Si, Ti, Zr, etc.) unavailable by traditional ceramic powder methods.

The third boom came in the 1980s, when the sol-gel method was rediscovered by the micro-optical and heterogeneous catalytic industry. Outstanding versatility, excellent control over the properties of the material and very high and homogeneous component distribution were the key factors responsible for the exponential gain in popularity. This phenomenon is indicated by the increase in the number of registered U.S. patents utilising sol-gel elements, as depicted in Figure 1.

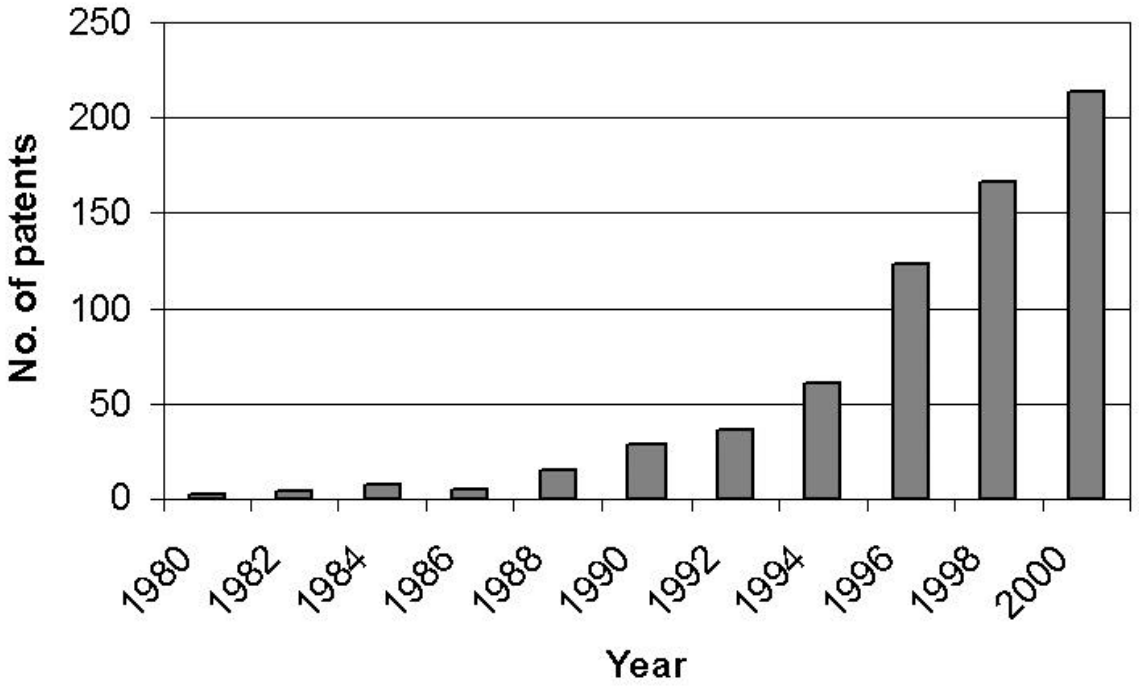


Figure 1. Number of annually registered U.S. patents related to the sol-gel method

Currently, the sol-gel method is utilised by more disciplines of science [7] then ever before. Optics [8], electronics [9], biotechnology [10], the drug industry [11] and of course, heterogeneous catalysis [12] are continuously finding novel possible applications — most of which are based on the capacity of the technique to build complex, multicomponent systems in one single step. As Ward and Ko summarise in [12]: *"We see the following specific advantages: (i) the ability to control structure and composition at the molecular level, (ii) the ability to introduce several components in a single step, (iii) the ability to impose kinetic constraints on a system and thereby stabilize metastable phases, and (iv) the ability to fine tune the activation behavior of a sample and thereby trace the genesis of active species."*

### 2.1.2 How does it work?

*Sols* are dispersions of colloidal particles in a liquid. A *gel* is an interconnected, rigid network with pores of submicrometer dimensions and polymeric chains whose average length is greater than a micrometer [13]. In the most general sense of the word, the term "*sol-gel method*" can refer to any synthesis that begins with a liquid state (real or colloidal solution) and ends up with a gel phase. Because of their immense effect on the properties of the final material, post-synthetic treatment procedures like ageing, drying, hydrothermal treatment,

calcination etc. of the gel are usually bundled with the real "sol-to-gel" process parameters in the dictionary of most authors.

Two approaches are used to make sol-gel monoliths: (i) gelation of a solution of colloidal powders, (ii) hydrolysis and polycondensation of a real solution of nitrate or alkoxide precursors followed by ageing and drying. Supercritical drying yields aerogels, while drying at ambient conditions yields xerogels (also called alcogels, if the major solvent removed from the gel was some sort of alcohol). All samples mentioned in this thesis are alcogels prepared by the controlled hydrolysis of alkoxide precursors, therefore, only this route shall be detailed below.

Alkoxide based sol-gel chemistry can be described by the two (oversimplified, yet demonstrative) reactions presented in Scheme 1.

Hydrolysis: $\text{—MOR} + H_2O \rightarrow \text{—MOH} + \text{ROH}$

Condensation: $\text{—MOR} + \text{ROM} \rightarrow \text{—MOM—} + \text{ROH}$

or: $\text{—MOH} + \text{HOM} \rightarrow \text{—MOM—} + H_2O$

Scheme 1. The two classes of reactions governing the alkoxide based sol-gel process

In my studies M was Si, Al or Ti and R was ethyl or isopropyl group. All reactions were performed under acidic conditions, except the silica nanotube synthesis which was catalysed by adding $NH_3$ solution to the system.

Two models for the $Si(OR)_4$ hydrolysis reaction have been proposed, one in which a trivalent [14] and another in which a pentavalent [15] transition state is assumed. The latter has been found to be correct by the high-pressure Raman spectroscopic studies of Zerda and Hoang [16]. They suggest that in the case of the acid catalysed hydrolysis of $Si(OCH_3)_4$ the proton is attracted by the oxygen atom of the $OCH_3$ group as illustrated in Scheme 2.

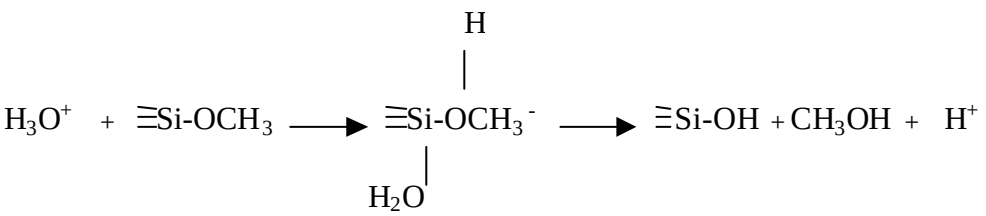


Scheme 2. Acid catalysed hydrolysis of $Si(OCH_3)_4$ *via* a pentavalent transition state [16]

This causes a shift of the electron cloud of the Si-O bond toward the oxygen, thus the positive charge on the Si increases. The pentavalent state is formed by a nucleophilic attack of a water molecule, and the system stabilises itself by releasing methanol and the catalysing proton.

Gelation (a series of condensation steps leading to a three dimensional interconnected structure) is the most important factor governing the features of the final product. Three different gelation theories are commonly recited regarding sol-gel processes:

- Classical of mean-field theory

Developed by Flory [17], this model visualises the basis structure of a polymer as a tree (Cayley tree or Bethe lattice). The maximum number of bonds allowed to form at each node is a pre-defined value (e.g. 4 for silicic acid) for each polymer family. Clusters grow in a random, branching, but essentially linear fashion. This is ensured by the condition that requires at least two bonds per node so that the cluster remains continuously connected from one side to the other. Though this model is appealing at a first glance and makes it possible to calculate important parameters like the distribution of molecular weights, it has a fatal flaw in it. Because no rings are allowed, there is an increasing number of nodes as the radius of the cluster increases. The direct consequence of this error is that the model predicts that the mass of such clusters should increase as the fourth power of the radius, instead of the real-life behaviour where mass must grow as the third power of cluster radius.

- Perlocation theory

Perlocation theory has been recently reviewed by Zallen [18]. Perlocation allows for rings or closed loops to form, and thus the mass of perlocation models increases correctly, with the cube of the cluster radius. The simplest site perlocation model starts with an empty grid and puts particles randomly at the intersections. If two particles are adjacent, then bonding will occur. The flaw of this model is that complete connectivity or gelation is rather unlikely at rational values of site filling. The so-called bond perlocation model corrects this problem by starting with all intersections filled and adding the bonds randomly. This model is dependent on the lattice (threshold values were summarised by Brinker and Scherer [7], but is capable to provide accurate predictions within its own limits.

- Fractal theory

The idea of fractality (or self-similarity) was introduced by Mandelbrot [19], and has been applied very successfully in as distant areas of science as modelling the growth of trees [19] and modelling the surface of the Sun [20]. One fractal gelation model was developed by Keefer [21]. Clusters simulated with this model retain the desirable branching, self-similar structure of the classical gelation theory, but compensate its major flaw by postulating that the

density of mass fractals decreases with size. All in all, the model gives a range of fractal dimension values from 1.6 to 2.4 depending on the rate of hydrolysis, which relates well with published experimental results. Besides its applicability to modelling gelation, the fractal approach has proven to be a most useful tool in describing certain surface properties of the synthesised gels as well (see Sections 2.2 and 4.3).

### 2.1.3 Controlling the properties of the gel

Sol-gel science being such a broad field, the topic of this Section should cover at least four distinct areas:

- Controlling the pore structure, specific surface area, micropore volume etc.
- Controlling the elemental composition of the gel. Possibilities of incorporating metal, metal-oxide and non-metal functional modifiers, changing acidity etc.
- Controlling the morphology of the product. Synthesis of monolithic pieces, spheres, layers, coverings, foams, membranes etc.
- Regulating macroscopic properties like opacity, density, fracture resistance etc.

The first of these is the point of the present Section, the second shall be discussed in the next Section and the third area is to be summarised in Section 2.2. Questions related to the control over macroscopic properties are clearly out of the scope of this thesis.

The novice investigator is easily discouraged by the apparent complexity of the problem of tailoring the pore volume and specific surface area of even a simple, single-component $SiO_2$ matrix. Temperature, pressure, pH, water-to-Si ratio, time, ageing, drying etc. all seem to be important yet counter-acting factors governing the properties of the final product. Curiously enough, the theory determining sol-gel pore characteristics is really quite simple: it's all about the hydrolysis and condensation reactions. Fast condensation leads to compact, dense, low-area structures, while fast hydrolysis accompanied by moderate condensation speed results in open, irregular, porous matrices. Any of the synthesis parameters may act as an effective modifier factor as long as it is able to change the absolute and/or relative rates of these two competing reactions.

Recently, Jones *et al.* have performed a comprehensive study [22] on the dependence of pore characteristics on the preparation conditions of sol-gel derived aluminosilicates. Their method was to take a default TEOS-based acid catalysed hydrolysis reaction, and synthesise a series of gels changing one parameter a time. Their findings can be summarised as follows:

- Increasing the Al-to-Si ratio, the solvent (ethanol) content or the pH results in a decrease in the specific surface area of the products. Increasing the $H_2O$-to-Si ratio, on the other hand, results in higher BET surfaces.
- Porosity and total pore volume change in line with the BET surface. However, micropore volume seems to follow the opposite trend: the lower the surface area, the higher the contribution of micropores to the total pore volume.
- Increasing the size of the alkyl group of the solvent alcohol or the number of –OH groups per molecule increases the BET area, pore volume and porosity, but decreases the micropore volume.

In a comprehensive study on the properties of titanosilicates prepared by various synthesis techniques, Toba *et al.* [23] have found that the complexing agent (in their case, 1,6-hexanediol) assisted sol-gel method gave the most homogeneous samples and offered (chiefly *via* changing the Ti/Si ratio) the biggest control over pore system characteristics.

When a gel is maintained in its pore liquid, its structure and properties continue to change long after the gel point. This process is called ageing. Four processes can occur during ageing: polycondensation, syneresis (shrinkage of the gel accompanied by the expulsion of liquid from the gel pores), coarsening and phase transformation. Albeit there is plenty of literature on ageing [24], the details of the process are scarcely understood, and the optimisation of the ageing parameters of the sol-gel synthesis has not advanced far beyond the trial-and-error level.

The next step in the course of the synthesis is drying, which can be done either under supercritical conditions or at elevated temperatures (or decreased pressures). The former method leads to xerogels, the latter to alcogels (if the original solvent was alcohol, aerogels otherwise). Smith *et al.* have discovered [25] a co-operative effect between the synthesis pH and the drying parameters (e.g. solvent type, washing solvent type) of aerogels: surface area, pore size and pore volume all decrease with the increasing surface tension of the liquid to be removed from base-catalysed aerogels. On the other hand, micropore surface area and pore volume increase considerably in the case of acid catalysed gelation steps. Smith explains this phenomenon by pointing out that the higher the surface tension at the liquid-vapour interface, the higher the capillary pressure within the pore. When the pressure exceeds a certain threshold value, the gel network loses its integrity. Acid catalysed gels are less highly cross-linked then base catalysed ones, therefore, the same surface tension values correspond to the breaking of different pores in their case.

The last step in a typical sol-gel process is a high temperature treatment called densification or calcination. Maximum temperature, heating rate, atmosphere (inert or oxidising) etc. are the most important factors here. In the first stage of the heating process (up to 3-400 ºC) water and volatile organics (e.g. template molecules) are removed from the gel. This is generally accompanied by an increase in the specific surface area. Surface area diminishes in the second stage (up to 800-1000 ºC) because of capillary contraction, condensation and sintering. This is caused by the gel-to-glass transition, driven by the higher free energy of gels. In the final stage, once the gel-to-glass transition is complete, the structure and properties of the material are indistinguishable from those of a conventional melt-derived glass [26].

### 2.1.4 Applications

The simplest heterogeneous catalytic applications of sol-gel derived materials are those where the sol-gel sample is a simple replacement for a conventional catalyst: an amorphous sol-gel silica support instead of normal silica, silica-alumina composites instead of zeolites and so on. Albeit such examples are nowadays generally too common to claim any serious scientific attention, they can still be interesting materials, provided that either their pore system or their morphological features are special enough.

Sol-gel derived mixed oxides, on the other hand, make full use of the possibilities of the method. Vanadia-silica [27], alumina-silica [28], titania-silica [29], $Fe_2O_3$-$SiO_2$ [30], $ZrO_2$-$SiO_2$ [31] as well as BaO-$Al_2O_3$ and $La_2O_3$-$Al_2O_3$ [32] and many more composites have already been prepared successfully. Even though the goals of these investigations are quite different, their common feature is that they utilise the great control over homogeneity, elemental composition and sample morphology offered by the sol-gel technique. Samples are usually compared to those synthesised by conventional methods like co-precipitation or kneading, and more often then not, sol-gel materials are found to be superior in certain respects.

The same advantages and especially the achievable very small and uniform metal cluster size [33] make the sol-gel route a favourable alternative to conventional two-step impregnation methods for the preparation of metal — metal-oxide composites. Mixing can be performed at the atomic level; therefore, the resulting materials are of considerable interest to the currently flourishing nano-industry as well. Some catalytic applications reported are the selective side chain oxidation [34] of alkyl aromatic compounds over sol-gel derived Co-$SiO_2$, the synthesis of N,N-dimethylformamide over Group VIII transition metal containing silicas

[35] and detailed studies on the theory [36] and practice of selective benzene [37] and toluene [38] hydrogenation over Ru-$SiO_2$.

Truly exciting new materials can be prepared by the non-metallic functionalisation of sol-gel derived oxide matrices. Heteropoly acids, amino acids and carbohydrates can be anchored onto the walls of the pores, offering nearly endless possibilities for the heterogenisation of traditionally homogeneous reactions and performing such delicate tasks as molecular recognition [39] and chiral separation [40].

### *2.2 Morphology in heterogeneous catalysis*

Sample morphology in heterogeneous catalysis is considered to be important on at least three different levels: (i) macroscopic features like the maximum size of a monolith or the thickness and crack-freeness of a coating, (ii) "conventional" morphological issues concerning the shape of the primary particles of the material, and (iii) the layout of the pore system inside these particles.

By using the sol-gel method it is possible to gain control over all three levels at the same time, in one single synthesis. At well-defined points in the sol-to-gel transition, the viscosity of the material becomes ideal for spin coating [41] or dip coating [42], and thus, large crack-free membranes [43] can be prepared. Thanks to the versatility of the elemental composition (see previous Section), these membranes can be applied for separation [44] as well as for catalytic purposes [45].

Sol-gel derived primary particles can be prepared in an impressive number of shapes and curvatures [46], especially out of silica and by using supramolecular templating [47]. However, supramolecular assemblies have also been applied successfully for the synthesis of $TiO_2$ hollow fibers [48] and films [49] as well as mesolamellar aluminophosphates [50], for example. Well choosen templating may also lead to completely new pore systems, like sol-gel derived silica nanotubes [51] and silica foams [52, 53].

Fractal analysis has become a very popular tool in solid surface characterisation in the last two decades [54-57]. Fractal materials have scale invariant morphological features by definition, and can be classified [58] as mass fractals, pore fractals and surface fractals. From the point of view of heterogeneous catalysis, the latter two are of considerable interest, since transport efficiency [59] and catalytic activity [57, 60] may both be related to pore and surface self-similarity. Because of their paramount importance in separation, adsorption and catalysis, the fractality of silica species has been quite extensively studied [61-65] already. While it is

generally agreed [59] that pore fractals are rarely found among common porous materials, the existence of surface fractality in silica specimens is still heavily debated. Even by narrowing the scope of investigation down to sol-gel derived silicas we can find a wide range of opinions ranging from the denial ("*…it is more realistic to assume that a given porous system does not show a fractal structure*.", by Gottsleben and Hesse [66]) to the acceptance (numerous authors have calculated fractal dimensions for such species, e.g. Sermon *et al.* [64]) of the surface fractality of these materials.

## *2.3 Reactions of interest*

This thesis being focused on catalyst synthesis and characterisation, the Reader is referred to some excellent literature [67] about heterogeneous catalysis or acidity test reactions in general. However, I shall briefly mention the key points found in the literature about the two performed reactions awaiting more detailed examination in the future.

### 2.3.1 Carbon nanotube synthesis

Investigations on the carbon deposits formed over catalyst surfaces can be traced back to the early years of the 20$^{th}$ century. For a long time, these studies were focused on minimising the coke amount. In fact, it was not until the discovery of carbon filaments [68] that researchers became interested in the variety of carbon morphology to be found in such deposits. It was the rapid industrial career of carbon strengthened plastic composites that initiated the conscious in-depth investigations that eventually led to the discovery of multiwalled [69] and singlewalled [70] carbon nanotubes. Since then, a high level of research activity has been concentrated on these materials. Electric arc discharge [71], laser ablation [72] and catalytic vapour deposition [73] are the most often utilised carbon nanotube synthesis methods, of which the catalytic route appears to be the most promising for large scale industrial applications. Using different metals as catalysts supported on zeolites or silica, Ivanov *et al*. [74], Li *et al.* [75] and Mukhopadhyay *et al.* [76] reported the production of multiwalled nanotubes with 3-8 nm inner, 5-25 nm outer diameter and up to 60-80 μm length with remarkable efficiency at low temperatures. Currently, catalytic research efforts are concentrated on (i) increasing the nanotube yield, and (ii) improving product quality and homogeneity.

### 2.3.2 Diels-Alder type reactions

Diels-Alder type reactions are 4,2 type cycloadditions [77]. Their main advantage is that they make it possible to create more than one asymmetric centre [78] in one reaction step, and thus, they are widely used as a key step in the synthesis of complex carbon frameworks and natural products. The two reacting partners are a diene and a dienophile, the catalyst (required in most cases) is a Lewis acid, traditionally operating in homogeneous phase [79]. The catalyst is often a chiral molecule [80] itself.

Following the general trend of replacing homogeneous acidic catalysts by their heterogeneous counterparts, quite a number of studies are currently focused on Diels-Alder reactions catalysed by solid organic networks [81], clays [82], zeolites [83], ALPOs [84] and immobilised heteropoly acids [85]. The common features of these experiments are that (i) approximately the same conversion levels can be achieved as in conventional homogeneous reactions, (ii) the catalyst can be simply filtered off and reused after the reaction, and (iii) some regioselectivity can be observed in most cases. Contemporary research efforts are concentrated on improving stereoselectivity, either by incorporating chiral modifiers beside the catalytically active centres or by developing new materials where the pore system itself forces steric restraints on the reaction partners.

# 3. EXPERIMENTAL

In this Chapter I shall present all the synthesis recipes, experimental and computational details that were utilised to obtain the results of my research.

## *3.1 Synthesis*

Because of the wide range of materials studied herein, it is necessary to define a unified labelling system. All samples mentioned in this thesis are identified by a code printed in italics, built up as shown in Scheme 3. Sample codes are defined when mentioned for the first time, and are summarised in Table 16. in the Appendix.

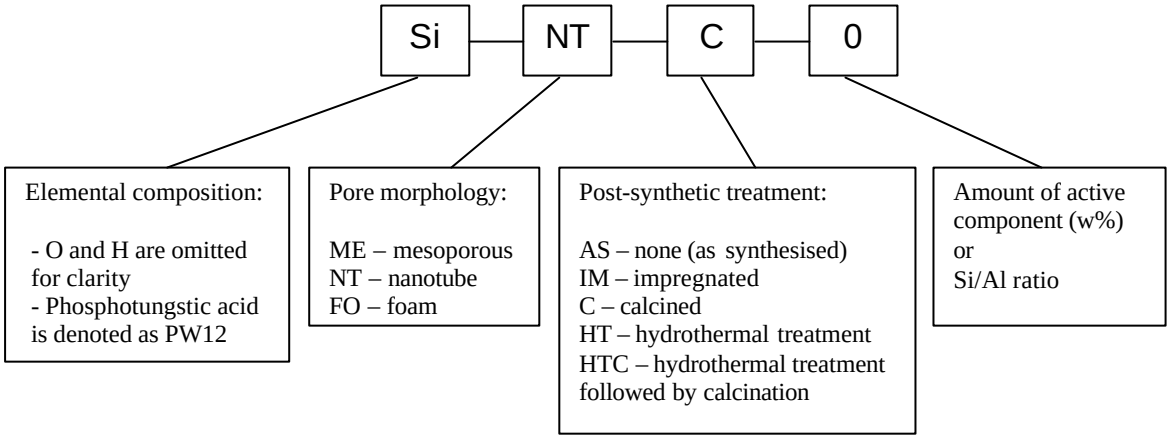


Scheme 3. Definition of the sample naming convention used throughout this thesis.

Even though the sol-gel technique can indeed be practised using a large variety of different source compounds, for the sake of consistency and simplicity only studies relying on one single alkoxide of each network-forming metal shall be described in this thesis. The chosen molecules are tetraethyl-orthosilicate (TEOS) as silicon, aluminum-tri-isopropoxide (AiPR3) as aluminum and tetraisopropyl-orthotitanate (TIPOT) as titanium source.

### 3.1.1 Mesoporous materials

#### *3.1.1.1 Materials containing transition metals*

Samples based on a purely siliceous matrix were prepared as follows. Nickel, cobalt and iron nitrates were dissolved in 7 ml of 2-propanol in amounts necessary to obtain a 5 w% total metal loading in the final metal-silica product, and stirred at 333 K for 60 min. Then, 10 ml TEOS was added to the solution and stirring was continued for an additional 60 min followed by the initiation of hydrolysis by the introduction of the following solution: 8 ml 2-

propanol + 25 ml distilled water + catalytic amount of acetic acid. The system was stirred for another 3 h at 333 K. A clear, transparent gel was obtained after complete gelation at ambient conditions in 12 h. The gel was ground into a fine powder, dried at 373 K under reduced pressure and calcined in a flow of $O_2$ at 770 K. According to the naming convention, these samples shall be referred to as *Co,Si-ME-C-5*, *Co,Ni,Si-ME-C-2.5* and so on.

Samples containing $TiO_2$ were prepared essentially the same way, but by adding a pre-mixed TEOS+TIPOT solution to the alcoholous metal salt solution instead of TEOS alone. Because of the moisture sensitivity of TIPOT, the water content of the hydrolysing solution was reduced to 4 ml to avoid phase separation caused by premature hydrolysis. In all $SiO_2/TiO_2$ composite samples the molar ratio of Si:Ti is 1:1, therefore, this ratio is not given explicitly in the sample code (e.g. *Co,Ti,Si-ME-C-5*).

*3.1.1.2 Materials containing 12-phosphotungstic acid*

The synthesis method of sol-gel derived 12-phosphotungstic acid ($H_3PW_{12}O_{40}$, denoted PW12 from now on) + silica composites was the following: 13.86 g TEOS was dissolved in a mixture of 8.26 g ethylene glycol and 8 g ethanol while stirring at 353 K in an oil bath. To this solution PW12 was added in a calculated amount to reach 5, 20, 50 or 80 w% heteropoly acid loading in the final (calcined) composite. After stirring for 1 hour, a mixture of 24 g ethanol, 6 g water and a catalytic amount of acetic acid was added to the system. The stirring rate and temperature were maintained long enough (typically 3 hours) to reach a clear, transparent, solid gel state. The resulting gel was aged at ambient conditions for 24 hours and dried under reduced pressure at 413 K for 3 hours. The colour of the samples changed from white to deep purple during the drying. Finally, the samples were calcined in air at 873 K for 6 hours, which caused their colour to change back to greenish white. The resulting xerogels were labelled *PW12,Si-ME-AS-5* … *PW12,Si-ME-AS-80* and *PW12,Si-ME-C-5* … *PW12,Si-ME-C-80*.

Another set of samples was prepared by conventional wet impregnation: PW12 was dissolved in 150 ml water in amounts calculated to produce 5, 20, 50 and 80 w% PW12 loading on the final composite, and these solutions were used to impregnate 5-5 g *Si-ME-C-0* by evaporationg the water at 313 K under reduced pressure. Thus samples *PW12,Si-ME-IM-5* … *PW12,Si-ME-IM-80* were obtained.

## 3.1.2 Macroporous materials

### *3.1.2.1 Silica nanotubes*

Silica nanotubes were prepared at ambient conditions by the method described by Nakamura et al. [51]. In spite of the considerable research effort invested, we were not able to significantly optimise the recipe any further. Results of these experiments shall be summarised in Section 4.2.1. However, we have found that it is possible to scale up the original process while maintaining a constant nanotube yield. The reaction was carried out as follows: 10.0 g DL-tartaric acid and 30.0 g water were dissolved in 2000 ml absolute ethanol. To this solution 365 g TEOS was added and the mixture was stirred for 5 minutes, while stirring with a magnetic stirrer. After that, the system was allowed to stand for 30 minutes and then 1000 ml of 25% $NH_3$ solution was added, while stirring lightly by a glass rod. In about 15 seconds an opal white gel was formed, which was permitted to stand for 20 minutes and then was washed with water to remove excess $NH_3$, dried at 378 K overnight and finally calcined at 773 K for 12 hours in a flow of $O_2$. Thus a fine white powder was obtained, which was labelled *Si-NT-C-0*.

The catalytically inert nanotubes were transformed into active heterogeneous catalysts by building phosphotungstic acid into them by the means of wet impregnation. Samples containing 5 w% and 20 w% PW12 were prepared by mixing 3 g *Si-NT-C-0* with a calculated amount of PW12 dissolved in 500 mL water. The water was gradually evaporated under continuous stirring at 363 K, then the samples were dried in air at 423 K overnight and labelled *PW12,Si-NT-C-5* and *PW12,Si-NT-C-20*, respectively.

### *3.1.2.2 Silica foams*

Macrocellular mesoporous silicate foams were prepared by a modified sol-gel route based on the technique suggested by Bagshaw [52]. 4.58 g Triton X-114 (a non-ionic surfactant from Fluka) was dissolved in 30 g $H_2O$ adjusted to pH=1 by a few drops of $H_2SO_4$. This solution was stirred at ambient conditions at 500 rpm by a magnetic stirrer for 1 hour and then 13.86 g TEOS was added to the foam. Stirring was maintained until a thick white gel was formed (4-6 hours). The gel was transferred into a Petri dish and allowed to age overnight. One half of the resulting foam monolith was hydrothermally treated at 413 K for 24 hours, while the other half was dried at 313 K for 24 hours. Finally, both samples were calcined at 673 K in a flow of $O_2$ for 8 hours, and labelled *Si-FO-C-0* and *Si-FO-HTC-0*, respectively.

Solid acid foams containing 5 w% and 20 w% PW12 were prepared by the drop-wise addition of the required amount of PW12 solution to the forming TEOS foam. Silica/alumina composite acid foams were obtained by carefully adding the alcoholous solution of AiPR3 to the forming TEOS foam in amounts necessary to reach Si/Al ratios of 20 and 5, respectively. All these acidic foams were aged at ambient conditions for 24 hours, then either hydrothermally treated at 413 K for 24 hours, dried at 313 K for 1 day and finally calcined at 473 K for 8 hours in a flow of $O_2$. Sample codes were given following the rules defined above (e.g. *PW12,Si-FO-C-5* or *Al,Si-FO-HTC-20*, 8 samples altogether).

## *3.2 Characterisation*

### 3.2.1 Elemental analysis

Most samples were assumed to have the elemental composition defined by the synthesis recipe. Though this might sound a touch inaccurate at first, it is a rather correct guess. Only alcohols and water are removed from the gel during the sol-gel synthesis, therefore, there is no reason to believe that the ratio of the key components (e.g. acid function) suffers any changes over the course of the process.

However, in the case of the most complex bimetallic mesoporous samples (*Me1,Me2,Si,Ti-ME* group) atomic absorption spectroscopy was performed in order to determine the exact metal loading. Around 200 mg sample was dissolved in a mixture of 5 ml 40% HF, 5 ml cc. HCl and 10 ml 12.5% $HNO_3$, which was heated from room temperature to 453 K in 10 minutes in a microwave oven, kept at 453 K for 20 minutes and allowed to cool afterwards. Metal loadings were determined from these solutions by a Zeiss AAS spectrometer.

### 3.2.2 Sample features on the molecular scale

#### *3.2.2.1 UV-VIS spectroscopy*

Diffuse reflectance UV-VIS spectra of samples ground to fine dust were recorded on a Perkin-Elmer Lambda 15 instrument at ambient conditions against MgO reference in reflectance mode. Spectra presented in this thesis were derived from the measured ones using the Kubelka-Munka equation [86] as defined in Eq. 1.:

$$F(R_\infty) = \frac{(1-R_\infty)^2}{2R_\infty} \qquad \text{Eq. 1.}$$

where $R_\infty$ is the reflectance of the infinitely thick sample layer.

*3.2.2.2 FT-IR spectroscopy*

For structural infrared investigations 1 mg sample powder was pressed into a 200 mg KBr pellet, the spectrum of which was recorded at a resolution of 2 $cm^{-1}$ making 32 scans on our Mattson Genesis FT-IR 1 instrument. All spectral subtractions were performed on normalised spectra in absorbance mode.

*3.2.2.3 $^{29}$Si MAS NMR spectroscopy*

$^{29}$Si MAS NMR spectra were recorded on a 400 MHz BRUKER instrument in $^{1}$H high power decoupling mode against TMS reference. Measurements were performed at FUNDP, Namur, Belgium by Patrick Lentz.

*3.2.2.4 X-Ray Diffractometry*

XRD patterns were recorded between 2T=3-43º on a DRON-3 instrument operating with Cu $Ka_1$ irradiation (wavelength: XXXX nm).

*3.2.2.5 Thermogravimetry*

TD and DTA profiles of the samples were recorded in air between room temperature and 1200 K on a MOM Derivatograph-Q instrument. Approximately 100 mg sample (measured accurately into a ceramic crucible sample holder) was consumed in each experiment. The heating rate was 10 K/min and linear.

### 3.2.3 Acidity

*3.2.3.1 Pyridine adsorption*

The Brönsted and Lewis acid centres of the samples were characterised on the basis of the IR spectrum of pyridine adsorbed on the activated material. The samples were pressed into 10 $mg/cm^2$ self-supporting wafers which were outgassed at 723 K in vacuum and then exposed to 10 Torr pyridine at 473 K for 30 min. Excess pyridine was removed in vacuum at 423 K and then the spectrum of the adsorbed pyridine was recorded on the Mattson Genesis FT-IR 1 instrument (32 scans, 2 $cm^{-1}$ resolution). The IR cell used for the experiments is described in detail in Section 3.3.3.

*3.2.3.2 $NH_3$ desorption*

Total acid content was measured by recording the $NH_3$ TPD profile of the samples. In these experiments 10 mg sample was outgassed at 723 K in vacuum and subjected to an 5%

$NH_3$:95% He gas mixture until no more weight gain was observable at room temperature. TPD profiles were recorded by directly measuring the weight loss of the sample on a Shimadzu microbalance while heating at 10 K/min in a flow of He. Each experiment was accompanied by a blank measurement to compensate for thermal weight losses unrelated to $NH_3$ release.

### 3.2.4 Electron microscopy

TEM pictures were taken with the JEOL instrument of the NIMC, Tsukuba, Japan. SEM images were taken either on the Hitachi instrument of NIMC, Tsukuba, Japan or on the XXXX microscope of FUNDP, Namur, Belgium.

### 3.2.5 Adsorption behaviour

The majority of the nitrogen adsorption-desorption isotherms was measured in a conventional volumetric apparatus. In a typical experiment, 150 mg , 150 mg sample from a d=0.25-0.40 mm sieve fraction was outgassed at 723 K in vacuum for 1 hour. After activation the dead volume of the system was calibrated using He gas, and finally, the adsorption-desorption isotherm of $N_2$ was measured at 77 K.

A few isotherms were obtained on the automatic XXX system of the Institute for Technical Chemistry of TU Dresden, Germany. In these experiments 1 g sample outgassed at 523 K for 2 hours was used.

### 3.2.6 Effects of mechanical pressure

The effects of mechanical pressure on the surface fractal dimension were studied for a representative sample of all three pore systems (mesoporous, nanotube, foam) by applying 0, 3, 9 ton/cm$^2$ pressure to 200 mg material for 2 minutes, after which the $N_2$ adsorption isotherm was measured and the fractal dimension calculated.

## *3.3 Catalytic experiments*

### 3.3.1 Synthesis of carbon nanotubes

Acetylene was used as a source of carbon for the production of carbon nanotubes. The decomposition of acetylene was carried out at atmospheric pressure in a fixed bed flow reactor. In a typical experiment, 5 g catalyst was spread manually on a quartz plate in a thin layer (1-2 mm thick) and placed into a preheated tube furnace. After purging with $N_2$ (120

ml/min) for 15 min the acetylene stream was opened for 1 hour for the CCVD reaction to take place. Three different temperatures (770, 870 and 970 K) were tested and two different acetylene flow rates (15 and 25 ml/min). All these experiments were performed at FUNDP, Namur, Belgium by Dr. Zoltán Kónya.

### 3.3.2 Isomerisation of 1-butene

Catalytic activity of the solid acid samples was tested by the isomerisation reaction of 1-butene to 2-butenes in a fixed bed recirculatory reactor. In a typical experiment, 100 mg sample of a d=0.25-0.40 mm sieve fraction was placed in the reactor and outgassed for 1 hour at 673 K in a vacuum of $3*10^{-2}$ Torr. 500 Torr of 1-butene was introduced into the reactor, and the reaction was started. The reaction was monitored by sampling the gas mixture at regular intervals. Analysis of these samples was performed *via* an on-line Hewlett Packard 5710A gas chromatograph equipped with a 4.5 m × 6 mm 30% dimethylsulpholane on Chromosorb-W column and FID. The system is visualised in Scheme 4.

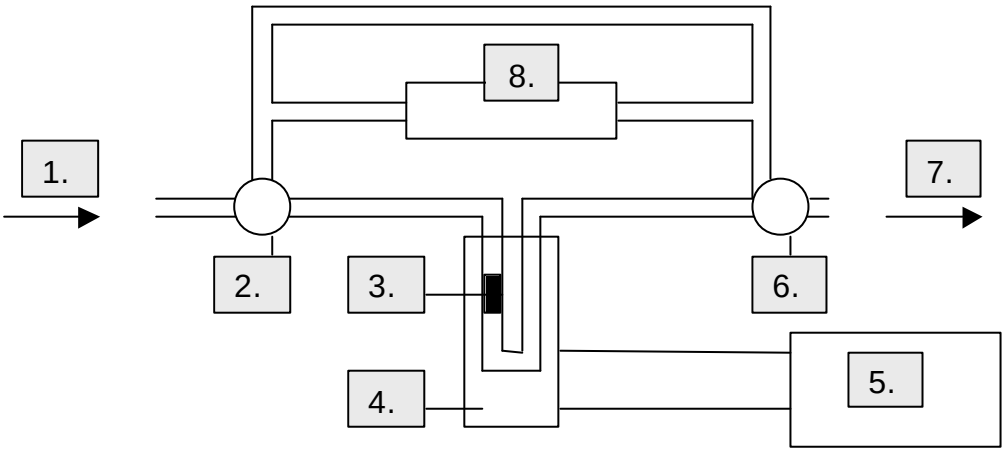


Scheme 4. Test system set-up for 1-butene conversion reactions.

1: towards vacuum line, 2: gas inlet valve, 3: catalyst bed, 4: heating, 5: temperature controller, 6: sampling valve, 7: towards GC line, 8: magnetic pump

### 3.3.3 Diels-Alder reactions

Because of certain limitations of our chromatographic equipment, we have decided to monitor the Diels-Alder type test reactions *via* IR spectroscopy. This technique is not often used for such a purpose, therefore, these experiments not only provide catalytic data but have their methodological merits as well.

The measurements were performed by placing a self-supported catalyst wafer (ca. 10 $mg/cm^2$) into a heatable cell allowing *in situ* IR measurements. The catalyst was outgassed for 1 hour at 673 K and then the 2:1 mixture of 1,3-cyclohexadiene and 2-propenal was

introduced into the cell at room temperature. Both the gas phase and the catalyst surface were monitored at regular intervals by recording their IR spectrum (32 scans, 2 $cm^{-1}$ resolution) on a Mattson Genesis FT-IR 1 instrument. The IR cell is visualised in Scheme 5.

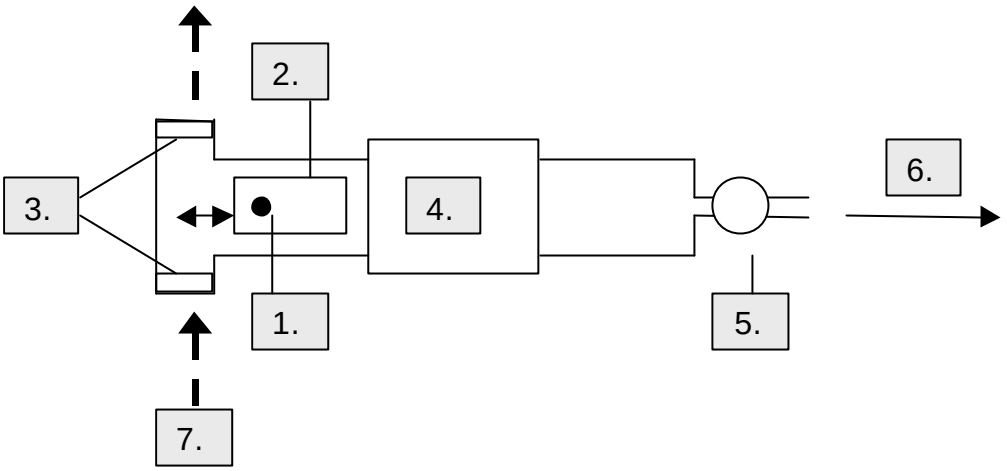


Scheme 5. Schematics of the heatable IR cell used for catalytic measurements.

1: self-supporting sample wafer, 2: movable sample holder, 3: KBr windows, 4: heating and temperature control, 5: gas inlet valve, 6: towards vacuum line, 7: IR radiation from the spectrometer.

### *3.4 Computational methods*

The following section shall be devoted to the description of the major mathematical tools I have applied.

#### 3.4.1 Pore structure characterisation

Specific surface areas were determined from the $N_2$ adsorption isotherms using the Brunauer-Emmett-Teller (BET) equation [87]. The validity of the BET model was not verified in each case, but care was always taken so that only the truly linear part (typically $0.05 < p / p_0 < 0.35$) of the BET plot (plot of $p / V(p-p_0)$ vs. $p / p_0$) is taken into account when performing the least square linear fitting required by Eq. 2.:

$$\frac{p}{V(p_0 - p)} = \frac{1}{V_m c} + \frac{c-1}{V_m c} \cdot \frac{p}{p_0} \qquad \text{Eq. 2.}$$

where $V$ is the volume of the gas adsorbed, $p$ is the pressure of the gas, $p_0$ is the saturated vapour pressure of the liquid at the operating temperature, $V_m$ is the volume equivalent to an adsorbed monolayer and $c$ is the BET constant given by Eq. 3.:

$$c = \exp\left(\frac{H_1 - H_L}{RT}\right) \qquad \text{Eq. 3.}$$

In this expression, $H_1$ is the fixed heat of adsorption of the first layer of adsorbate and $H_L$ is the latent heat of evaporation, characterising the cohesion strength between all but the surface and the first adsorbate layer.

In addition to the specific surface area, the pore shape, size and the homogeneity of the size distribution are all equally important characteristics of a given porous system. These quantities have been determined from the $N_2$ adsorption-desorption isotherms using the fact that gas condenses to liquid in narrow pores at pressures less than the saturated vapour pressure of the adsorbate. The relation between the $r$ radius of a cylindrical pore and the equilibrium pressure $p$ of the adsorbate above the meniscus is given by the Kelvin equation (Eq. 4.):

$$\ln \frac{p}{p_0} = -\frac{2gV}{rRT}\cos f \qquad \text{Eq. 4.}$$

where $p_0$ is the saturated vapour pressure of $N_2$ at the temperature $T$ of the system, $g$ and $V$ are the surface tension and the molar volume of $N_2$ in liquid form, $R$ is the universal gas constant and $f$ is the angle of contact between the liquid and the wall of the pore. Even though in principle it is possible to evaluate the pore size distribution from the adsorption branch of the isotherms, all calculations reported in this thesis are based on the analysis of the desorption branch in order to take hysteresis effects into account.

Unfortunately, the simple Eq. 4. does not make allowance for the reduction of the width of the pore entrances because of the multiple layers of adsorbate adsorbed on the walls of the capillary. Moreover, the thickness of this adsorbed layer is not constant: it diminishes during desorption. Parallel to this process, the area of the walls covered by the adsorbed layer is increasing due to the fact that more and more pores lose their capillary-condensed liquid. Wheeler [88] summarised this situation in mathematical terms by writing:

$$v_p - v_a = \int_{r_p}^{\infty} p\left(r_p - t\right)^2 L(r)dr \qquad \text{Eq. 5.}$$

where $v_p$ is the total pore volume, $v_a$ is the volume adsorbed (computed as liquid volume) at the relative pressure at which all pores having radii less than $v_p$ are full and $t$ is the thickness of the layer adsorbed on the walls. As the $t$ thickness can be estimated using the Halsey equation:

$$t = s\left[\frac{5}{2.303\log_{10}\frac{p}{p_0}}\right]^{\frac{1}{3}} \qquad \text{Eq. 6.}$$

where the value $s$ = 4.3 A is assigned to $s$, the only unknown in Eq. 5. is the *L(r)* pore size distribution. Since *L(r)* is involved in the integration, the solution is somewhat complicated, and therefore, it has been addressed by a large number of researchers. Results reported herein were obtained by the procedure known as the Barret-Joyner-Halenda (BJH) method [89].

Micropore volumes have been calculated from the low pressure parts of $N_2$ adsorption isotherms by the Dubinin-Radushkevich equation [90]:

$$\ln W = \ln W_0 - \left(\frac{1}{E_0}\right)^2\left(\frac{m}{b}\right)^2 \qquad \text{Eq. 7.}$$

where $W$ is the volume of the adsorbate assumed to be in liquid state, $W_0$ is the micropore volume, $b$ is an activity coefficient related to the molar specific volume, $E_0$ is the characteristic energy related to the mean radius of the micropores, and $m$ is the adsorption potential defined as:

$$m = RT\ln\left(\frac{p_0}{p}\right) \qquad \text{Eq. 8.}$$

One can not make guesses of such precision about the shape of the capillaries. While it is generally agreed that pore shapes can be deducted from the type of the hysteresis loop of the adsorption-desorption isotherms, there is no fail-safe way to obtain this information. Isotherms reported in this thesis can be classified [91] as type A and E hysteresis loops, and therefore, we assume that the typical pore shape of our sol-gel materials (except silica nanotubes, see Section 4.2.1) is either cylindrical or ink-bottle.

### 3.4.2 Calculation of the fractal dimension

The most widespread methods for the calculation of surface fractal dimension $D$ are based on adsorption measurements. One either measures the variation in the specific surface area when determined by use of a series of adsorbents (e.g.: n-alkanes) or determines the surface roughness from the data contained in one adsorption isotherm. In this thesis I present results obtained by the latter approach. The $N_2$ adsorption-desorption isotherms have been analysed both by the Frenkel-Halsey-Hill (FHH) equation [92] and by the Wang method.

The FHH equation can be expressed as

$$\ln N = const - (3 - D)\ln m \qquad \text{Eq. 9.}$$

where N is the amount adsorbed at the relative pressure $p/p_o$ (the range $0.35 < p/p_o < 0.75$ has been used for the detemination of $D$) and absolute temperature $T$, and $m$ is the adsorption potential as defined in Eq. 8..

The calculation suggested by Wang and Li [63] is a development of the so-called thermodynamic method first described by Neimark [93]. The $D$ surface fractal dimension can be calculated from the data in the region of capillary condensation (the whole $p/p_o > 0.35$ region can be used for the calculation) of both the adsorption and the desorption branches of the isotherms by use of the following relationship:

$$\ln A(X) = const + D\ln B(X) \qquad \text{Eq. 10.}$$

where $X$ denotes the relative pressure $p/p_o$ and $A(X)$ and $B(X)$ are defined as:

$$A(X) = \frac{\int_{N(X)}^{N_{max}} \ln X dN(X)}{r_c^2(X)} \qquad \text{Eq. 11.}$$

$$B(X) = \frac{\left[N_{max} - N(X)\right]^{\frac{1}{3}}}{r_c(X)} \qquad \text{Eq. 12.}$$

In these equations $N_{max}$ denotes the amount adsorbed at $X$ tending to unity, and $r_c$ can be calculated from the Kelvin equation (Eq. 4.).

### 3.4.3 Quantum chemical calculations

The forces of molecular modelling were utilised for the validation of certain conjectures concerning the optimal geometry and heat of formation of molecules. The semi-empirical level of theory provides adequate precision for such computation, therefore, all calculations were performed using the AM1 method built into the Spartan 4.1.1 package running on an SGI Indy R5000.

### 3.4.4 Statistical background

Errors in the data were only calculated for measurements where the exact figures were considered to be important. In these cases, a confidence interval is given from 3 independent measurements, at 95% significance level, assuming normal error distribution.

# 4. RESULTS AND DISCUSSION

As mentioned already in the Introduction, the main goal of this PhD work was to lay down the foundations of possible future exploitations of a technique previously unknown to our group. Therefore, this Results and Discussion section should not be read expecting 50 pages of solid science with one rock-hard conclusion in the last paragraph. Rather, it should be read as a research menu: a selection of smaller independent projects, each solving a problem of its own, and each having the potential to serve as starting point for a detailed, long-term research plan.

## *4.1 Mesoporous materials*

The mesoporous region (pore diameter ranging from 20-100 Å) is probably the scale where sol-gel derived materials might find their most beneficial applications as heterogeneous catalysts. Below that, synthetic zeolites seem to work very efficiently in nearly every field of operation; above that, pores become far too wide to be practical from the catalytic point of view. Mesoporous openings, however, are just about the right size for certain industrially important molecules and because of that, ample research effort is being spent on building every imaginable catalytic function into such porous systems.

### 4.1.1 Materials containing transition metals

Transition metals and their oxides very often serve as active species in heterogeneous catalysts. The reason for this is either their special affinity towards hydrogen (e.g. Ni, Pt, Pd) or the variety of possible stable oxidation states their valence shell offers. Some very early applications of the sol-gel method were about building transition metals into various oxide matrices. As the present research interests of our department are related to catalytic carbon nanotube synthesis, in the following Section I shall describe our studies [94] concerning the sol-gel incorporation of cobalt, nickel and iron into Si and Ti oxides. These elements have all been chosen because of their previously reported roles in carbon nanotube synthesis.

#### *4.1.1.1 Characterisation*

As we can see from Table 1., the specific surface area of each sample was high but not exceptional. The probability maximum of their pore radius distribution curve was diffuse and centred at around 18 Å and approximately 15-25 % of their total pore volume originated from micropores. These values correlate well with each other and findings described in the literature, and can be traced back to the presence of the pore structure directing agent

ethylene-glycol in the precursor sol. Accurate knowledge of metal loading was considered to be important for these samples. Data obtained by AAS measurements presented in Table 1. indicates that our synthesis procedure was successful: the transition metals were incorporated into the sol-gel samples in the required quantities. Deviations from the expected theoretical values were random and within experimental error.

| | BET surface area ($m^2/g$) | Co contents (w%) | Fe contents (w%) | Ni contents (w%) |
|---|---|---|---|---|
| *Co,Fe,Si,Ti-ME-C-2.5* | 233 | 2.34 | 2.32 | 0.0 |
| *Co,Fe,Ti-ME-C-2.5* | 289 | 2.42 | 2.23 | 0.0 |
| *Co,Fe,Si-ME-C-2.5* | 268 | 3.23 | 2.53 | 0.0 |
| *Fe,Ni,Si,Ti-ME-C-2.5* | 241 | 0.0 | 2.98 | 2.41 |
| *Fe,Ni,Ti-ME-C-2.5* | 276 | 0.0 | 2.71 | 2.64 |
| *Fe,Ni,Si-ME-C-2.5* | 290 | 0.0 | 2.50 | 2.36 |
| *Co,Ni,Si,Ti-ME-C-2.5* | 237 | 2.46 | 0.0 | 2.13 |
| *Co,Ni,Ti-ME-C-2.5* | 249 | 2.35 | 0.0 | 2.20 |
| *Co,Ni,Si-ME-C-2.5* | 295 | 2.74 | 0.0 | 2.31 |

Table 1. Certain characteristic features of the transition metal containing sol-gel samples

One of the major advantages of the sol-gel method is that it ensures a highly homogeneous distribution of transition metals in the matrix. This assumption has been experimentally confirmed in the case of randomly selected *$Me_1$,$Me_2$,Si-ME-C-* samples by recording the TEM image of the materials. On the representative picture presented in Figure 2. the dark spots are believed to be metal clusters, while the lighter areas correspond to the silica matrix. On the basis of this image we estimate the average metal cluster size to be around 18 nm.

Figure 3. presents the diffuse reflectance UV-VIS spectra of the samples investigated [94]. According to Prakesh *et al.* [95], bands belonging to the titania matrix could be: at 200 nm a charge transfer transition indicates framework co-ordinated Ti, bands at 250-300 nm are characteristic of octahedral Ti and the presence of bands around 300-350 nm indicates that segregated crystalline anatase $TiO_2$ is present. Part A exhibits the UV-VIS spectra of Co,Fe containing specimens before (left hand side) and after (right hand side) calcination. These samples are especially interesting because of the enhanced carbon nanotube producing activity of Co,Fe silica compared to other metal pairs and matrices (see Section 4.1.1.2 for details).

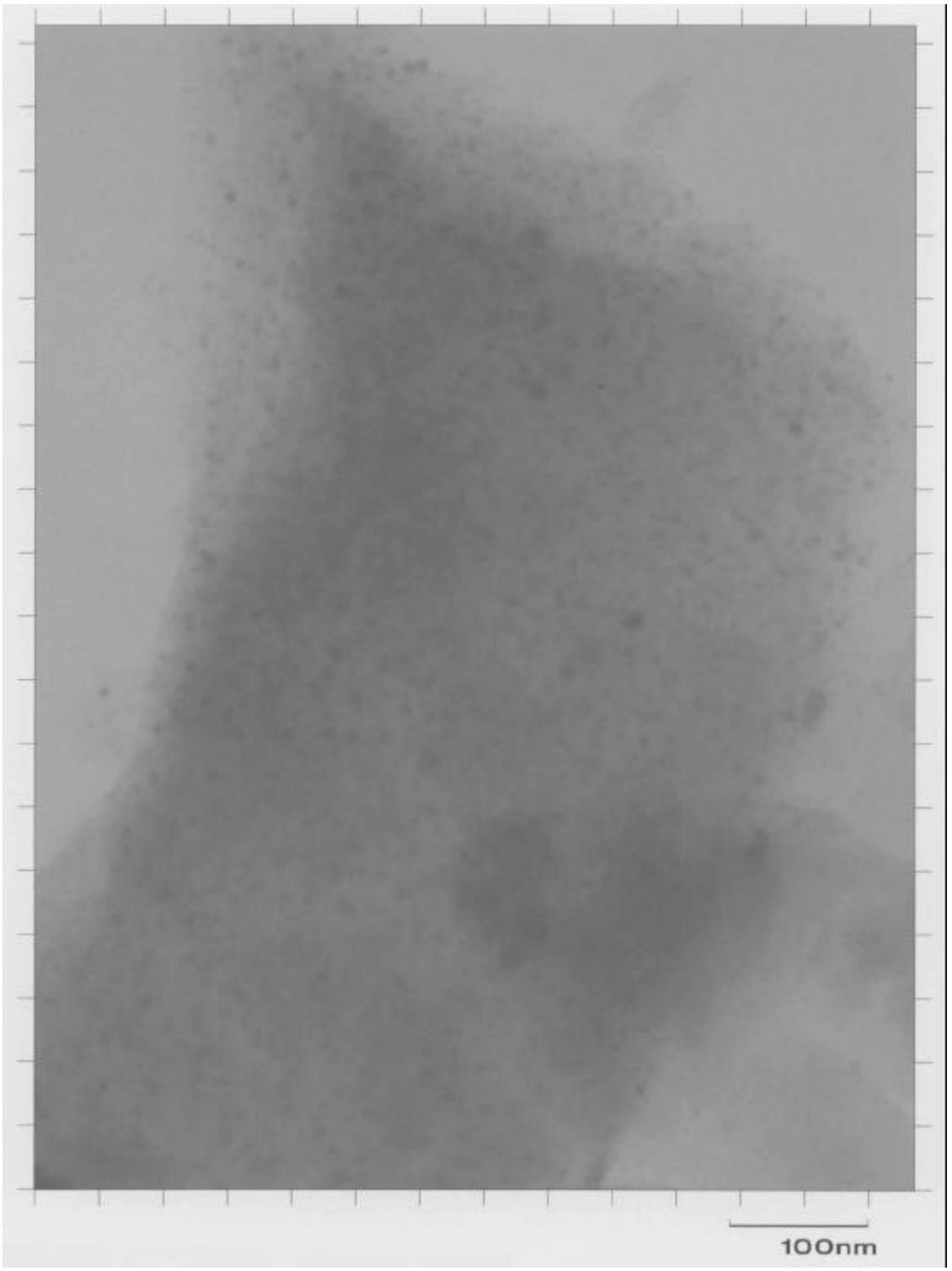


Figure 2. Representative TEM image of a transition metal containing sol-gel silica sample (*Co,Fe,Si-ME-C-2.5*)

In silica matrix (spectra “a” and “d”) four bands are clearly seen at 250, 350, 380 (as shoulder) and 550 nm for the as-synthesised sample, while in the heat-treated derivative the position of electronic transitions changed to 250, 340, 500 and 580 nm.

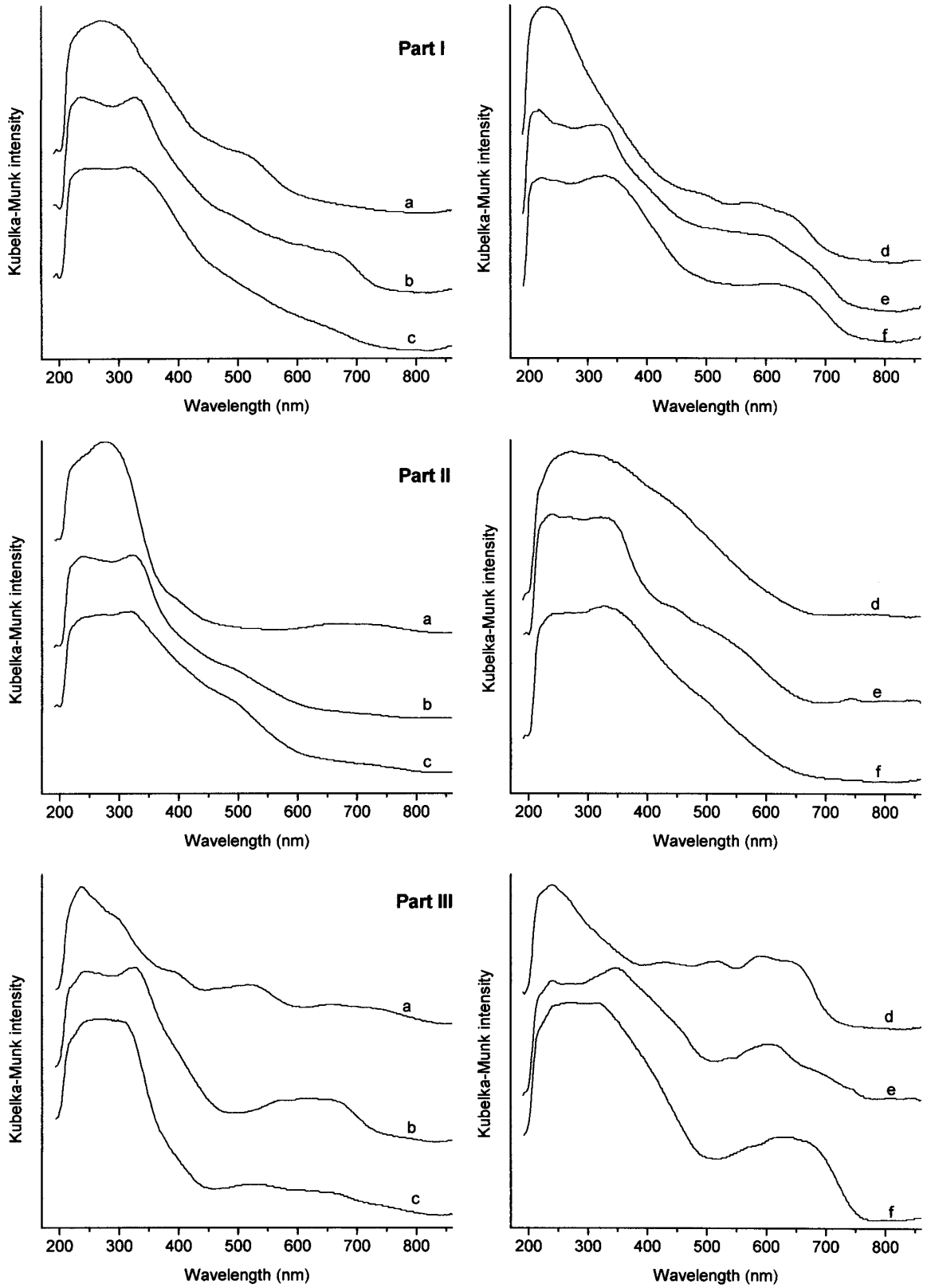


Figure 3. Diffuse reflectance UV-VIS spectra of samples studied. Part **I**: Co-Fe, Part **II**: Fe-Ni, Part **III**:. Co-Ni. On all graphs: a: $SiO_2$ matrix, b: $TiO_2$ matrix, c: $SiO_2$-$TiO_2$ matrix, d: calcined $SiO_2$, e: calcined $TiO_2$, f: calcined $SiO_2$-$TiO_2$.

Four bands appeared in titania at 250, 350, 480 and 680 nm, and their position has changed slightly upon heat treatment. The most obvious change was found for the band at 680 nm whose intensity has gradually increased. In the case of titania-silica matrix much greater changes occurred, the most characteristic of which was the increase in the intensity of the 655 nm band.

For Ni,Fe samples, spectra of which are presented in Part B of Figure 3., smoother changes were found. The low frequency bands (720, 670, 516 nm) are much less separated than those of the former samples. This could be due to the fact that here two easily oxidisable-reducible ions were introduced into the matrices. If these ions are oxidised, bands in the UV-VIS spectra are expected to suffer broadening because of the increase in the number of oxidation states — and thus possible electron transitions — in the samples. This phenomenon is readily observed when comparing the spectra of as-synthesised and heat treated samples, irrespective of the matrix used.

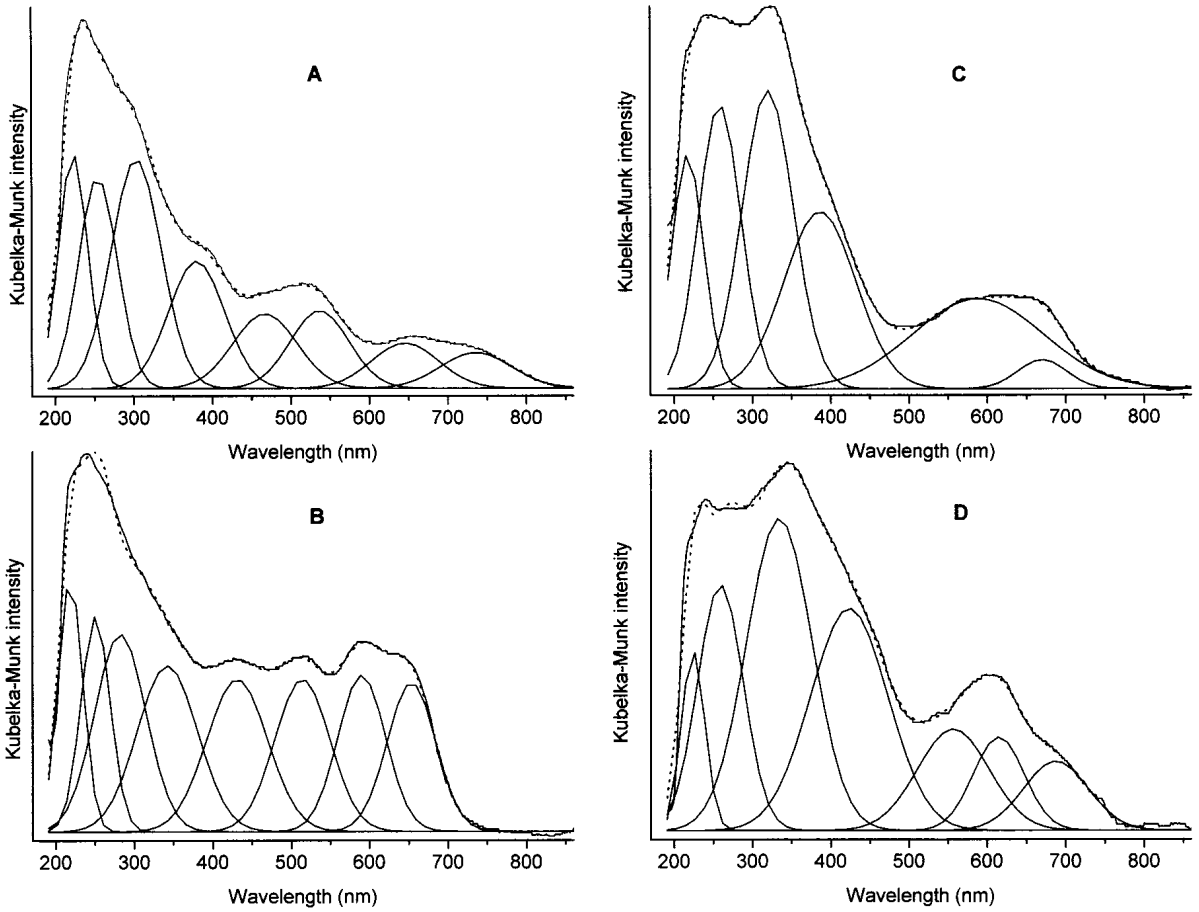


Figure 4. Some representative spectral decompositions of Co-Ni composites: **A**: as-synthesised, $SiO_2$ matrix; **B**: calcined, $SiO_2$ matrix; **C**: as-synthesised, $TiO_2$ matrix; **D**: calcined, $TiO_2$ matrix. On all four spectra, the dotted line denotes the sum of the Gaussians.

Spectra of Co,Ni containing materials are depicted in Part C of Figure 3. The substantial influence of the matrix is clearly seen on these spectra. Several bands appeared in each spectrum (740, 650, 550, 465, 385 nm), and the calcination resulted in major spectral changes. On Figure 4. a few representative multi-peak spectral decompositions are shown. Presenting such details of all 18 spectra would not provide significant extra information, and therefore, it shall be omitted. It is enough to note here that the same decomposition routine was applied for all spectra presented in Figure 3. Therefore, whenever a "band" is mentioned here, we always mean a spectral entity whose existence has been confirmed by such fitting of the data. Assignment of these bands, however, seems to be rather difficult.

| Ion | Environment | Band (nm) | Transition |
|---|---|---|---|
| $Fe^{2+}$ | octahedral | peaks around 500 | $^5T_{2g}\rightarrow{}^5E_g$ |
| $Fe^{3+}$ | octahedral | 813, 704 | $^6A_{1g}\rightarrow{}^4T_{1g}$ |
| | | 571, 500 | $^6A_{1g}\rightarrow{}^4T_{2g}$ |
| | | 434 | $^6A_{1g}\rightarrow{}^4A_{1g}$ |
| | | 377 | $^6A_{1g}\rightarrow{}^4T_{1g}$ |
| $Co^{2+}$ | octahedral | peaks around 500 | $^4T_{1g}\rightarrow{}^4T_{1g}(P)$ |
| | tetrahedral | 560 | $^4A_2\rightarrow{}^4T_1(P)$ |
| $Co^{3+}$ | octahedral | 714 | $^1A_{1g}\rightarrow{}^3T_{1g}$ |
| | | 467 | $^1A_{1g}\rightarrow{}^1T_{1g}$ |
| | | 338 | $^1A_{1g}\rightarrow{}^1T_{2g}$ |
| $Ni^{2+}$ | octahedral | 740 | $^3A_{2g}\rightarrow{}^3T_{1g}(F)$ |
| | | 395 | $^3A_{2g}\rightarrow{}^3T_{1g}(P)$ |

Table 2. Possible assignments of bands present in the UV-VIS spectra of the transition metals studied here. All assignments are taken from Ref. [96].

Even though there is plenty of literature data concerning the electronic transitions of the elements studied here, we must realise that results similar to those presented in Table 2. are of limited use for the interpretation of our spectra. This is probably due (i) to the fact that instead of a well-defined crystal, transition metals in our samples are partially incorporated into amorphous sol-gel materials, and (ii) to the co-presence of two similar ions in such an amorphous structure. In our earlier work [97] we have already suggested that some sort of co-operative effect modifying the acidity could exist in bimetallic sol-gel samples — it is quite possible that certain electronic transitions of the metals are also linked. This could result in the complex band structure of the UV-VIS spectra, and would — at least partially — explain the special activity enhancement observed on Co,Fe silica in carbon nanotube synthesis.

*4.1.1.2 Catalytic activity*

Transition metal containing mesoporous sol-gel composites may find numerous applications in heterogeneous catalysis. We have investigated some of the factors governing their Lewis acidity [97] and by exploiting this knowledge we have successfully utilised them as catalysts of Diels-Alder reactions [98]. Studies related to the redox and photocatalytic properties of $TiO_2$ containing sol-gel materials are currently under progress [99].

In this thesis I shall present only the most interesting new results: the ones about using the bimetallic silica species as catalysts in catalytic chemical vapour deposition (CCVD) carbon nanotube synthesis. These experiments were performed as described in Section 3.3.1.

The amount of carbon deposited on the catalyst was calculated from the difference in weight of the catalyst before ($m_0$) and after ($m_p$) treatment in the acetylene flow by using Eq. 13.:

$$deposit(\%) = 100\frac{m_p - m_0}{m_0} \qquad \text{Eq. 13.}$$

Sol-gel $m_0$ values were corrected by the high temperature weight loss characteristic for these materials. Data presented in Table 3. prove that each catalyst tested in the reaction of acetylene was active in carbon generation [100].

| | Temperature (K) | | |
|---|---|---|---|
| | 770 | 870 | 970 |
| 2.5% Co on silica* | 6.2 | 22.1 | 28.2 |
| 2.5% Co on alumina* | 7.1 | 18.8 | 26.9 |
| 2.5% Fe on alumina* | 12.8 | 32.4 | 52.7 |
| 2.5% Ni on alumina* | 22.9 | 89.3 | 120.7 |
| *Co,Si-ME-C-5.0* | n.a.** | 1.9 | 8.9 |
| *Fe,Si-ME-C-5.0* | n.a. | 1.0 | 8.2 |
| *Ni,Si-ME-C-5.0* | n.a. | 0.3 | 6.1 |
| *Co,Fe,Si-ME-C-2.5* | n.a. | 16.7 | 31.1 |
| *Co,Ni,Si-ME-C-2.5* | n.a. | 1.1 | 10.7 |
| *Fe,Ni,Si-ME-C-2.5* | n.a. | 0.5 | 11.2 |

* Non sol-gel catalysts presented for comparison purposes
** Catalyst not acting at that temperature

Table 3. Carbon deposits formed in the CCVD reaction after 1 hour

Analysing the data of Table 3., it should be noted at once that the high activity towards the formation of carbon species of the reference catalyst "2.5% Ni on alumina" is not equal to the formation of the desired carbon nanotubes.

Indeed, no nanotube formation was observable at all on that catalyst, only poorly graphitised amorphous carbon.

Our sol-gel catalysts performed moderately in this reaction. The amount of carbon deposit formed on the sample was commensurable with, yet definitely smaller than that on the non sol-gel materials. The *Co,Fe,Si-ME-C-2.5* sample generated a significantly larger amount of carbon than the other sol-gel phases. This finding is in good agreement with our recent results [101] concerning the peculiar properties of supported Co-Fe bimetallic catalysts.

HREM images of the carbon nanotubes generated on sol-gel catalysts show diverse features. While these materials are definitely capable of producing carbon nanotubes, the quality of the product seems to be more sensitive to the catalyst composition than in the case of ordinary supports. Thin and thick tubes with encapsulated particles and frequent defects were observed both on Co and on Ni incorporated into sol-gel silica (Figure 5.)

A rather interesting feature of these MWNTs is that they have a double wall structure. The inner set of walls is made of 6-20 graphite layers, and this is covered by 5-10 loosely attached layers of partially graphitised carbon. On the other hand, the *Co,Fe,Si-ME-C-2.5* sample produced well graphitised, high quality tubes, once again indicating the importance of the binary metallic phase.

All in all, the temperature dependence of the catalytic activity of the sol-gel materials seems to match that of the conventional reference samples. They tend to produce significantly less carbon deposit than their non sol-gel counterparts, but this deposit is always rich in carbon nanotubes. The quality of these nanotubes is generally diverse. However, the *Co,Fe,Si-ME-C-2.5* is among the best catalysts we have tried in respect of structural defects, and should be seriously considered by anyone interested in producing high quality carbon nanotubes.

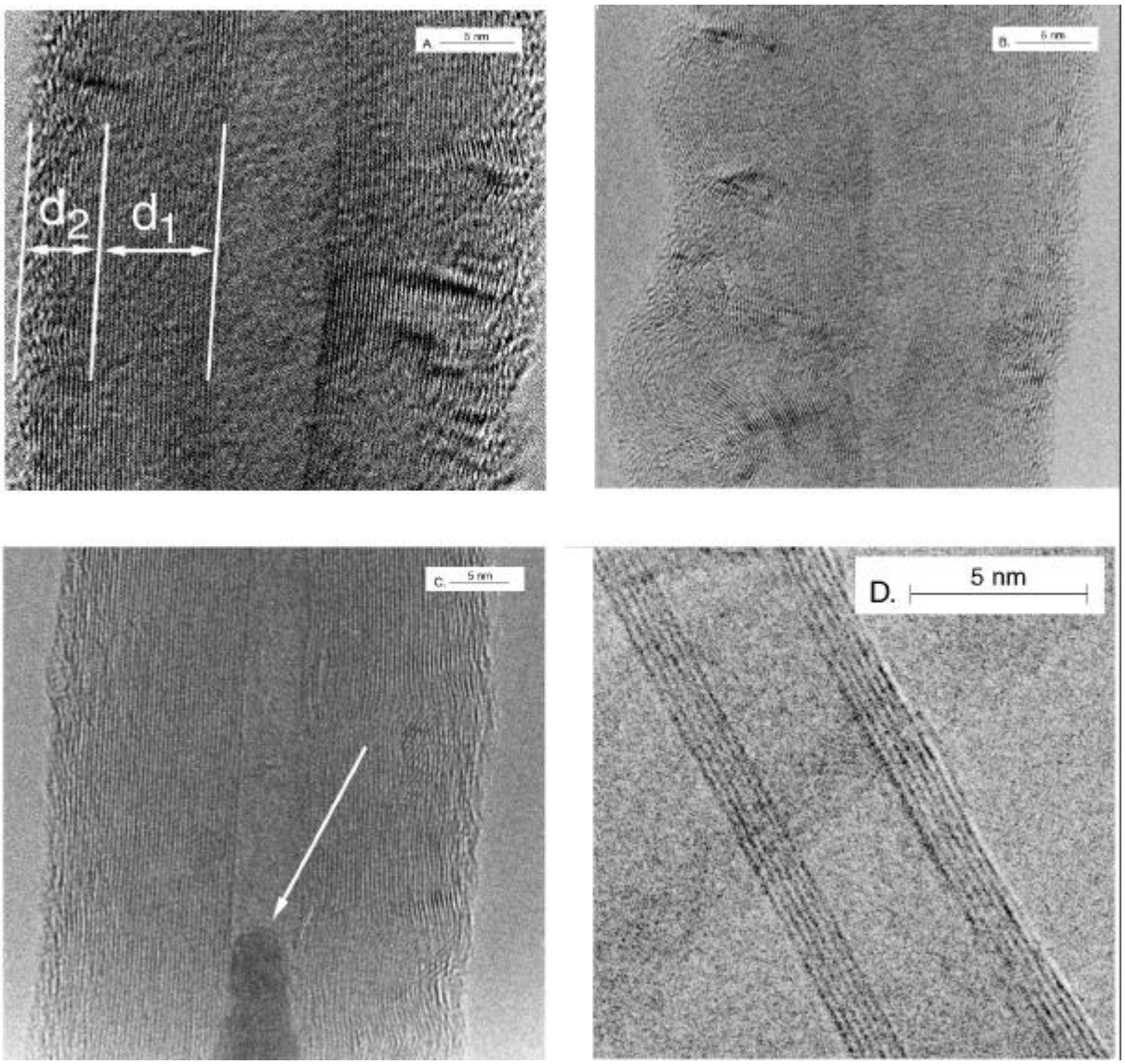


Figure 5. HREM images reveal the fine details of carbon nanotubes generated on sol-gel catalysts. (A) *Co,Si-ME-C-5.0* illustrates the double-wall structure where the thickness of the ordinary inner wall $d_1$ is typically twice the thickness of the outer block ($d_2$) of covering layers, (B) *Ni,Si-ME-C-5.0* and (C) *Co,Ni,Si-ME-C-2.5* illustrate typical defects (unordered wall growth and metal particle encapsulation marked by the arrow, respectively), while (D) shows the splendid quality of a tube produced on *Co,Fe,Si-ME-C-2.5*

### 4.1.2 Materials containing phosphotungstic acid

Even though the synthesis of carbon nanotubes is an interesting and promising new field of science, the overwhelming majority of present-day heterogeneous catalytic applications lays in the domain of acid-base catalysis. Sol-gel science offers two basic techniques to build acid function into the essentially neutral silica matrix: (i) co-hydrolysis with an aluminum source may grant zeolite-like acidity to the sample, or (ii) acid molecules

might be fixed in the catalyst. Conventional industrial acids like $H_2SO_4$ or HF are not suitable for this purpose, but heteropoly acids are. In this Section I shall describe a comprehensive study on the sol-gel immobilisaton of the widely used [102] $H_3PW_{12}O_{40}$ molecule in $SiO_2$. Results of a parallel series of experiments performed with catalysts prepared by conventional impregnation are also reported for comparison purposes.

*4.1.2.1 Characterisation*

Table 4. summarises certain properties of the samples synthesised as described in Section 3.1.1.2. The BET surface areas of the samples were very similar up to 50% PW12 content. As data in the Table prove, a small, gradual decrease in the BET surface area of the samples is seen. In contrast, samples containing 80% PW12 show a sudden drop of surface areas independently of the preparation method. It is also remarkable, however, that both the sol-gel and the impregnated sample having 80% PW12 possesses much higher surface area than the unsupported PW12, which may be due to the dispersion effect of silica as support.

| | | Optical density of pyridine IR band (A/mg) | |
|---|---|---|---|
| | Specific surface area ($m^2/g$) | Broensted | Lewis |
| *Si-ME-C-0* | 330 | 0.000 | 0.043 |
| *PW12,Si-ME-C-5* | 342 | 0.016 | 0.091 |
| *PW12,Si-ME-C-20* | 339 | 0.018 | 0.139 |
| *PW12,Si-ME-C-50* | 286 | 0.120 | 0.151 |
| *PW12,Si-ME-C-80* | 110 | n.a.* | n.a. |
| *PW12,Si-ME-IM-5* | 303 | 0.006 | 0.036 |
| *PW12,Si-ME-IM-20* | 281 | 0.035 | 0.078 |
| *PW12,Si-ME-IM-50* | 266 | 0.199 | 0.099 |
| *PW12,Si-ME-IM-80* | 89 | n.a. | n.a. |
| *pure PW12* | 22 | n.a. | n.a. |

* 80 w% and 100 w% PW12 samples could not be pressed into self-supporting wafers adequate for the FT-IR pyridine adsorption experiment.

Table 4. Summary of certain properties of samples investigated.

The specific surface area of our samples decreased with increasing content of the heteropoly acid. Compared to the samples prepared by Izumi *et al*. [103], we have found that our sol-gel samples had significantly lower surface areas, but the decrease in the surface areas from *Si-ME-C-0* to *Si-ME-C-50* is proportionally far less pronounced than that reported by Izumi. We attribute this beneficial effect to the presence of ethylene glycol in our preparation method acting as a pore structure directing agent. The decrease itself can be explained by the

different distribution of heteropoly acid on the silica surface (which has a surface area as small as 22 $m^2/g$) in the case of the impregnated samples. It is assumed that at low coverages the distribution of PW12 is molecular, whereas islands are formed and the surface area decreases at higher coverages since the pores are partially blocked. At even higher coverages crystallisation of PW12 takes place and it fills the pores of the support. For the sol-gel specimens we can explain the reactions taking place upon increasing dosage of PW12 as follows. The low PW12 content does not influence the BET areas since it has only slight effect on the sol and gel formation. Higher initial acid amount in the system influences the gel formation and thereby the surface area of the product. Giving 80% phosphotungstic acid to the gelating mixture results in a solid sample showing much lower surface area that is due to the severe influence on the rate of gelation and thereby, to the characteristics of the resulting specimen.

In Figure 6. the XRD patterns of specimens prepared by the sol-gel and conventional impregnation methods are compared. It is clearly seen that IM samples show reflections due to crystalline PW12 on their surface. The higher the PW12 loading the more intensive reflections appear in the pattern. For the sample having only 5% heteropoly acid no clear reflection was found. This behaviour suggests that the PW12 is present on this sample in molecular distribution or in very small clusters undetectable by XRD. Contrary to the features observed for the impregnated materials, samples prepared by the sol-gel procedure do not have any distinct reflections. This indicates that the acid is probably finely dispersed in these samples and has no opportunity to build clusters exhibiting XRD patterns.

XRD patters are in accordance with the features observed by BET measurements. The XRD pattern of supported samples show characteristic diffractions at the crystal face distances due to the crystalline HPWA [104, 105]. At low coverages the quantity of PW12 is not sufficient enough to form clusters or crystallites. At medium coverages first cluster formation occurs resulting in sharp XRD reflections, while at even higher coverages distinct crystalline phases are formed exhibiting appropriate XRD patterns.

The sol-gel materials have no XRD features characteristic of the PW12 phase in crystalline forms. It follows from this that PW12 is present in these samples in very high dispersion. However, from the XRD and BET measurements alone, a reasonable explanation cannot be given for these features.

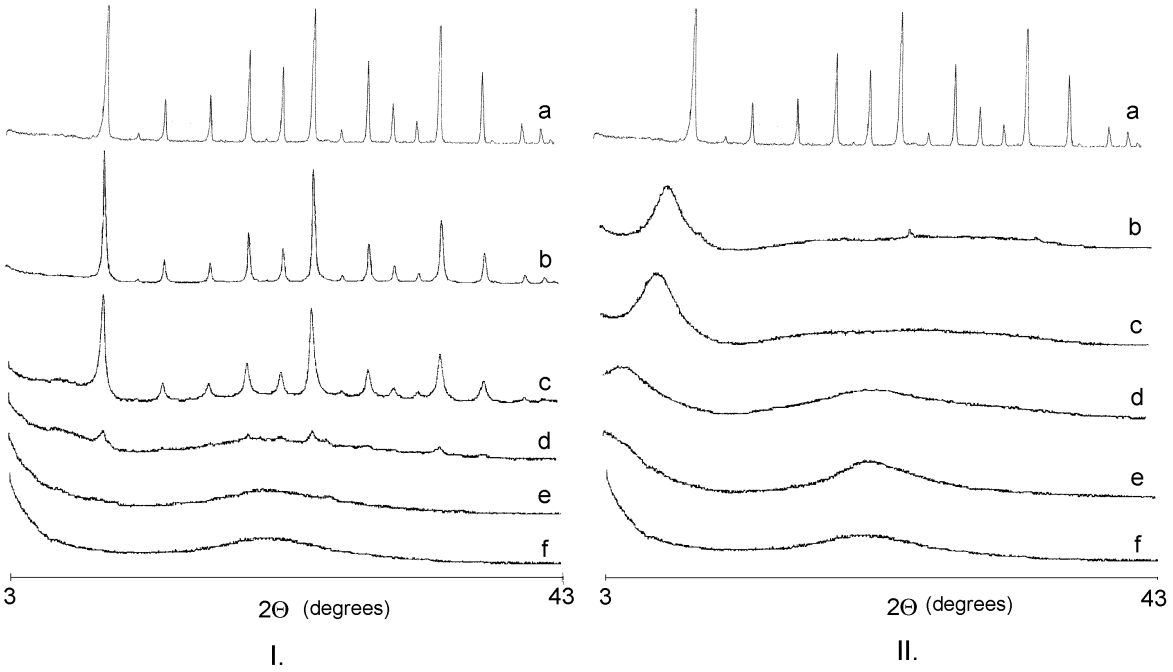


Figure 6. XRD profiles of impregnated (*-ME-IM-* series, Part I) and as-synthesised sol-gel derived (*-ME-C-* series, Part II) PW12-$SiO_2$ composites. On both parts the heteropoly acid loading is indicated as follows: a: pure PW12, b: 80 w% PW12, c: 50 w% PW12, d: 20 w% PW12, e: 5 w% PW12, f: pure silica (*Si-ME-C-0*)

The thermal behaviour of supported and sol-gel samples were completely different. For the supported samples the main processes resulting in weight loss took place below 673 K. As can be seen in Figure 7. an unresolved peak is found around 596 K and a second sharp peak at 448 K. These weight losses may be due to dehydration of the support and the heteropoly acid. At higher temperatures several much smaller steps are seen in the TG curve. Contrary to this feature two robust weight losses were observed for the sol-gel samples. The TG curve starts with a small step around 373 K probably due to dehydration. At 483 K a large step is seen followed by the second big step around 773 K. The low temperature step is due to the desorption of water and ethylene glycol while at higher temperature organic materials encapsulated into the gel structure are removed and the decomposition of PW12 takes place [106, 107]. No further weight loss was found at higher temperatures.

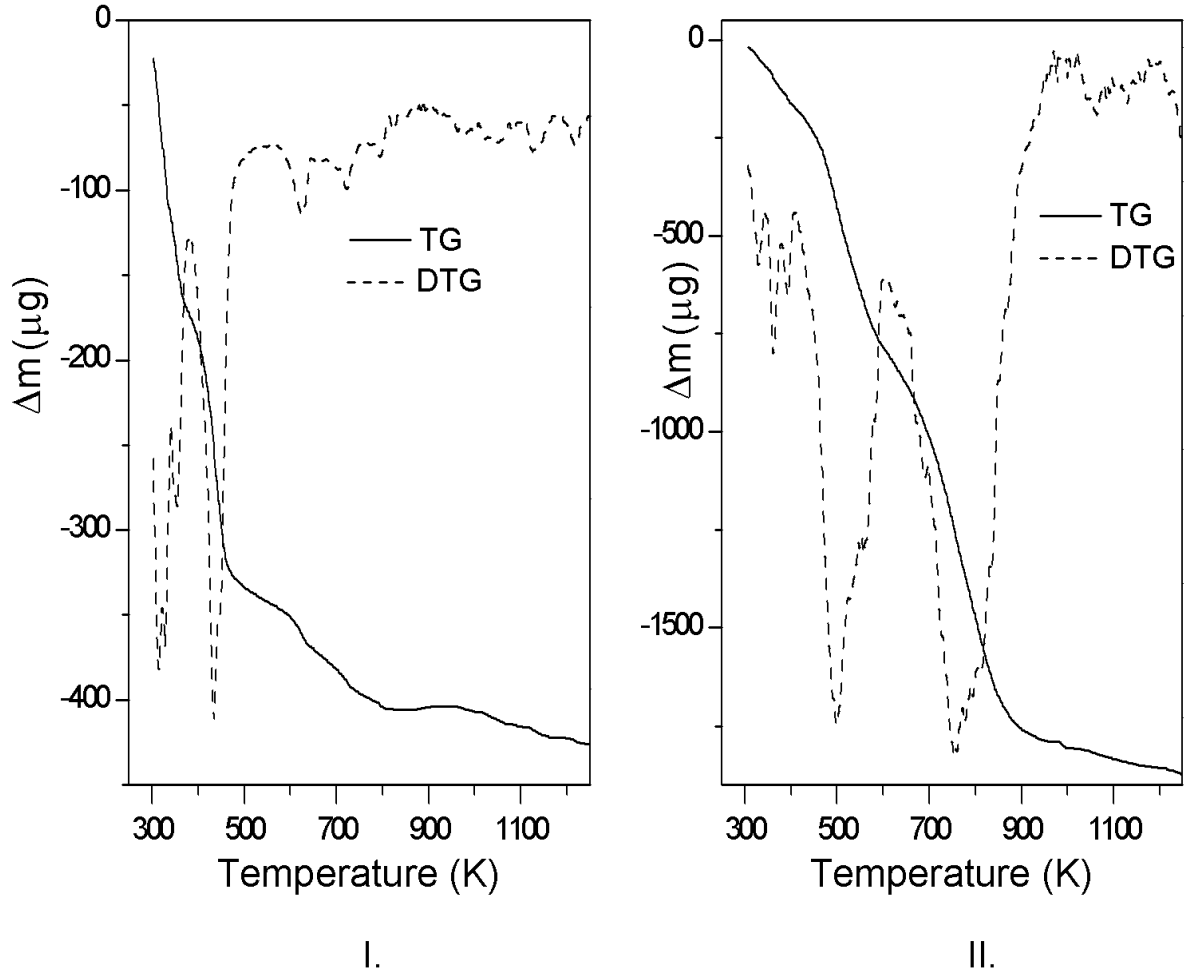


Figure 7. Thermal behaviour of the impregnated (*PW12,Si-ME-IM-50*, Part I) and as-synthesised sol-gel derived *(PW12,Si-ME-AS-50*, Part II) 50 w% PW12-$SiO_2$ composites.

The KBr matrix technique was used to compare the spectral behaviour of potential catalyst samples. Figure 8. shows three sets of spectra. Part I. of the figure shows the spectra of the impregnated materials. Bands observed at 1080, 995 (as a shoulder), 985, 878 and 795 $cm^{-1}$ are due to the characteristic vibrations of PW12. Here again, the higher the heteropoly acid concentration, the more intense bands appear. Quite similar spectra are obtained on the uncalcined sol-gel samples (see part II in Figure 2). Bands characteristic of ν(P=O), ν(W=O), and ν(W-O-W) vibrations are seen in these spectra. When we compare these spectra to those taken from sol-gel samples heat treated at 723 K, substantial changes appear. Neither the sample with 5% PW12 nor that with 80% PW12 contained well-resolved bands which were observed for pure heteropoly acid.

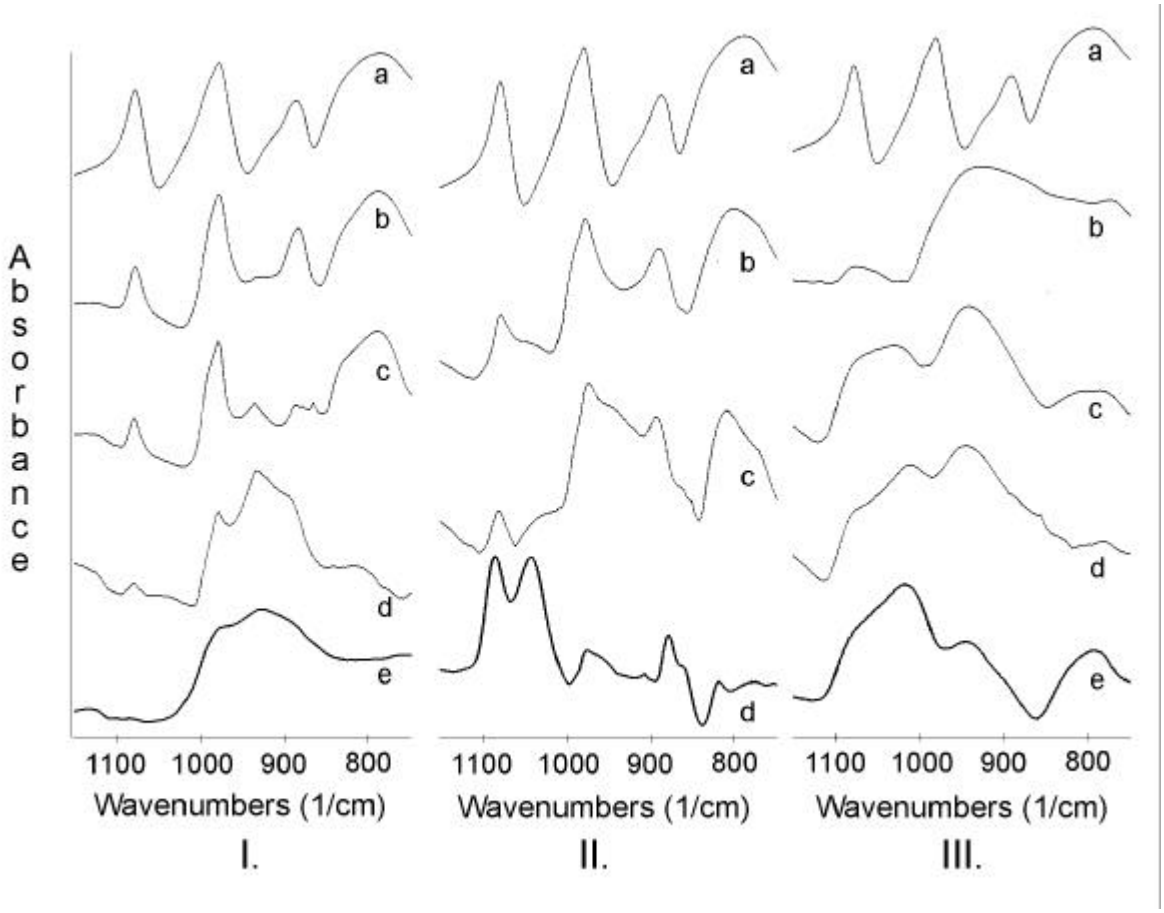


Figure 8. KBr IR spectra of the samples investigated. Part I: impregnated samples (a: *pure PW12*, b: *PW12,Si-ME-IM-80*, c: *PW12,Si-ME-IM-50*, d: *PW12,Si-ME-IM-20*, e: *PW12,Si-ME-IM-5*) Part II: as-synthesised sol-gel samples (a: *pure PW12*, b: *PW12,Si-ME-AS-80*, c: *PW12,Si-ME-AS-50*, d: *PW12,Si-ME-AS-5*) Part III: calcined sol-gel samples (a: *pure PW12*, b: *PW12,Si-ME-C-80*, c: *PW12,Si-ME-C-50*, d: *PW12,Si-ME-C-5*).

IR spectroscopy is a useful tool to detect various bonds in different matrices including silica. Band characteristic of the silica itself would be found in the 1450-1000 $cm^{-1}$ region [108], if the presented spectra were not deprived of the matrix features by spectral suntraction. Thus, the spectra recorded on the supported samples show the characteristic bands due to HPWA. These are $\nu_{as}$(P-O) 1080 $cm^{-1}$, $\nu_{as}$(W-O) 985 $cm^{-1}$, $\nu_{as}$(W-$O_c$-W) 890 $cm^{-1}$ in corner shared octahedra, and $\nu_{as}$(W-$O_e$-W) 810 $cm^{-1}$ in edge shared octahedra [109, 110, 111]. These characteristic absorptions are regarded as experimental evidence to the existence of HPWA molecules or molecular fractions such as phosphorous oxides and/or tungstate ions on the surface.

The spectral characteristics of the sol-gel samples are different from those of the impregnated materials. There are well-resolved IR bands on specimens that were not subjects

of heat treatment. However, no separated IR absorptions are seen on heat-treated samples. The necessity of heat treatment can be understood when we think of the fact that sol-gel samples contain quite a high amount of organic template materials, which should be burned off. When the treatment in air or oxygen takes place below 723 K, we may not be completely sure that all the organic materials are extracted from the inorganic matrix. The question arises, what is the optimal calcination temperature where all organics are removed and the added PW12 remains intact. Is there such a temperature? To make a compromise, we can choose a lower temperature taking the risk that the sample contains some residual organic compounds. This could cause difficulties for reactions sensitive to catalyst impurities. In this study we selected a higher temperature than suggested by the thermal analysis of pure PW12. As we treat the catalysts at a temperature above the decomposition temperature of HPWA, bands due to HPWA may not be expected. In fact, the IR bands due to the presence of HPWA cannot be seen. Nevertheless, as the catalytic tests show (Section 4.1.2.2), the acidity of samples is somehow preserved.

$^{29}$Si MAS NMR spectra presented in Figure 9. for the calcined sol-gel series were recorded in order to monitor the changes of the matrix structure initiated by the sol-gel PW12 incorporation. Fourier self-deconvolution followed by spectral decomposition [112] revealed that while in *Si-ME-C-0* the dominant Si form is $Q_4$ (typically at d= -110.5 ± 0.6 ppm, band width ?H= 620 ± 85 Hz) silicon, the introduction of PW12 into the system considerably increases the amount of $Q_3$ (d= -101.3 ± 0.3 ppm, ?H= 540 ± 70 Hz) and even $Q_2$ (d= -91.2 ± 0.3 ppm, ?H= 460 ± 80 Hz) species. Results of the decomposition are detailed in Table 5. The $^{29}$Si MAS NMR spectra of the impregnated PW12-$SiO_2$ composites *PW12,Si-ME-IM-5…PW12,Si-ME-IM-80* were practically identical to that of *Si-ME-C-0*, therefore, they are not presented here.

| | $Q_2$ (%) | $Q_3$ (%) | $Q_4$ (%) |
|---|---|---|---|
| *Si-ME-C-0* | 2.1 | 19.0 | 78.8 |
| *PW12,Si-ME-C-5* | 6.0 | 37.1 | 56.8 |
| *PW12,Si-ME-C-20* | 6.2 | 39.5 | 54.3 |
| *PW12,Si-ME-C-50* | 6.2 | 41.6 | 52.2 |
| *PW12,Si-ME-C-80* | 6.8 | 41.7 | 51.5 |

Table 5. $^{29}$Si MAS NMR analysis of the distribution of various Si species in sol-gel derived composites

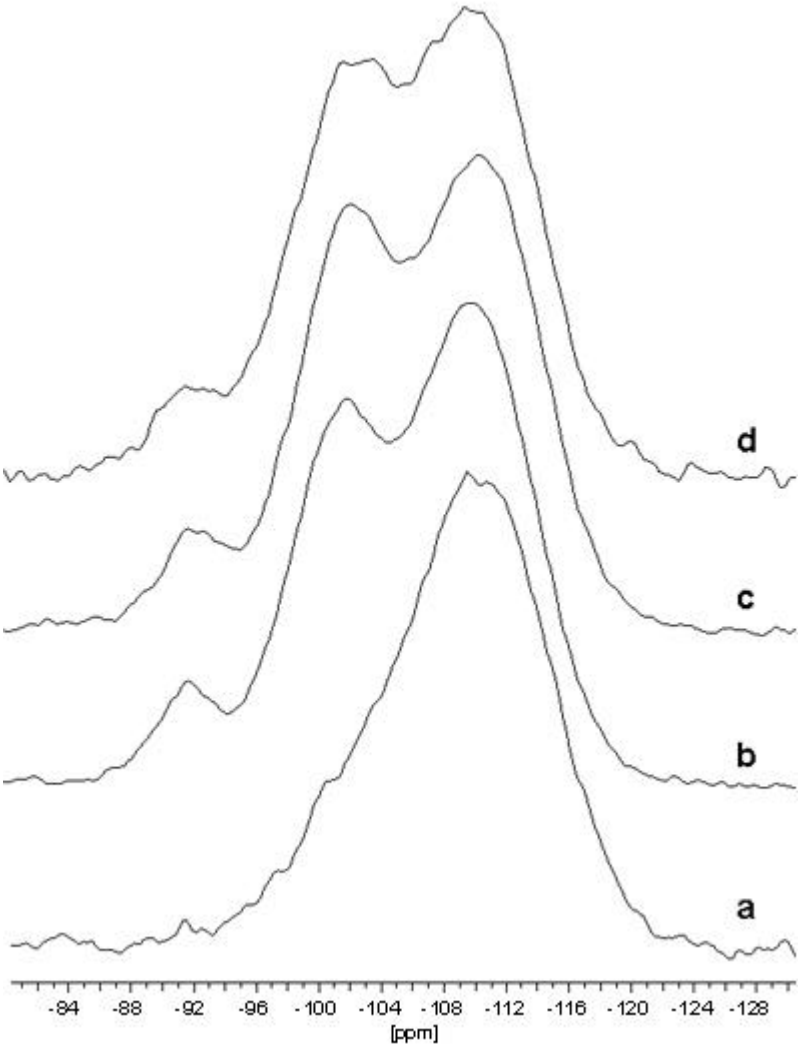


Figure 9. $^{29}$Si MAS NMR spectra of sol-gel derived composites

Conventional impregnation does not change the structure of the catalyst: PW12 crystallites are deposited onto the $SiO_2$ surface and are held there by secondary bonding forces. This is the reason why the NMR spectra of all impregnated samples are identical to each other and to *Si-ME-C-0*.

In the case of sol-gel PW12 incorporation, the heteropoly acid is chemically attached to the surface. In our opinion a covalent bond is generated between the support and the PW12 *via* release of a $H_2O$ molecule. This hypothesis is fully supported by NMR data in Table 5.: as low as 5 w% PW12 is enough to lower the $Q_4/Q_3$ ratio from 4.15 to 1.53. The reason for this change is that heteropoly acid molecules are bonded to silicon atoms near the surface, thus decreasing the number of Si's having 4 Si neighbours. We suppose that the increased percentage of the $Q_2$ Si atoms is not directly related to this phenomenon. Rather, it is thought to be caused by the more acidic media (PW12 is an ***acid*** after all), which is generally accepted

[24] to direct TEOS hydrolysis towards more open, linear structures. Increasing the PW12 contents of the precursor gel to 20 and 50 w% results in $Q_4/Q_3$ ratios of 1.37 and 1.25, respectively. According to Table 4. and Figure 6, this decrease is not accompanied by PW12 crystallite formation or a major drop in the specific surface area. A possible explanation comes from realising that any enlargement of heteropoly acid percentage reduces the silica contents of the composite. In other words: these samples contain highly dispersed PW12 just like *PW12,Si-ME-C-5* does, but their pore walls are thinner and that's why there is less and less $Q_4$ silicon in them. Sample *PW12,Si-ME-C-80* contains "too much" heteropoly acid. Even by the sol-gel technique we are not able to avoid PW12 crystallite formation visible by the XRD. These crystallites do not take up any more Si atoms as they grow on previously anchored acid cores. Therefore, the $Q_4/Q_3$ ratio in the *PW12,Si-ME-C-80* is 1.24 — practically identical to that of *PW12,Si-ME-C-50.*

*4.1.2.2 Finding the optimal heteropoly acid loading*

In the previous Section we have obtained experimental evidences about the successes of the sol-gel method in building the acid molecules into the samples. In order to decide if these catalysts have the potential to attract industrial attention or not, their acidity must be thoroughly investigated. These studies shall be described in the present Section in the following order:

- acidity measurements
- acidity test reactions
- catalyst stability analysis

Acidity of our heterogenised PW12 samples was determined using two conventional methods: pyridine adsorption and $NH_3$ TPD.

Pyridine was adsorbed on the samples and the absorptions of pyridine bound to acid sites were monitored by IR spectroscopy. The optical density of these vibrations giving rise to bands at around 1450 and 1540 $cm^{-1}$ was used as the measure of Lewis and Broensted acidity, respectively. Figure 10. shows two spectra due to pyridine adsorbed on samples prepared by impregnation and by the sol-gel method. The spectrum of sol-gel silica as a reference sample is also depicted.

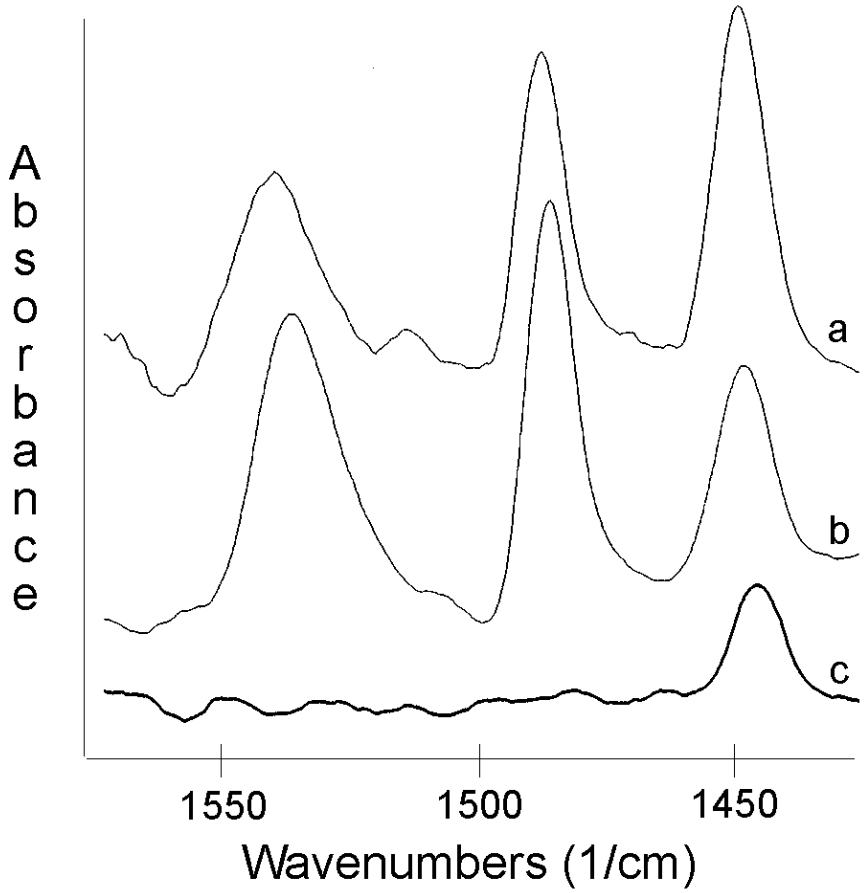


Figure 10. Differential pyridine adsorption IR spectra of "a": impregnated 50 w% PW12 composite *PW12,Si-ME-IM-50*, "b": 50 w% sol-gel composite *PW12,Si-ME-C-50* and "c": pure $SiO_2$ reference *Si-ME-C-0*.

These spectra show that both Lewis and Broensted acid sites exist on both series of samples containing PW12. It was a general observation that the sol-gel samples contained somewhat less Broensted acidity than the impregnated samples of identical initial PW12 content. The concentration of Lewis acidity showed a reverse trend: on IM samples the concentration of such acid sites proved to be lower. The silica support itself contained no Broensted acidity and only a small amount of Lewis acid sites was detected. The optical density of both Lewis and Broensted sites corresponding to pyridine bound are summarised in the last two columns of Table 4. On the basis of this data alone, samples with high PW12 loading would seem to be more appealing than those with low acid content.

A somewhat more detailed picture could be obtained *via* ammonia TPD. These measurements revealed that negligible ammonia was adsorbed on silica used as both support and matrix for the sol-gel preparation method. From samples containing PW12, ammonia desorbed in two steps as it was published by Kapustyn *et al.* [113]. The low temperature

desorption peak generally appeared between 543 and 639 K, while the high temperature one between 665 and 860 K. The detailed results are depicted in Figure 11.

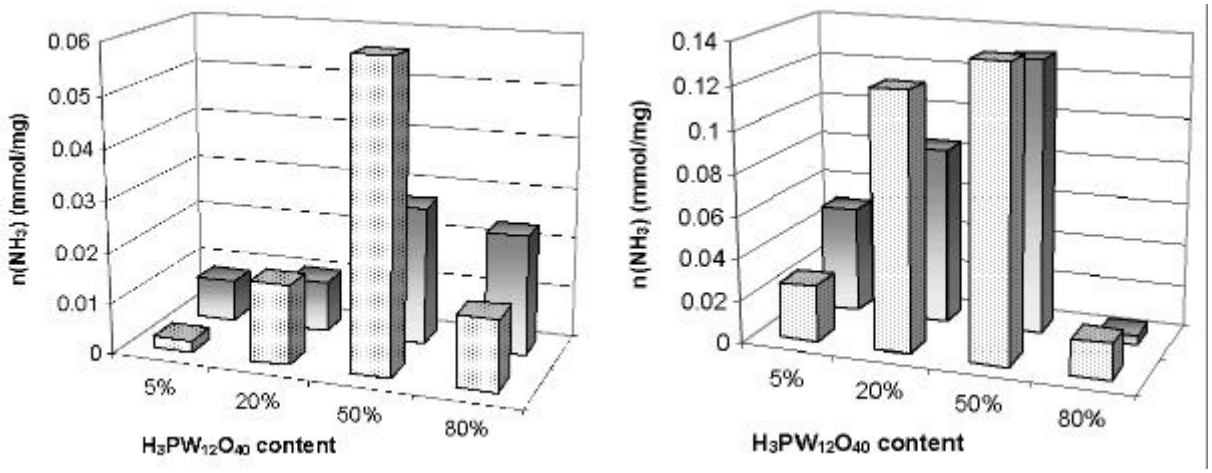


Figure 11. Integrated area of the low temperature (Part I) and high temperature (Part II) peak in the $NH_3$ TPD profiles of the samples. Hatched bars denote impregnated sampes (*-ME-IM-* series) and dotted bars sol-gel samples (*-ME-C-* series).

The area under both the low and the high temperature desorption peaks passed through a maximum with the increasing concentration of heteropoly acid. The largest peak areas were found for samples containing 50% PW12, indicating that an optimum in the acid amount exists.

It is widely accepted that the most sensitive method to characterise the acid-base properties of a catalyst is to use an appropriate, selective test reaction. Such possible test reactions are the skeletal isomerization of cyclopropane to propene, the dehydration of methanol to dimethyl ether, or the isomerization of 1-butene to 2-butenes. We chose the last reaction since the initial ratio of the *cis* and *trans* isomers gives information not only about the acidity but also on the basic character of the catalyst, if there is any. The initial ratio of *cis* and *trans* 2-butene was checked in each measurement and was always found to be close to unity. Therefore, we can conclude that it was indeed the man-made acidic function and not some spontaneously formed basic centre that catalysed the isomerisation of 1-butene. Consequently, it is correct to regard the partial pressure drop of 1-butene as a measure of the propagation of the chosen test reaction. Data measured for both types of samples are shown in Figure 12. The numerical values corresponding to the speed of the reaction are presented in Table 6.

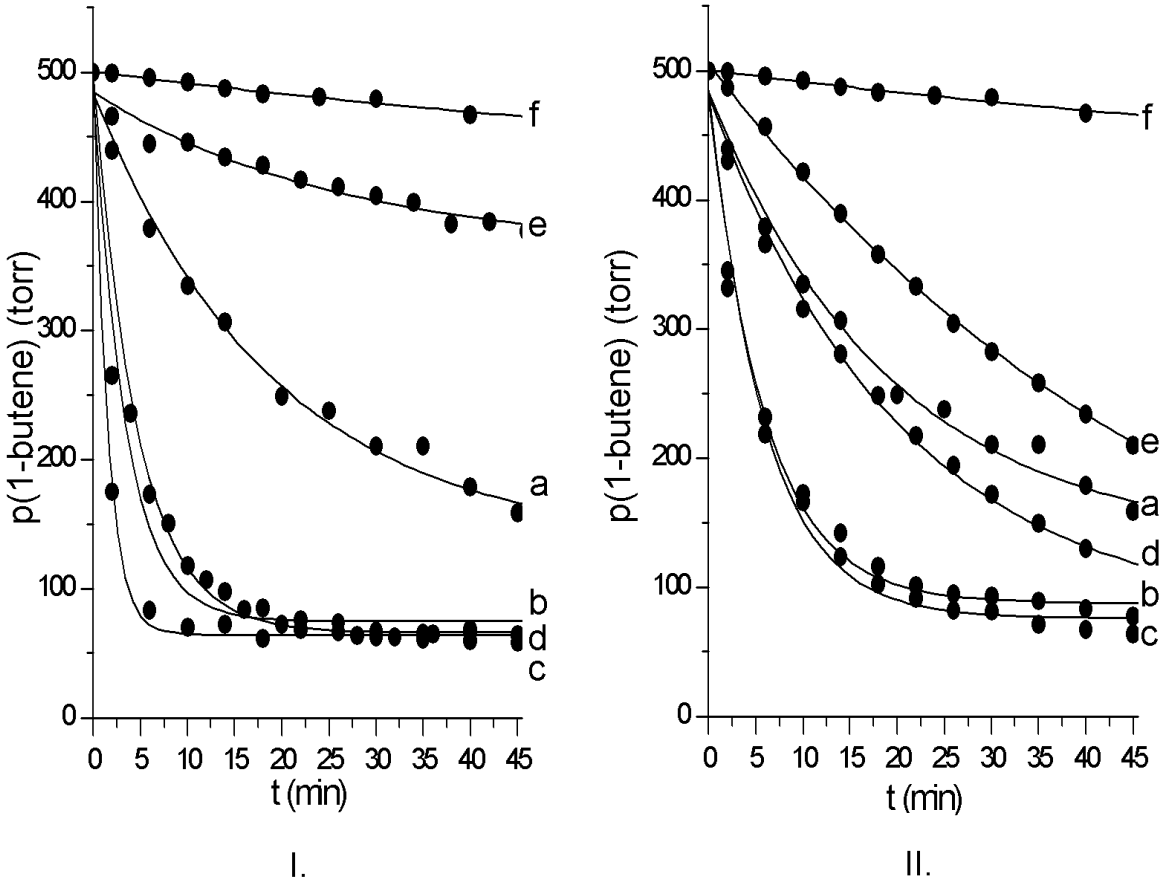


Figure 12. Kinetic curves of the 1-butene isomerisation reaction over impregnated (-*ME-IM*- series, Part I) and sol-gel derived (-*ME-C*- series, Part II) PW12-$SiO_2$ composites. On both parts the PW12 loading is indicated as follows: a: pure PW12, b: 80 w% PW12, c: 50 w% PW12, d: 20 w% PW12, e: 5 w% PW12, f: pure $SiO_2$ *Si-ME-C-0*.

| Sample | -dp/dt (Torr/min) | Sample | -dp/dt (Torr/min) |
|---|---|---|---|
| *Si-ME-C-0* | 0.96 | *Si-ME-C-0* | 0.96 |
| *PW12,Si-ME-IM-5* | 3.85 | *PW12,Si-ME-C-5* | 10.51 |
| *PW12,Si-ME-IM-20* | 91.53 | *PW12,Si-ME-C-20* | 19.12 |
| *PW12,Si-ME-IM-50* | 298.10 | *PW12,Si-ME-C-50* | 65.77 |
| *PW12,Si-ME-IM-80* | 113.70 | *PW12,Si-ME-C-80* | 58.76 |
| *pure PW12* | 14.78 | *pure PW12* | 14.78 |

Table 6. Initial velocity of the 1-butene isomerisation reaction on various samples expressed as the time derivative of the pressure drop in the kinetic curve

It is clear from the data that both types of materials contain working acid centres, but the impregnated samples are more active than their sol-gel counterparts. This is probably caused by the fact that each acid site generated by impregnation is accessible for the reactants

which is not the case for sol-gel samples, where some acid clusters could be incorporated into closed pores for example.

The information we have obtained so far indicates that the best catalyst studied in this Section is the one that is conventionally impregnated with 50 w% PW12. On the other hand, heteropoly acids are known for their splendid solubility in polar media (ethanol, water etc.). Since catalyst stability (that is, the ability to operate at the same performance level for a long time) is generally considered to be even more important than activity, we must examine if our catalysts are able to endure polar solvents without losing their PW12 contents. If not, they can not be used as catalysts of liquid phase reactions.

Both the *PW12,Si-ME-IM-50* and the *PW12,Si-ME-C-50* sample was treated with an 1:1 ethanol:water mixture by stirring at room temperature for 2 hours, followed by drying at 353 K overnight. In Figure 13. XRD patterns of the samples are seen.

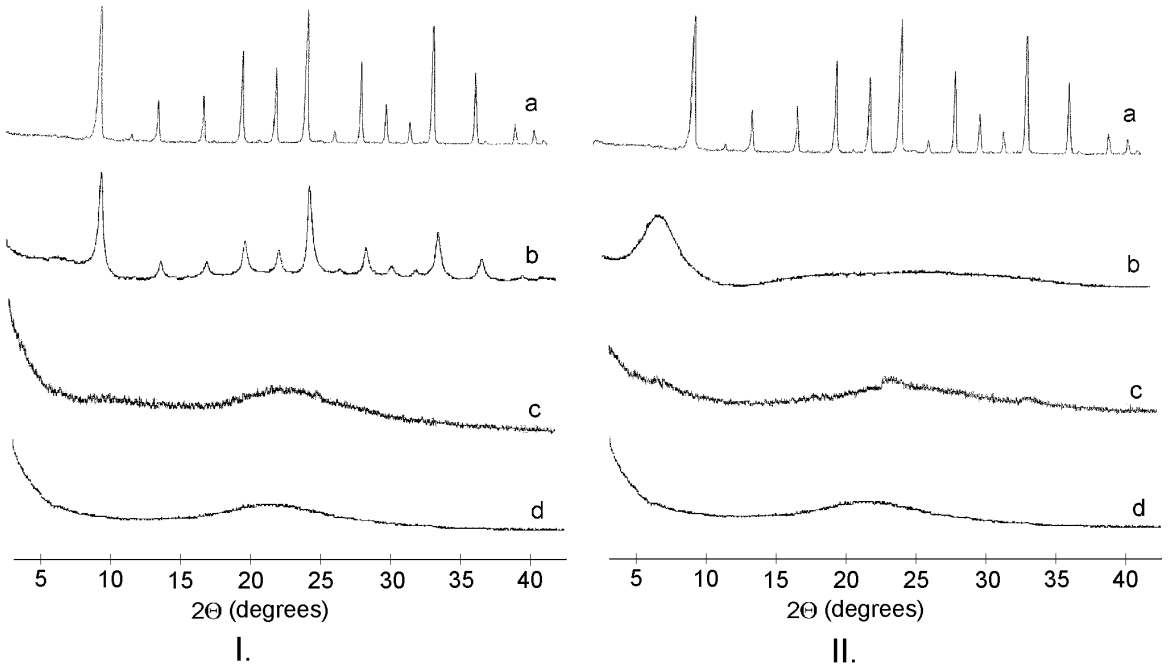


Figure 13. Solvent resistance of the 50 w% impregnated (*PW12,Si-ME-IM-50*, Part I) and sol-gel derived (*PW12,Si-ME-C-50*, Part II) PW12-$SiO_2$ composites studied by XRD. On both parts the of the figure, „a" denotes the profile of the pure PW12, „b" is the profile characteristic to the material before treatment, „c" is the profile after treatment in $H_2O$:EtOH and „d" is the profile of the pure $SiO_2$ *Si-ME-C-0*.

It is obvious that washing the sample with 1:1 water–ethanol mixture results in a decrease in the loading of PW12 for the impregnated samples. This is not unexpected, since

PW12 dissolves easily in both components of the solution. The situation, however, is completely different for the sol-gel catalysts. PW12 cannot be dissolved from these samples, since it is present either as finely dispersed, strongly bonded component or as partially or completely decomposed material showing catalytic activity in acid catalysed reactions.

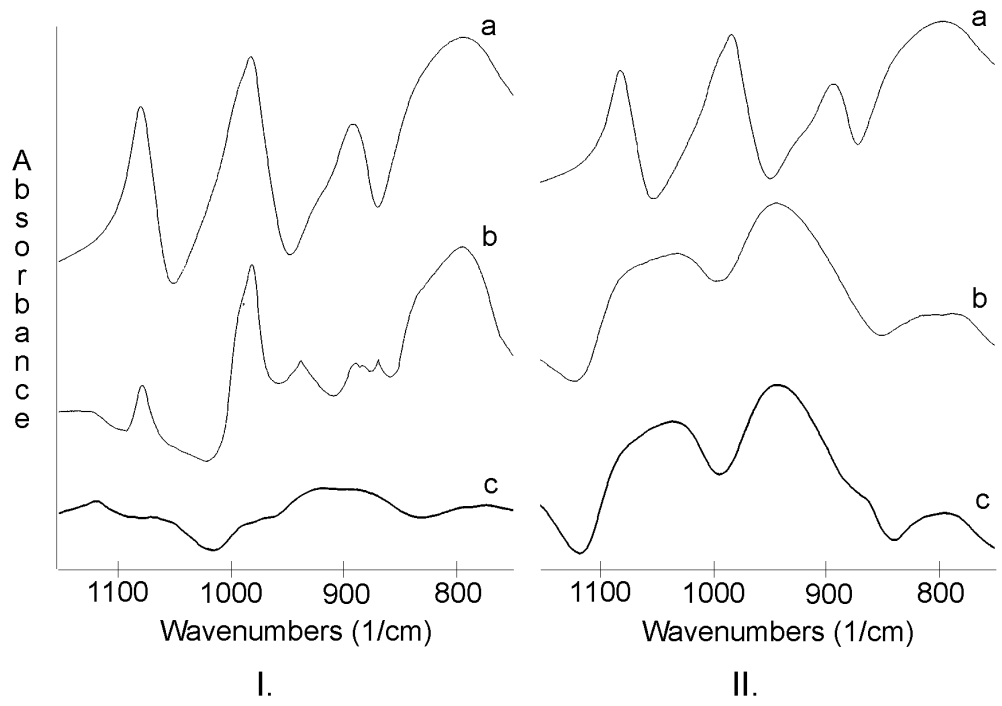


Figure 14. Solvent resistance of the impregnated (*PW12,Si-ME-IM-50*, Part I) and sol-gel derived (*PW12,Si-ME-C-50*, Part II) 50 w% PW12-$SiO_2$ composites studied by KBr IR. "a": pure PW12 , "b" spectrum of material before and "c" after treatment in $H_2O$:EtOH.

As Figure 14. shows no bands in the IR spectrum of the washed impregnated material due to the presence of PW12 are seen. It follows from this that no active component remained in the catalyst sample to act as acid catalyst in the test reaction. In contrast, the sample prepared by the sol-gel method shows an IR spectrum unchanged upon treatment in aqueous-alcoholic system. This result indicates the advantage of the use of such a sol-gel material as catalyst in acid-catalysed reactions.

The results of the test reaction applied to monitor the activity of the washed catalysts are seen in Figure 15., where the kinetic curves of the transformation of 1-butene to 2-butenes are depicted.

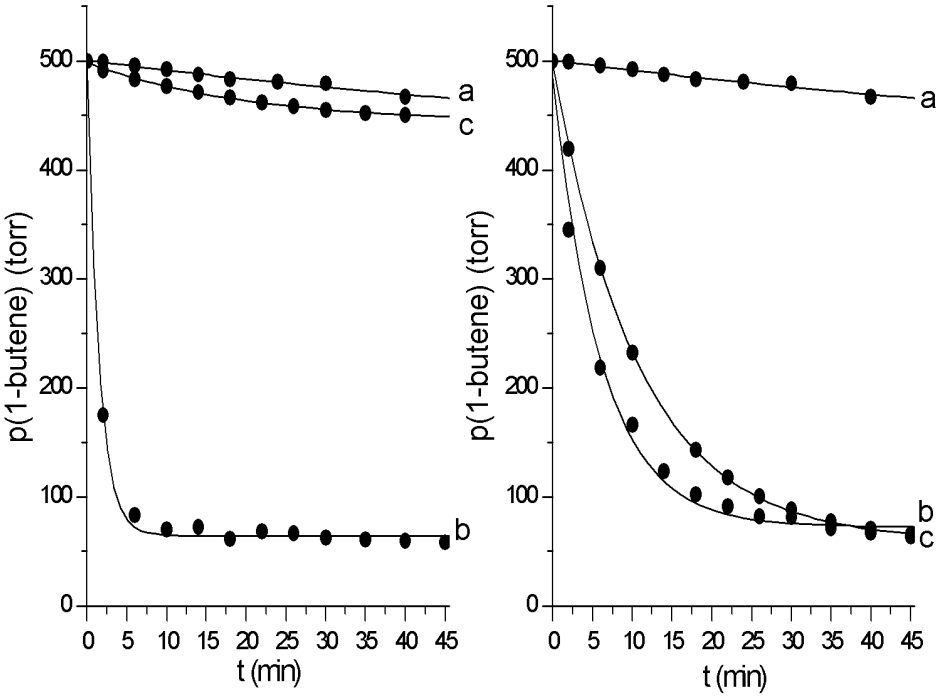


Figure 15. Solvent resistance of the impregnated (*PW12,Si-ME-IM-50*, Part I) and sol-gel derived (*PW12,Si-ME-C-50*, Part II) 50 w% PW12-$SiO_2$ composites studied by measuring their 1-butene isomerisation activity. On both parts, „a" denotes pure $SiO_2$ *Si-ME-C-0*, „b" is the kinetic curve before and „c" after treatment in polar media.

| Sample | -dp/dt (Torr/min) | Sample | -dp/dt (Torr/min) |
|---|---|---|---|
| *Si-ME-C-0* | 0.96 | *Si-ME-C-0* | 0.96 |
| *PW12,Si-ME-IM-50 b.t.** | 298.10 | *PW12,Si-ME-C-50 b.t.* | 65.77 |
| *PW12,Si-ME-IM-50 a.t.* | 2.75 | *PW12,Si-ME-C-80 a.t.* | 39.55 |
| *pure PW12* | 14.78 | *pure PW12* | 14.78 |

*b.t. : before treatment in 1:1 water:ethanol mixture
a.t. : after treatment

Table 7. Effect of the treatment with polar solvent visualised through the time derivative of the initial pressure drop in the 1-butene isomerisation kinetic curves

These curves, as well as the numerical values presented in Table 7. clearly show that for the impregnated catalyst the activity of the washed sample decreased dramatically compared to its original activity. In a sharp contrast, the sol-gel catalyst exhibited almost the same catalytic activity after the washing procedure.

Summarising the results of this Section we may conclude that it is possible to generate acid sites in sol-gel silica samples by $H_3PW_{12}O_{40}$ incorporation. The optimum acid loading is

approximately 50 w%. The sol-gel derived catalysts suffer an activity loss compared to their conventionally impregnated counterparts, but this loss is counterbalanced by the gain in stability. In our opinion, this stability originates from covalent bonds between the heteropoly acid molecules and the silica matrix. This interaction allows mesoporous sol-gel PW12-$SiO_2$ composites to be used as catalysts in polar solvents, thus opening new fields where heterogeneous catalysis can take the place of traditional homogeneous reactions.

*4.1.2.3 PW12-$SiO_2$ composites as catalysts of Diels-Alder type reactions*

Quite a number of possible transformations come to mind when thinking about a suitable test reaction that could benefit from the use of sol-gel catalysts discussed in the previous Section. We have chosen the Diels-Alder type (4,2) cycloaddition reaction, because (i) it is a very useful tool of synthetic organic chemistry, (ii) it is traditionally performed using homogeneous Lewis catalysts like $AlCl_3$ etc., and (iii) it is generally performed in liquid phase. In this Section I present FT-IR spectroscopic evidence for the applicability of PW12-$SiO_2$ catalysts in the reaction of 1,3-cyclohexadiene and 2-propenal with results comparable to those achieved on conventional silica-alumina systems.

The key differences between our studies [114] and a similar work by Meuzelaar *et al* [85] are that (i) our catalysts are prepared in one-step sol-gel incorporation instead of impregnation, (ii) we attempt to utilise FT-IR spectroscopy for reaction monitoring instead of capillary GC and (iii) we have followed the reaction in the adsorbed phase, not in the gas phase. Although in the previous Section we have proved that the optimal PW12 loading is approximately 50 w%, in the present study samples containing 5 w% and 20 w% PW12 were used. The reason for this is that it is way easier to press wafers suitable for IR measurements from highly siliceous materials, and we know from the previous measurements that such samples already possess acid centres. The silica-alumina composite *Al,Si-ME-C-20* was also enrolled in the study so that one can compare the sol-gel results with results obtained on a sample very similar to generally accepted Diels-Alder catalysts like zeolites and clays.

Concerning catalyst acidity: sample *Si-ME-C-0* has a practically neutral surface, samples *PW12,Si-ME-C-5* and *PW12,Si-ME-C-20* possess considerable Lewis but no Broensted acidity and sample *Al,Si-ME-C-20* has both Lewis and Broensted acidic centres in commensurable amounts. Note that the PW12 composites were deliberately deprived of their Broensted acidity by using a high calcination temperature. In the literature it is accepted [115] that at the applied 873 K temperature phosphotungstenic acid suffers partial decomposition,

and therefore, the active catalytic centres are likely to be various oxide species and not Keggin type acid molecules.

All reactions were performed as described in Section 3.3.3. Examination of the gas phase spectra revealed no changes in either series, as only the additive spectrum of 1,3-cyclohexadiene and 2-propenal was visible. This phenomenon is most likely caused by the strong adsorption of both the reactants and the products on the catalyst surface. Although these species are probably removable by elevating the temperature of the cell, such experiments were not performed to avoid the oligomerisation of 2-propenal. For this reason only adsorbed phase spectra will be discussed further herein. All presented spectra were derived by subtracting the spectrum of the clean, activated catalyst wafer from the actual measurement.

In order to be able to use vibrational spectroscopy for monitoring catalytic reactions, one first has to find molecular parts that make the spectra of the reactants and products different from each other. It is visible on Scheme 6. that in our Diels-Alder reaction this is no easy task, as the reactants and the products possess very similar bonds and groups. Our experimental conditions and instrumentation are clearly inadequate to distinguish between *endo* and *exo* products, therefore no attempt shall be made to do so.

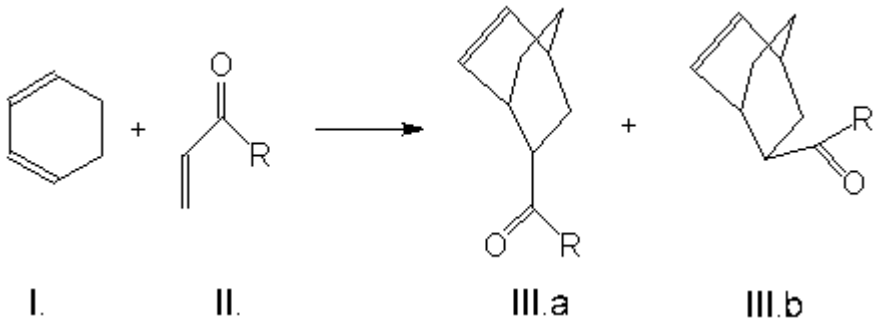


Scheme 6. Diels-Alder type reaction between 1,3-cyclohexadiene and 2-propenal. I: 1,3-cyclohexadiene, II: 2-propenal, III.a: *endo* bicyclo(2.2.2)-5-octene-2-carboxyaldehide, III.b: *exo* bicyclo(2.2.2)-5-octene-2-carboxyaldehide.

The key difference between reactants and products is that the carbonyl group is conjugated with the vinyl $CH_2$=CH- in 2-propenal, and this conjugation no longer exists in the product molecules. On this basis we can expect a 20-30 $cm^{-1}$ increase in the frequency of ν(C=O) as the reaction propagates. It should be noted that the conjugation of the C=C double bonds in 1,3-cyclohexadiene also disappears in the product. However, the frequency shifts of the ν(C=C) and ν(H-C=) bands corresponding to this structural change are smaller and —

especially in the adsorbed state — hard to identify, therefore in this paper the shift of the ν(C=O) band shall be used as a measure of the propagation of the reaction.

To make sure that this shift really measures a bimolecular catalytic reaction, let us first examine Parts I and II of Figure 16. describing two critical blank tests. It is easily noticeable that without a reaction partner 2-propenal is not transformed even on an acidic surface, and that even if both partners are present they are not able to react on a neutral surface.

On Parts III and IV of Figure 16. we verify if the spectral changes are really due to the reaction between our chosen reactants and not some surface decomposition product, for instance. Sample *Al,Si-ME-C-20* is covered by 2-propenal on Part III and by 1,3-cyclohexadiene on Part IV, and the reaction partner is added to this preadsorbed system. The reaction can be analysed on the basis of Part III as follows. The very intense band at 1693 $cm^{-1}$ is instantaneously reduced to a small shoulder. This process is matched by the appearance of an intense band at 1715 $cm^{-1}$, and is followed by the slower development of the band at 1725 $cm^{-1}$. Our interpretation of this phenomenon is that the strongly adsorbed 2-propenal molecules react nearly instantaneously with 1,3-cyclohexadiene and because of this the original 1693 $cm^{-1}$ band disappears and in the Diels-Alder reaction unconjugated C=O bonds absorbing at 1715 $cm^{-1}$ are formed. Since the temperature is not high enough for desorption (see above), the active sites of the catalyst are gradually poisoned by the products and this reaction stops. The gradual increase of the 1725 $cm^{-1}$ band is then explained by unwanted oligomerisation reactions taking place on the Broensted acid sites of the *Al,Si-ME-C-20* catalyst. A very similar picture appears if we add 2-propenal to preadsorbed 1,3-cyclohexadiene as shown on Part IV of Figure 16.

On the basis of these findings we may conclude that (i) a bimolecular heterogeneous catalytic Diels-Alder reaction occurs on the acidic *Al,Si-ME-C-20* surface, and (ii) the reacting partners of this reaction are indeed 2-propenal and 1,3-cyclohexadiene, otherwise the "c" spectra on Parts III and IV should be different. On Parts V and VI of Figure 16. the propagation of the reaction over *PW12,Si-ME-C-5* and *PW12,Si-ME-C-20* catalysts is depicted, respectively. Since in these experiments the reaction mixture was let onto a clean, activated surface, the band corresponding to adsorbed 2-propenal appears at 1693 $cm^{-1}$. Once again we witness the quick formation of the 1715 $cm^{-1}$ band indicating that the reaction is progressing. The Diels-Alder reaction seems to go faster on *PW12,Si-ME-C-20* than on *PW12,Si-ME-C-5* as indicated by the larger unconjugated:conjugated ratio on spectrum "b" on Part VI.

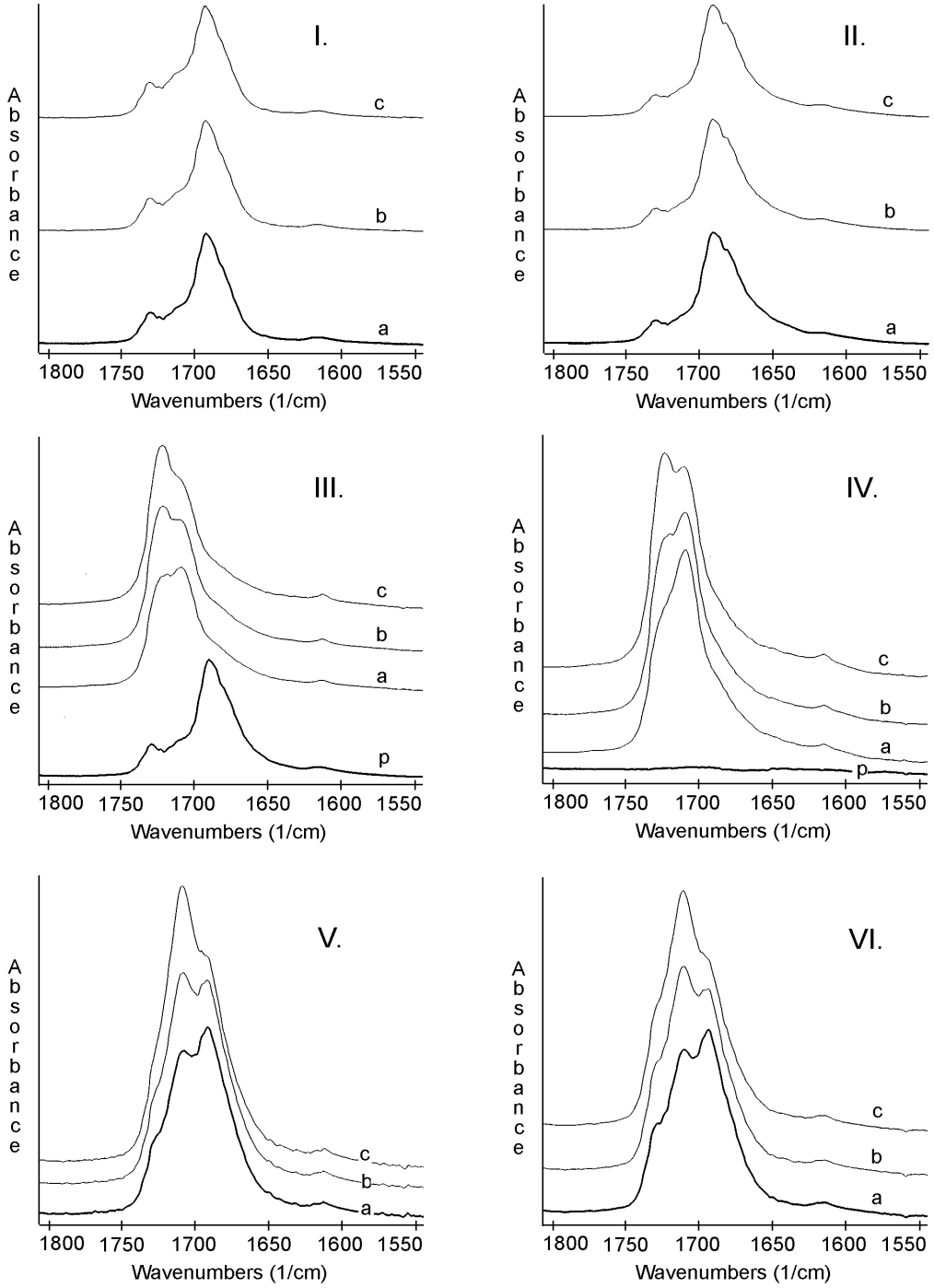


Figure 16. Time dependence of the fine structure of the ν(C=O) band. Part **I**: 2-propenal adsorbed on *Al,Si-ME-C-20*, Part **II**: reaction mixture adsorbed on non-acidic *Si-ME-C-0*, Part **III**: 1,3-cyclohexadiene added to 2-pronenal preadsorbed on *Al,Si-ME-C-20*, Part **IV**: 2-propenal added to 1,3 cyclohexadiene preadsorbed on *Al,Si-ME-C-20*, Part **V**: reaction taking place on *PW12,Si-ME-C-5*, Part **VI**: reaction taking place on *PW12,Si-ME-C-20*. On all six parts, "a", "b" and "c" denote the spectrum after 2, 10 and 40 minutes, respectively. On Part III and Part IV "p" denotes the spectrum of the preadsorbed species.

This finding agrees well with the larger number of Lewis acid sites in *PW12,Si-ME-C-20* as found by pyridine adsorption. The band at 1725 $cm^{-1}$ corresponding to unwanted side reactions is a mere shoulder in both series, which can be explained by the absence of Broensted acid sites in the PW12 composites.

In this Section we suggested an identification scheme [114] that can be used for the monitoring of Diels-Alder type reactions by FT-IR spectroscopy. Sol-gel derived silica-alumina and silica-heteropoly acid composites were both found to be active catalysts in the reaction of 2-propenal and 1,3-cyclohexadiene. Catalysts lacking Broensted acidity seem to be a more favourable choice for future experiments because no side reactions take place over them.

## *4.2 Macroporous materials*

### 4.2.1 Silica nanotubes

#### *4.2.1.1 Structure*

SEM images presented in Figure 17. prove that by adding DL-tartaric acid to the precursor sol and performing a shocking basic hydrolysis as described in Section 3.1.2.1 hollow tubular shapes could be prepared via the sol-gel route. These structures shall be referred to as "silica nanotubes" from now on. It should be noted that another phase consisting of aggregated non-porous silica spheres has also been formed along with the nanotubes. This phase is probably akin to the so-called Stober spherical silica [116]. On the basis of SEM pictures we estimate the average silica nanotube to have an outer diameter of 0.8-1.5 μm, inner diameter of 0.5-0.8 μm, length of 5-100 μm and the nanotube/aggregate ratio to be above 5. Analysis of the $N_2$ adsorption isotherm of *Si-NT-C-0* (presented in Figure 18.) revealed the major features of the nanotube pore structure, which are summarised in Table 8.

| | BET surface area ($m^2/g$) | Pore diameter (Å) | Pore volume (ml/g) | Micropore volume (ml/g) |
|---|---|---|---|---|
| *Si-NT-C-0* | 24 ± 2 | 1720 ± 61 | 0.26 ± 0.03 | 0.0018 ± 0.0002 |

Table 8. Most important characteristics of the pore system of the silica nanotubes in *Si-NT-C-0*

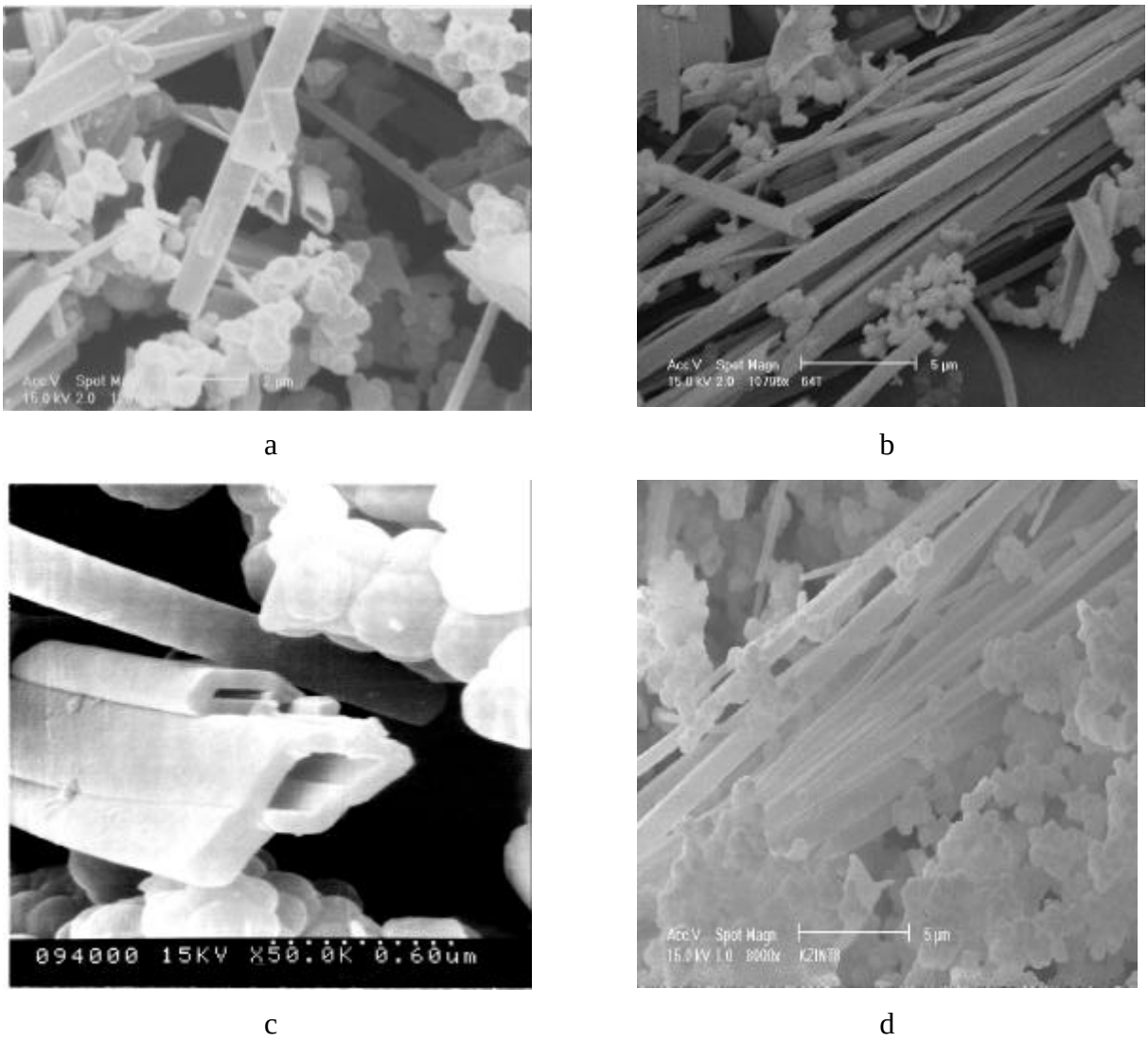


Figure 17. Four representative SEM pictures showing calcined silica nanotubes (*Si-NT-C-0*)

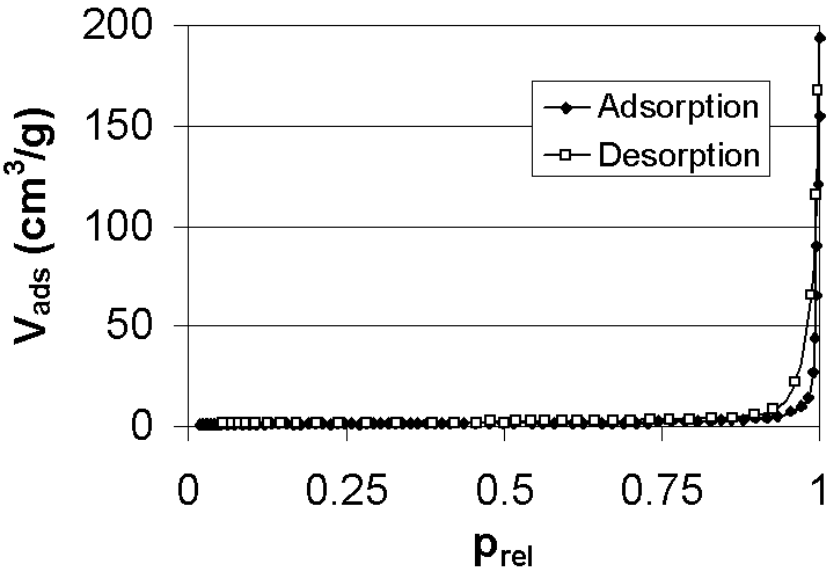


Figure 18. A typical $N_2$ adsorption-desorption isotherm of *Si-NT-C-0*

We have executed an optimisation plan [117] to get rid of the spherical silica phase and to increase the nanotube yield. Varied parameters were temperature, quality of mixing, Si to organic acid ratio, Si to water ratio and type of organic acid. Certain characteristic outcomes of these experiments are shown in Figure 19. It can be seen in the Figure that though experimental conditions do have the ability to slightly modify the appearance of the end-product, these minor fluctuations of quality can hardly be called "optimisation". Because of such lack of success, these attempts shall not be detailed here. However, there are two results worth mentioning: (i) we were able to scale up the original Nakamura process by a factor of 4, (ii) DL-tartaric acid was the ***only*** organic additive that directed gelation towards the nanotube shape.

Silica nanotubes exhibit practically no surface anomalies, only smooth flat walls. Besides the tubular shape, their key morphological feature is that they have angular cross section instead of a circular one. The origin of this rather unique (compared e.g. to the well-known circular carbon nanotubes) property is currently being debated. It certainly must be related to DL-tartaric acid somehow, since only the addition of this reagent resulted in nanotube formation. It is also clear that because of its small size DL-tartaric acid can not play the role of a conventional template molecule. Nakamura et al. [51] suggested that a "ladder-like" structure is formed from D and L tartaric acid molecules to serve as supramolecular template. However, it is rather dubious if the small amount of DL tartaric acid in the precursor solution can validate any model that assumes a fixed template-silica interaction.

In our opinion [118], tartaric acid molecules form quasi-flat sheets that can serve as templates for flat silica panels. This hypothesis is partially supported by the outcome of the conformational analysis of both tartaric acid isomers summarised in Figure 20. By rotating each molecule in a full circle at 1 degree/step around the $C_2$-$C_3$ axis and performing a constrained geometry optimisation at each point, we could realise that (i) the potential energy curves are mirror images of each other just as expected, (ii) the potential energy surfaces are rather complex with local minima at 101, 148 and 303 degrees (D isomer), and (iii) that there exist pairs of local minima that offer the possibility of H-bonding between a D and an L tartaric acid molecule. Moreover, in these special geometries it is possible to attach more tartaric acid molecules both to the carboxyl ends and to the hydroxyl "hands" of the DL adduct. In other words: the conformational analysis confirmed the energetic feasibility of large flat tartaric acid planes.

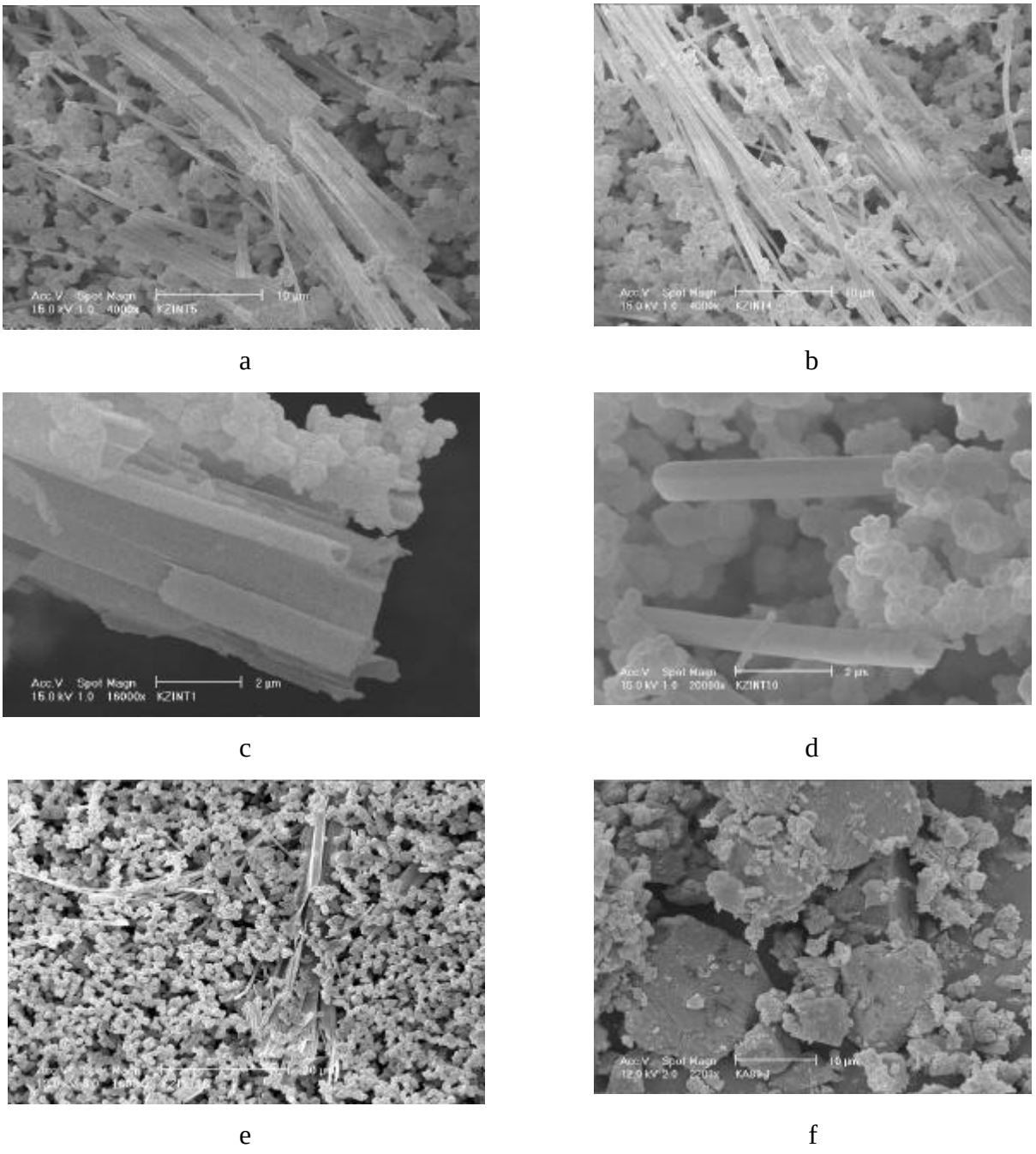


Figure 19. SEM results of experiments directed towards the optimisation of silica nanotube synthesis. a: original Nakamura process, b: × ½ amount DL-tartaric acid, c: ×2 amount DL-tartaric acid, d: elevated temperature (348 K), e: citric acid instead of tartaric acid, f: hydrolysis catalysed by acid instead of $NH_3$

After reaching a certain size, the silica planes are thought to detach from the tartaric acid sheet, which becomes ready for directing the formation of the next plane. The nanotube

formation is a secondary process occurring spontaneously when two planes meet. The steps of this proposed mechanism are visualised in Figure 21.

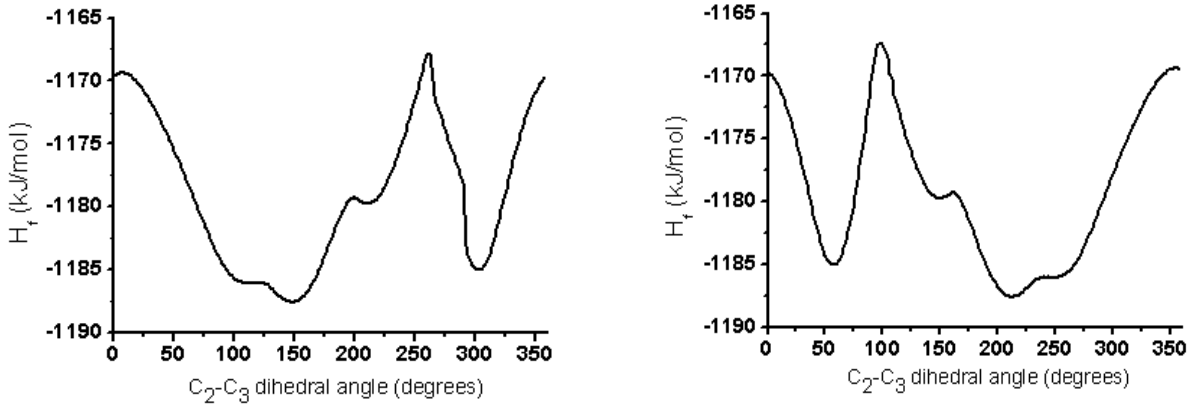


a b

Figure 20. Conformational analysis of D (a) and L (b) tartaric acid at the AM1 semi-emipirical level of theory

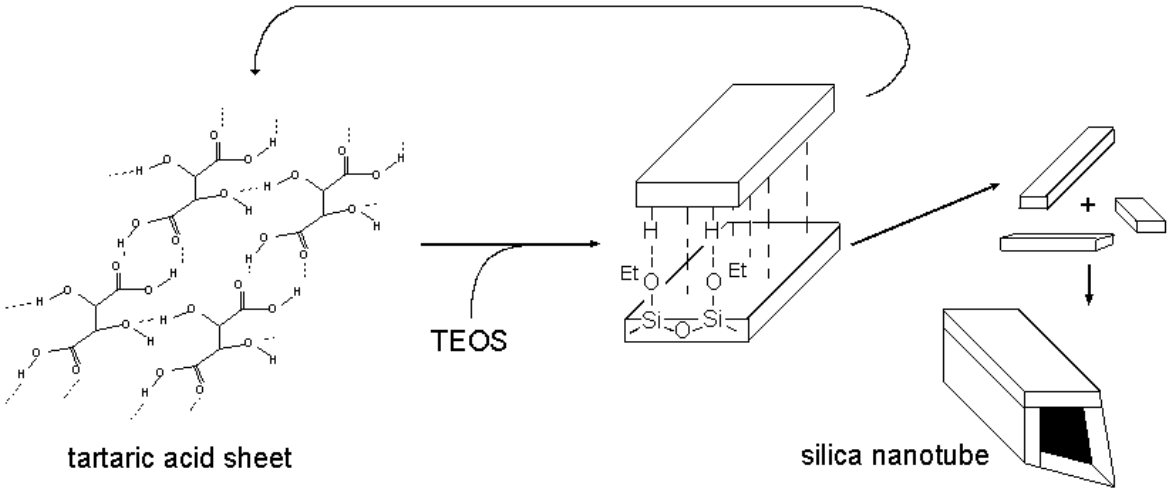


Figure 21. Proposed mechanism of silica nanotube formation

*4.2.1.2 Chemical properties*

In order to gain insight into the possibilities of catalytic applications, the heteropoly acid containing silica nanotube samples *PW12,Si-NT-C-5* and *PW12,Si-NT-C-20* were tested in our standard acidic test reaction: the isomerisation of 1-butene. The measured kinetic curves are presented in Figure 22.

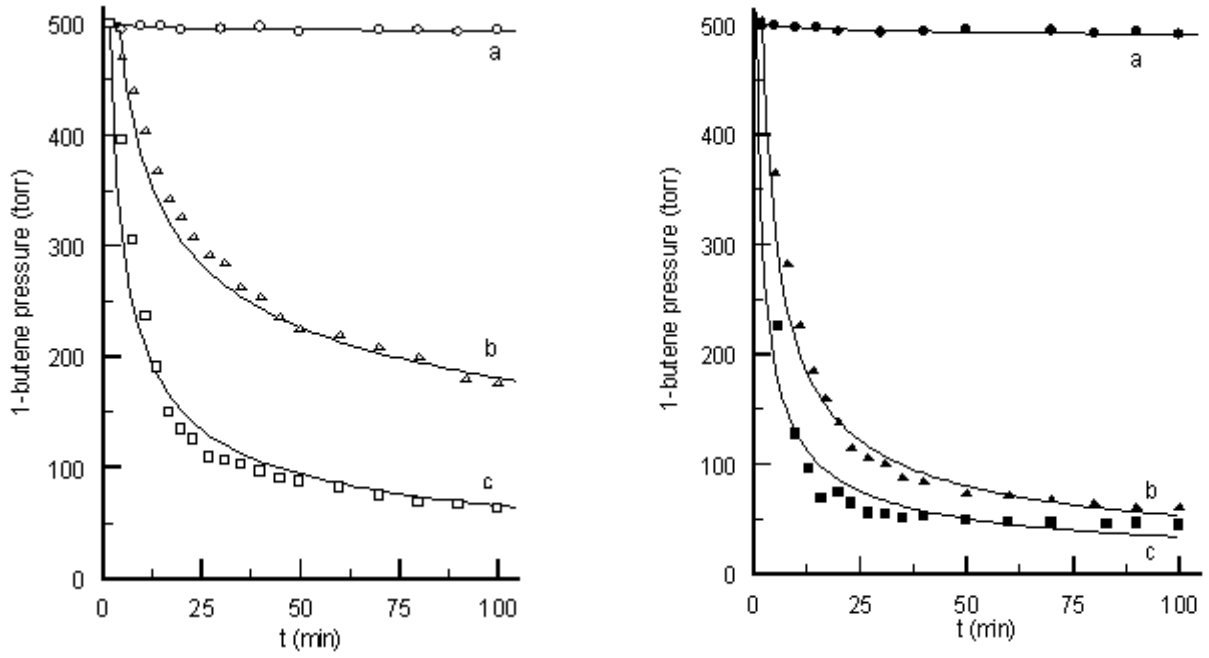


I. II.

Figure 22. Conversion of 1-butene into 2-butenes at 443 K (I) and 473 K (II) in a fixed bed recirculatory reactor. On both parts, *Si-NT-C-0*, *PW12,Si-NT-C-5* and *PW12,Si-NT-C-20* are labelled “a”, “b” and “c”, respectively.

The following observations [117] are readily made from the initial slopes of the curves:

- it is solely the heteropoly acid that grants the samples their catalytic activity.
- the influence of the elevated temperature follows the trend expected on the knowledge of basic reaction kinetics.
- the specific catalytic activity of the samples can be controlled by controlling the PW12 loading: the higher the heteropoly acid concentration, the faster the reaction is.

Just as in Section 4.1.2.2, the initial ratio of *cis* and *trans* 2-butene was checked and found to be close to unity in each reaction.

## 4.2.2 Silica foams

### *4.2.2.1 Structure*

In Figure 23. some characteristic pictures of the materials synthesised according to Section 3.1.2.2 are presented.

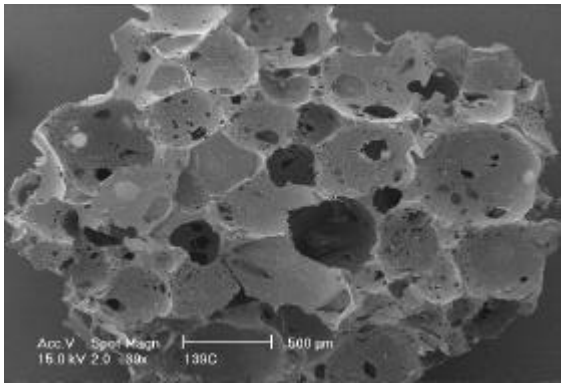


a

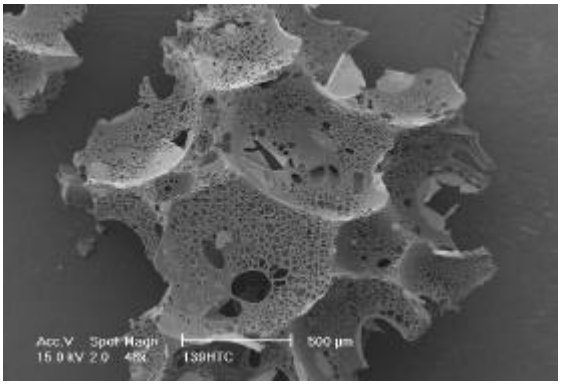


d

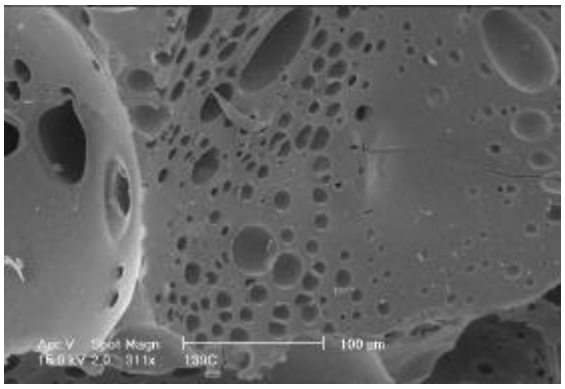


b

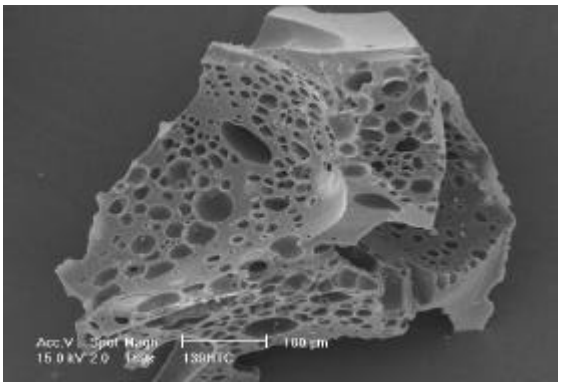


e

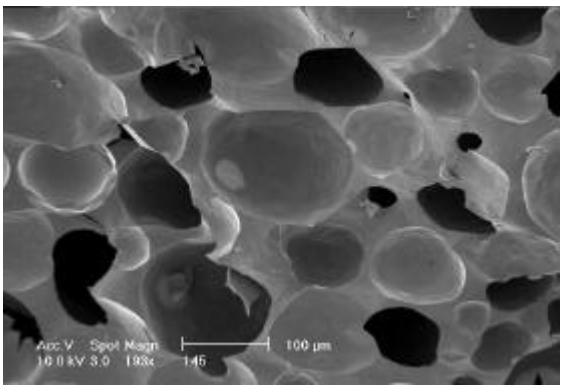


c

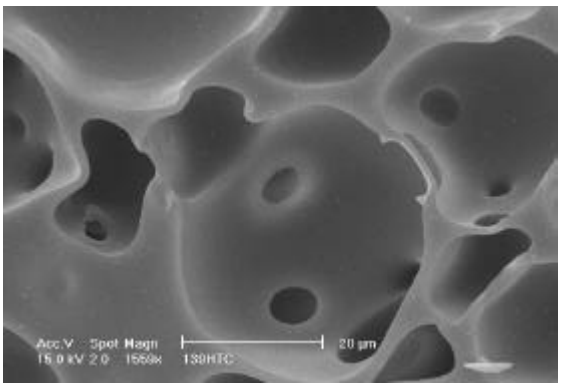


f

Figure 23. Representative images of *Si-FO-C-0* (a, b, c) and *Si-FO-HTC-0* (d, e, f) samples.

The silica foam was obtained as a monolith (apparent density after calcination: ~0.08 g/cm$^3$) sharing dimensions with the synthesis vessel. The diameter of the observed foam pores ranged from 4-6 mm to 2-5 μm. However, we are quite positive about the existence of even narrower pores, which could not be identified microscopically because of instrumental limitations. The hydrothermal treatment had no direct effect on foam morphology. Silica foam formation seems to be quite straightforward to explain: TEOS hydrolysis takes place in the walls of the foam raised by the heavy stirring of the aqueous detergent solution. A comprehensive discussion of the phenomenon was given by Bagshaw [52].

The major characteristics of the foam pore system were determined from $N_2$ adsorption isotherms like those shown in Figure 24. and are presented in Table 9. It is clear from these data that the foams are essentially mesoporous materials possessing very high surface areas.

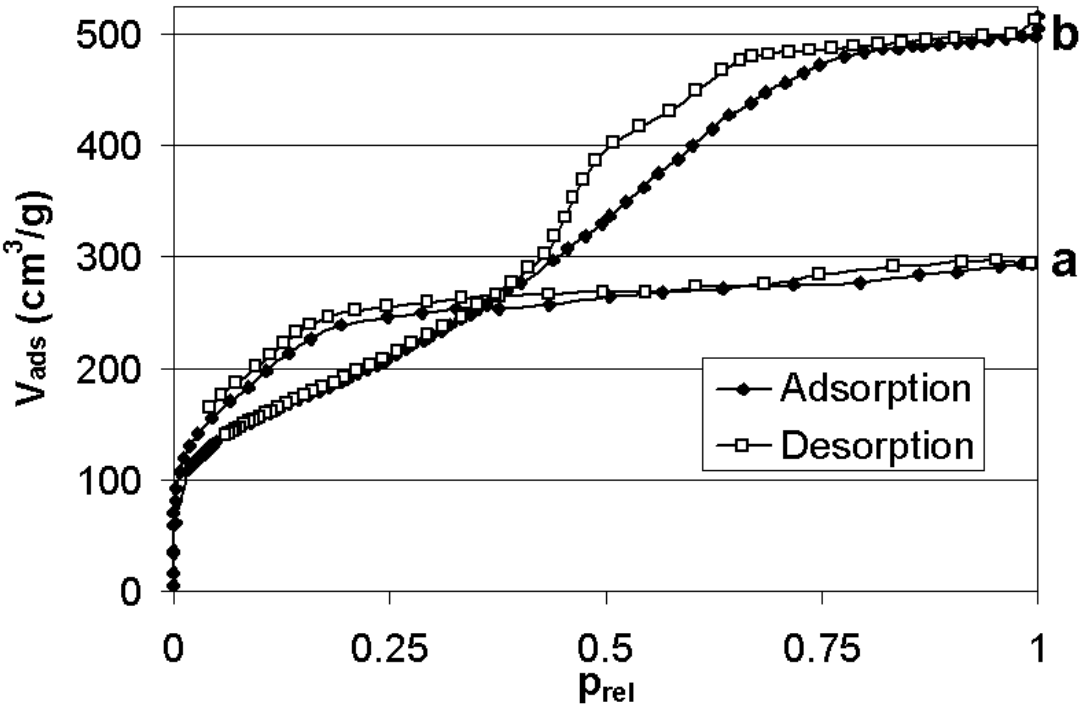


Figure 24. Typical $N_2$ adsorption isotherms of *Si-FO-C-0* (a) and *Si-FO-HTC-0* (b)

| | BET surface area (m$^2$/g) | Pore diameter (Å) | Pore volume (ml/g) | Micropore volume (ml/g) |
|---|---|---|---|---|
| *Si-FO-C-0* | 863 ± 6 | 36 ± 3 | 0.78 ± 0.15 | 0.064 ± 0.005 |
| *Si-FO-HTC-0* | 779 ± 6 | 43 ± 4 | 0.91 ± 0.22 | 0.053 ± 0.003 |

Table 9. Most important characteristics of the pore systems of silica foams

Considering the openness of the structures shown in Figure 23. and the extremely low apparent density, it is no surprise that freshly calcined silica foams are extremely sensible to physical pressure, fracture etc. To overcome this problem, hydrothermal treatment of the foams was suggested and is now generally applied. This is expected to enhance cross-linking of the walls and thus, to increase foam stability. However, direct experimental proofs of these beneficial effects are seldom found in the literature. Therefore, we have recorded the $^{29}$Si MAS NMR spectra of samples *Si-FO-AS-0*, *Si-FO-C-0* and *Si-FO-HTC-0* and performed Fourier deconvolution followed by multi-peak Gaussian decomposition to determine the percentages of different Si species [112] in the materials. The results are presented in Figure 25. and Table 10.

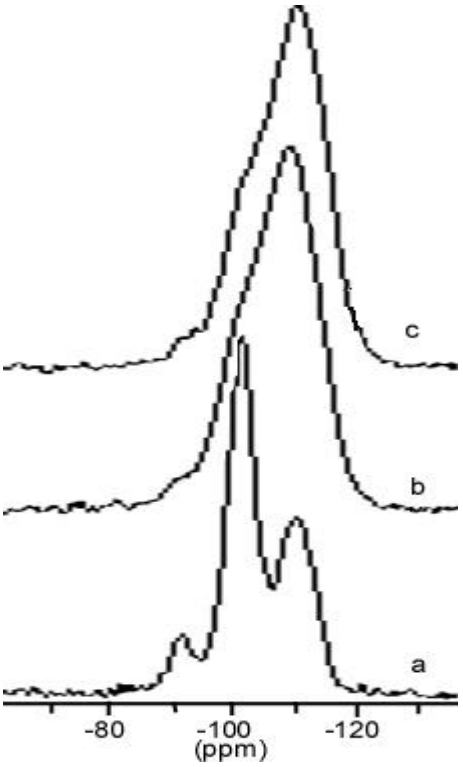


Figure 25. $^{29}$Si MAS NMR spectra of silica foams at various stages of the synthesis. Spectra "a","b" and "c" belong to samples samples *Si-FO-AS-0*, *Si-FO-C-0* and *Si-FO-HTC-0*, respectively.

| | | δ (ppm) | ΔH (Hz) | I (%) |
|---|---|---|---|---|
| Si-FO-AS-0 | $Q_2$ | -91.4 | 425 | **8.3** |
| | $Q_3$ | -101.3 | 425 | **57.2** |
| | $Q_4$ | -110.3 | 555 | **34.5** |
| Si-FO-C-0 | $Q_2$ | -91.0 | 500 | **2.9** |
| | $Q_3$ | -100.8 | 830 | **36.4** |
| | $Q_4$ | -110.1 | 775 | **60.7** |
| Si-FO-HTC-0 | $Q_2$ | -91.4 | 500 | **3.2** |
| | $Q_3$ | -100.8 | 670 | **24.1** |
| | $Q_4$ | -110.1 | 830 | **72.7** |

Table 10. Results of the decomposition of $^{29}$Si MAS NMR spectra of silica foams

The figures in the last column of the table are pretty straightforward to explain. Silicon atoms having 3 other silicon (and one –OH, presumably) neighbours make up the skeleton of the as-synthesised material. This finding conforms well to the general mechanism of the sol-gel process described in Section 2. Conventional calcination changes the $Q_4/Q_3$ ratio from 0.6 to 1.7, which can be interpreted by the heat-induced formation of Si-O-Si bridges from Si-OH HO-Si groups. If the as-synthesised material is treated hydrothermally prior to calcination, the final foam will have a $Q_4/Q_3$ ratio of 3, significantly higher then the previous value. In other words: there are more Si atoms in the foam walls that are covalently linked to other Si atoms in the three dimensional framework of the foam walls. This new finding is an experimental evidence for the necessity of the hydrothermal treatment.

*4.2.2.2. Chemical properties*

Because of their absolute novelty, silica foams do not have any direct catalytic applications yet. They could certainly be used as porous supports to construct catalysts similar to those synthesised by the post-calcination conventional impregnation of silica nanotubes (Section 3.1.2.1). However, foams can be made much easier and with larger yields than nanotubes, and therefore, we conceived it might be feasible to prepare acidic silica foams in a one-step sol-gel synthesis [119], much like the composites described in Section 3.1.1.2. To our best knowledge, such materials were not mentioned in the literature before.

We have developed two sol-gel based routes to incorporate acidic function into silica foams. This was trial-and-error experimentation at its best, since the quality of the final foam was found to be a sensitive non-linear function of the exact timing and composition of the steps of the synthesis. In the case of PW12 containing foams the most crucial factor was the water content of the precursor sol. The presence of water is essential for the surfactant to function, but above a certain concentration limit not all of the added water is built into the foam walls, resulting in a foam monolith floating over clear water. While this is not a problem when preparing purely siliceous foams, it completely ruins would-be heteropoly acid — silica composites because an unknown amount of PW12 remains dissolved in the aqueous phase instead of entering the foam. In the case of alumina-silica composite foams the problems were caused by the different moisture sensitivities of TEOS and AiPR3. Add AiPR3 to the foam too soon and it will hydrolyse by itself. Add it too late, and the hydrolysis of TEOS will have proceeded so far that aluminum can not enter the three dimensional network. In either case we end up with pieces of $Al_2O_3$ scattered in a $SiO_2$ foam instead of an acidic alumina-silica composite. Due to the extremely empirical nature of the process, details of the optimisations

are not described here. It is enough to note that both PW12 and alumina containing foams mentioned below were synthesised bearing the mentioned pitfalls in mind.

Experimental evidence about the presence of the acidic function in the foams was obtained by spectroscopic techniques. The evolution of the bands at 210, 265 and 315 nm in the diffuse-reflectance UV-VIS spectra of the PW12-$SiO_2$ composite foams presented in Figure 26. shows that phosphotungstic acid has entered the materials in the quantities intended. Comparing the KBr IR spectra of the silica-alumina foams (Figure 27.) we can realise that bands correlated with framework torsion vibrations at 1105 and 822 $cm^{-1}$ in pure silica have shifted to 1074 and 800 $cm^{-1}$ in the composite. This phenomenon is caused by the incorporation of aluminum into the silica framework, and therefore, it can be considered as proof of the successful sol-gel synthesis.

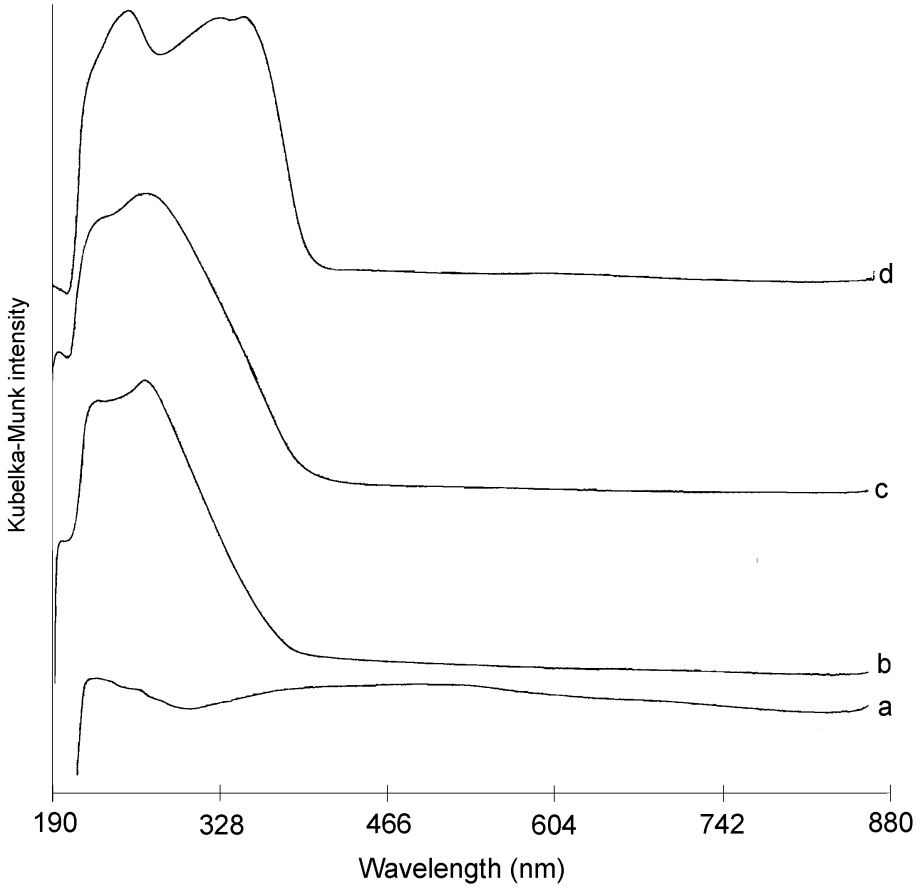


Figure 26. Diffuse reflectance UV-VIS spectra of samples *Si-FO-C-0* (a), *Si-FO-C-5* (b), *Si-FO-C-20* (c) and pure phosphotungstic acid (d)

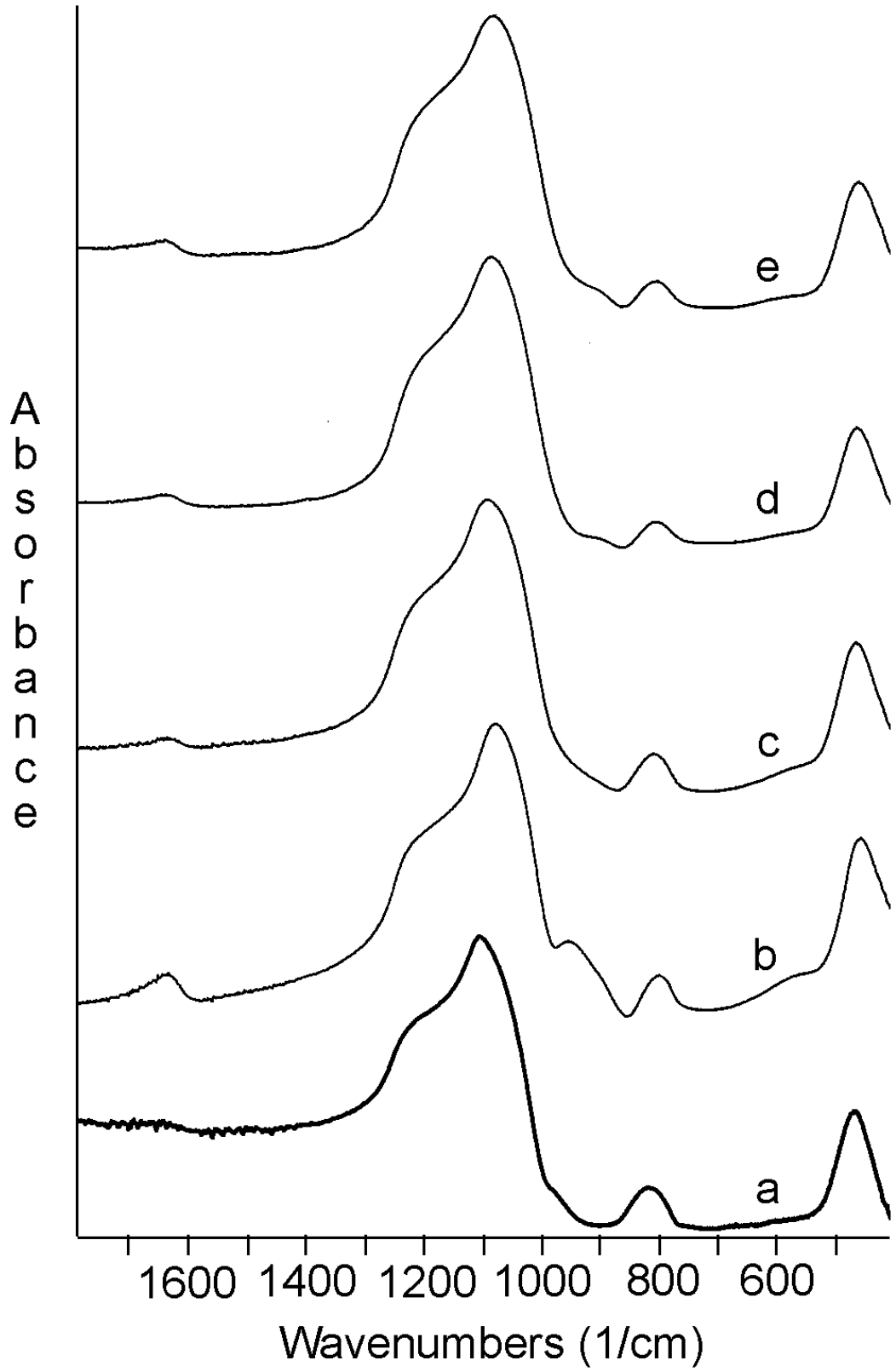


Figure 27. Framework torsion region of the IR spectrum of samples *Si-FO-C-0* (a), *Al,Si-FO-C-20* (b), *Al,Si-FO-HTC-20* (c), *Al,Si-FO-C-5* (d) and *Al,Si-FO-HTC-5* (e)

Acidity of the samples was measured using the well-established technique of pyridine adsorption. Optical densities of the bands corresponding to pyridine adsorbed on Broensted and Lewis acidic centres are given for each sample in the second and third columns of Table 11. The fourth column (denoted B/L) in the table is the ratio of the densities of the Broensted and Lewis bands, while the fifth and sixth columns give the ratios of acid sites before and after hydrothermal treatment. It should be noted that these B/L ratio differ from the real ratio of Broensted and Lewis acidic centres because the extinction coefficients of the surface complexes giving raise to the bands at 1450 and the 1540 $cm^{-1}$ are not necessarily equal. However, it is a useful tool when comparing the Broensted/Lewis ratio of various samples.

| Sample | Broensted (A/mg) | Lewis (A/mg) | B/L | $B_C/B_{HTC}$* | $L_C/L_{HTC}$* |
|---|---|---|---|---|---|
| *Si-FO-C-0* | 0 | 0.004 | 0 | | |
| *Si-FO-HTC-0* | 0 | 0.003 | 0 | n.a. | 1.333 |
| *PW12,Si-FO-C-5* | 0.091 | 0.085 | 1.07 | | |
| *PW12,Si-FO-HTC-5* | 0.083 | 0.079 | 1.05 | 1.096 | 1.076 |
| *PW12,Si-FO-C-20* | 0.147 | 0.129 | 1.139 | | |
| *PW12,Si-FO-HTC-20* | 0.121 | 0.111 | 1.095 | 1.215 | 1.162 |
| *Al,Si-FO-C-20* | 0.129 | 0.084 | 1.532 | | |
| *Al,Si-FO-HTC-20* | 0.079 | 0.081 | 0.973 | 1.636 | 1.039 |
| *Al,Si-FO-C-5* | 0.135 | 0.116 | 1.162 | | |
| *Al,Si-FO-HTC-5* | 0.065 | 0.083 | 0.787 | 2.065 | 1.400 |

* Ratios calculated from the original (C) and hydrothermally treated (HTC) samples are reported in the "HTC" line of each material.

Table 11. A summary of the acidic properties of solid acid foams.

It is evident from the acidity data that each but the pure silica sample possesses both Broensted and Lewis acidity. The amount of such centres is correlated with the amount of active component (PW12 or aluminum) incorporated into the matrix, thus providing us a tool for the tuning of the acidity of the foams. To gain insight into the possibilities of fine-tuning the acidity, the following observations can be made in the last three columns of Table 11. Heteropoly acid-silica composite foams show balanced behaviour: (i) their Broensted to Lewis ratio is closer to unity and changes less than that of the Al series, (ii) increasing the amount of PW12 incorporated increases the number of acid sites proportionally and (iii) calcination does not have a tremendous impact on the number of acid sites available for pyridine. Silica-alumina systems on the other hand seem to be more sensitive to synthesis

conditions: (i) a 4-fold increase in the number of potential acid centres can not even double the optical density of the pyridine adsorption bands, (ii) hydrothermal treatment is able to change the ratio of Broensted and Lewis sites to the opposite and (iii) in most cases, hydrothermal treatment drastically reduces the number of available acid sites of any kind. We believe that these major changes might originate from the partial dealumination of the foam framework and — especially in *Al,Si-FO-C-5* — from the formation of a separate, extra framework, alumina phase.

Finally, we can conclude that a very important step in the functionalisation of novel mesoporous silica foams has been made [119] by inventing two different routes to incorporate Broensted and Lewis acid centres into the foam walls. Acidity of the foams can be tailored by modifying the composition and the pre-treatment method applied. The hydrothermally treated PW12—$SiO_2$ composite seems to be the best choice for general acidic heterogeneous catalytic applications.

### *4.3 General considerations concerning fractal dimension*

Fractal materials have scale-invariant morphological features by definition and can be classified as mass fractals, pore fractals and surface fractals. The latter two are of considerable interest from the point of view of heterogeneous catalysis, since transport efficiency and catalytic activity may both be related to pore and surface self-similarity. While it is generally agreed that pore fractals are seldom found among common porous silica systems, the existence of surface fractality in the same materials is still heavily debated. We have performed a comprehensive study [118] involving all pore systems (*-ME-*, *-NT-* and *–FO-*) mentioned in this thesis in order to find out (i) if our sol-gel derived materials can be considered to be surface fractals or not, and (ii) if the everyday wear-and-tear is able to modify the self-similar behaviour of a potential silica catalyst.

The surface fractal dimension calculated by two methods and at three different mechanical pressure levels is given for *Si-ME-C-0*, *Si-NT-C-0*, *Si-FO-C-0* and *Si-FO-HTC-0* in Tables 12.…15., respectively. It is easy to notice that the general fractal behaviour is independent of the details of the calculation, and that D is approximately 2 for nanotubes, 3 for foams and ca. 2.5 for amorphous silica. The latter material did not exhibit any change in surface fractal dimension up to 9 ton/cm$^2$, but in the case of nanotubes and foams a small shift towards D=2.5 could be observed. It should also be noted that the foam structure collapsed completely even at pressures below 1 ton/cm$^2$.

| Applied pressure | Wang method | | FHH equation | |
|---|---|---|---|---|
| (ton/cm$^2$) | Adsorption | Desorption | Adsorption | Desorption |
| 0 | 2.38 ± 0.07 | 2.61 ± 0.10 | 2.48 ± 0.12 | 2.53 ± 0.08 |
| 3 | 2.41 ± 0.03 | 2.67 ± 0.08 | 2.47 ± 0.04 | 2.52 ± 0.05 |
| 9 | 2.58 ± 0.05 | 2.64 ± 0.06 | 2.34 ± 0.07 | 2.39 ± 0.11 |

Table 12. Calculated surface fractal dimension of mesoporous silica

| Applied pressure | Wang method | | FHH equation | |
|---|---|---|---|---|
| (ton/cm$^2$) | Adsorption | Desorption | Adsorption | Desorption |
| 0 | 2.02 ± 0.11 | 2.08 ± 0.14 | 2.15 ± 0.04 | 2.07 ± 0.02 |
| 3 | 2.06 ± 0.10 | 2.10 ± 0.07 | 2.03 ± 0.06 | 2.11 ± 0.12 |
| 9 | 2.16 ± 0.05 | 2.23 ± 0.09 | 2.14 ± 0.05 | 2.16 ± 0.08 |

Table 13. Calculated surface fractal dimension of silica nanotubes

| Applied pressure | Wang method | | FHH equation | |
|---|---|---|---|---|
| (ton/cm$^2$) | Adsorption | Desorption | Adsorption | Desorption |
| 0 | 2.89 ± 0.11 | 2.97 ± 0.15 | 2.92 ± 0.17 | 2.99 ± 0.10 |
| 3 | 2.86 ± 0.17 | 2.98 ± 0.18 | 2.93 ± 0.19 | 2.86 ± 0.14 |
| 9 | 2.79 ± 0.15 | 2.81 ± 0.15 | 2.84 ± 0.12 | 2.85 ± 0.16 |

Table 14. Calculated surface fractal dimension of calcined silica foam

| Applied pressure | Wang method | | FHH equation | |
|---|---|---|---|---|
| (ton/cm$^2$) | Adsorption | Desorption | Adsorption | Desorption |
| 0 | 2.93 ± 0.15 | 2.91 ± 0.09 | 2.98 ± 0.12 | 2.93 ± 0.16 |
| 3 | 2.90 ± 0.08 | 2.89 ± 0.07 | 2.88 ± 0.03 | 2.88 ± 0.11 |
| 9 | 2.85 ± 0.06 | 2.83 ± 0.13 | 2.77 ± 0.10 | 2.82 ± 0.14 |

Table 15. Calculated surface fractal dimension of hydrothermally treated and calcined silica foam

The surface fractal dimension (D) of a solid is basically an indicator of the presence (or absence) of scale invariant surface features. The case of D=2 corresponds to adsorption on a smooth, flat surface. D=3 indicates space filling with the adsorbate, while cases of 2<D<3 conform to adsorption on a fractal surface. The surface fractal dimension of freshly calcined

silica nanotubes was found to be close to 2 independent of the method of calculation. No scale invariant features are present: the word "surface" can only be interpreted on one scale, and that is the μm dimensional scale of the tubes. (The surface area — and thus, the contribution to the surface fractal dimension measurable by adsorption techniques — of the aggregated silica phase is negligible [Ref] compared to that of the nanotubes.) This finding is consistent with the formation mechanism suggested in Section 4.2.1: the nanotubes are made of silica planes of roughly the same size, which is easiest to explain by assuming that a large number of planes are synthesised on the very same template sheet. While moderate mechanical pressure has no effect on the fractality of the nanotubes, applying a large pressure of 9 ton/cm$^2$ resulted in a minor increase in D. The increase is probably caused by physical fracture effects. The walls of the nanotubes break, and the revealed jagged surfaces have adsorption properties different from the original smooth tube walls. Since the majority of these planes remains intact, the overall observable result is the ~0.1 increase in the surface fractal dimension.

The D~3 values obtained for the calcined silica foam indicate that this material also lacks fractal surface features, but because of a completely different reason. Here the adsorption process quickly changed to space filling, and therefore the formalism of Equations 9. and 10. can no longer provide information about surface properites. Our foam proved to be extremely vulnerable to mechanical pressure, as even at 1 ton/cm$^2$ it has lost its hollow structure and was pressed into a white powder. This denser material no longer exhibited space filling adsorption capabilities, instead, it started behaving as a fractal surface of D~2.8. In our opinion, this transition originates from the appearance of a new type of surface, which is made up of the tightly compressed shells of the foam pores.

The ordinary amorphous mesoporous silica sample was found to be a surface fractal in the sub-micrometer dimension by all calculation methods and at all pressures applied. Once again, the synthesis conditions, namely the possibility for the secondary aggregation of the sol particles seems to be responsible for this phenomenon. Effects of the mechanical pressure are hardly identifiable: the material was lacking morphology right after calcination, therefore even the 9 ton/cm$^2$ pressure could only transform it from one amorphous, rugged state into another. From the practical point of view, such tolerance of mechanical pressure compensates for the lack of a refined pore structure and renders amorphous mesoporous silica a more appealing candidate for disk-shaped reactors and filters than any other silica species studied here.

## 5. SUMMARY

The primary goal of this PhD work was to perform basic research to explore the possibilities of a rapidly developing, modern and popular synthesis technique, the sol-gel method. Since this technique was not previously employed by our group, it was my objective to implement as many small, independent projects serving as potential starting points for long-term research plans as I could.

The studies were focused on functionalised silica matrices possessing meso- or macroporous channel system, and their possible applications in heterogeneous catalysis. Besides ordinary amorphous materials, we were able to build acidic centres into novel silica shapes: nanotubes and foams. We have utilised various techniques ($N_2$ adsorption, TG, SEM, TEM, $^{29}Si$ MAS NMR, $NH_3$ TPD, AAS, XRD, IR, UV-VIS) for sample characterisation, applied semi-empirical molecular modelling and advanced data processing techniques (fractal dimension analysis, spectral decomposition), and tested most of the prepared solid acids in the chosen reaction of 1-butene isomerisation. Certain catalysts were found to be active in two research fields currently investigated at our Department: catalytic carbon nanotube synthesis and Diels-Alder type cycloadditions.

The major results of this PhD research are the following:

1. Concerning sol-gel derived structures in general:

- We have suggested a possible mechanism for the formation of angular silica nanotubes.
- We have proven the advantages of hydrothermal treatment in silica foam synthesis.
- We have performed a comprehensive study on the surface fractal properties of sol-gel derived silica species, and published surface fractal dimension data of silica nanotubes and silica foams for the first time in literature.

2. Concerning catalyst design:

- We were able to build acid centres into silica foams, thus synthesising a novel composite material not mentioned in the literature before.
- We have found that the effective acidity curve of $H_3PW_{12}O_{40}$ — $SiO_2$ composites passes through a maximum as a function of acid contents.
- We have proven that sol-gel derived $H_3PW_{12}O_{40}$ — $SiO_2$ composite catalysts are superior to their conventionally impregnated counterparts with respect to stability in polar solvents.

3. Concerning real-life applications:

- A sol-gel Co,Fe-$SiO_2$ catalyst was found to generate multiwall carbon nanotubes in moderate quantities, yet with splendid quality.

- Sol-gel $H_3PW_{12}O_{40}$ — $SiO_2$ composites were found to be effective catalysts of the Diels-Alder type cycloaddition reaction between 1,3-cyclohexadiene and 2-propenal.

If one outcome had to be named as the single most important result of this research, in my opinion it would be the synthesis of acidic silica foams. Their excellent formability and unique, open pore system make these materials promising candidates for novel, high liquid throughput disk-shaped and membrane reactors. We are currently planning an optimisation process similar to that performed on the ordinary mesoporous $H_3PW_{12}O_{40}$ — $SiO_2$ composites to find the optimal acid-to-silica ratio of the foams. Once the best catalyst is found, we shall focus our attention on utilising the experience obtained about Diels-Alder reactions, and move on to perform cycloadditions in fixed-bed continuous flow reactors. Our long-term goals also include building optical modifiers (e.g. carbohydrates) into the acidic foams and thus, to modify the stereoselectivity of the chosen Diels-Alder reactions.

Other research themes waiting to be exploited after being briefly touched here are high quality carbon nanotube synthesis on sol-gel derived catalysts, and theoretical studies on the relationship between the surface fractal dimension and the catalytic properties of sol-gel materials.

## 6. ACKNOWLEDGEMENT

I am indebted to a great many people for helping and supporting my PhD research. First of all I must thank my wife and my parents for their assistance during these last 21 years spent learning. Concerning science: I thank my supervisor, Dr. Imre Kiricsi for guiding my career, Dr. István Pálinkó for inspiring discussions, Dr. Zoltán Kónya for helping me whenever it was necessary and all of the staff of the Department of Applied and Environmental Chemistry of the University of Szeged, Hungary.

Long-distance thank-you's go to Dr. Fujio Mizukami, Dr. Makoto Toba, Dr. Shu-Ichi Niwa and Dr. Yoshimichi Kiyozumi of NIMC, Tsukuba, Japan; to Dr. János B.Nagy and Patrick Lentz of FUNDP, Namur, Belgium and to Dr. Wladimir Reschetilowski and Damian Mönter of TU Dresden, Dresden, Germany.

This PhD research was financed through the regular scholarship system of the Hungarian Ministry of Education. Additional financial support was provided by the following projects: MKM FKFP 0486/1999, DAAD-MÖB 30/1999 and occasional travel grants provided by OMFB and the Hungarian Soros Foundation.

## 7. REFERENCES


1 Weissermel, K.; Arpe, H-J., "*Industrial Organic Chemistry*" (in Hungarian), Tankönyvkiadó, Budapest, 1993.

2 Beck, J.S.; Vartuli, J.C.; Roth, W.J.; Leonowicz, M.E.; Kresge, C.T.; Schmitt, K.D.; Chu, C.T-W.; Olson, D.H.; Sheppard, E.W.; McCullen, S.B.; Higgins, J.B.; Schlenker, J.L., *J. Am. Chem. Soc.* 1992, **114**, 10834.

3 Ebelmen, M., *Ann. Chimie Phys.*, 1846, **16**, 129.

4 Graham, T., *J. Chem. Soc*., 1846, **17**, 318.

5 Liesegang, R.E., *Photogr. Archiv*., 1896, 221.

6 Roy, D.M.; Roy, R., *Am. Mineral*., 1954, **39**, 957.

7 Brinker, C.J.; Scherer, G.W., '*Sol-gel Science: The Physics and Chemistry of Sol-Gel Processing*", Academic Press: New York, 1990.

8 Levy, D., *Chem. Mater*., 1997, **9**, 2666-2670.

9 Lee, G.R.; Crayston, J.A., *Adv. Mater.*, 1993, **5**, 434-442.

10 Bhatia, R.B.; Brinker, C.J.; Gupta, A.K.; Singh, A.K., *Chem. Mater.*, 2000, **12**, 2434-2441.

11 Jain, T.K.; Roy, I.; De, T.K.; Maitra, A., *J. Am. Chem. Soc.*, 1998, **120**, 11092-11095

12 Ward, D.E.; Ko, E.I., *Ind. Eng. Chem. Res.*, 1995, **34**, 421-433

13 Szántó, F.; "*The Basics of Colloid Chemistry*" (in Hungarian), Gondolat, Budapest, 1987.

14 Swain, C.G.; Estene, R.M., Jr.; Jones, R.H., *J. Am. Chem. Soc*., 1949, **71**, 965.

15 Keefer, K.D., In "*Better Ceramics Through Chemistry*"; Brinker, C.J.; Clark, D.E.; Ulrich, D.R., Eds.; Elsevier, New York, 1984.

16 Zerda, T.W.; Hoang, G., *J. Non-Cryst. Sol*., 1989, **109**, 9.

17 Flory, P.J., "*Principles of Polymer Chemistry*", Cornell University Press: Ithaca, NY, 1953.

18 Zallen, R., "*The Physics of Amorphous Solids*", Wiley: New York, 1983.

19 Mandelbrot, B.B., "*The Fractal Geometry of Nature*", Freeman and Co., New York, 1982.

20 Novotny, E., "*Introduction to Stellar Atmospheres and Interiors*", Oxford, University Press, New York, 1973.

21 Keefer, K.D., In "*Science of Ceramic Chemical Processing*"; Hench, L.L., Ulrich, R.D. Eds.; Wiley, New York, 1986.

22 Jones, S.D.; Pritchard, T.N.; Lander, D.F., *Micropor. Mater.*, 1995, **3**, 419-431.

23 Toba, M.; Mizukami, F.; Niwa, S-I.; Sano, T.; Maeda, K.; Annila, A.; Komppa, V., *J. Mol. Catal*., 1994, **91**, 277-289.

24 Hench, L.L.; West, J.K., *Chem. Rev.*, 1990, **90**, 33.

25 Smith, D.M.; Desphande, R.; Brinker, C., In "*Better ceramics through chemistry*" Brinker, C.J.; Clark, D.E.; Ulrich, D.R., Eds.; Elsevier, New York, 1984.

26 Brinker, C.J.; Scherer, G.W.; Roth, E.P., *J. Non-Cryst. Sol*., 1985, **72**, 345.

27 Curran, M.D.; Pooré, D.D.; Stiegman, A.E., *Chem. Mater.*, 1998, **10**, 3156-3166

28 Mizukami, F.; Kiyozumi, Y.; Sano, T.; Niwa, S-I.; Toba, M.; Shin, S, *J. Sol-Gel Sci&Tech*., 1998, **13**, 1027-1031.

29 Toba, M.; Niwa, S-I.; Shimada, H.; Mizukami, F., in "*Heterogeneous Catalysis and Fine Chemicals IV*",

Blaser, H.U.; Baiker, A.; Prins, R., (Eds), Elsevier, Amsterdam, 1997.

30 Ennas, G.; Musinu, A.; Piccaluga, G.; Zedda, D.; Gatteschi, D.; Sangregorio, C.; Stanger, J.L.; Concas, G.; Spano, G., *Chem. Mater*. 1998, **10**, 495-502.

31 Navío, J.A.; Macías, M.; Colón, G.; Sánchez-Soto, P.J.; Augugliaro, V.; Palmisano, L., *Appl. Surf. Sci*, 1994, **81**, 325-329.

32 Chai, M.; Machida, M.; Eguchi, K.; Arai, H., *J. Membr. Sci*., 1994, **96**, 205-212.

33 De, G.; Mattei, G.; Mazzoldi, P.; Sada, C.; Battaglin, G.; Quaranta, A., *Chem. Mater*., 2000, **12**, 2157-2160

34 Rogovin, M.; Neumann, R., *J. Mol. Catal. A*, 1999, **138**, 315-318.

35 Kröcher, O.; Köppel, R.A.; Fröba, M.; Baiker, A., *J. Catal.*, 1998, **178**, 284-298.

36 López, T.; Gómez, R.; Novaro, O.; Ramírez-Solís, A.; Sánchez-Mora, E.; Castillo, S.; Poulain, E.; Martínez-Magadán, J.M., *J. Catal*., 1993, **141**, 114-123.

37 Niwa, S-I.; Mizukami, F.; Isoyama, S.; Tsuchiya, T.; Shimizu, K.; Imai, S.; Imamura, J., *J. Chem. Tech. Biotech*., 1986, **36**, 236-246.

38 Kluson, P.; Had, J.; Belohlav, Z.; Cerveny, L., *Appl. Catal. A*, 1997, **149**, 331-339.

39 Mizukami, F.; Izutsu, H.; Osaka, T., *Adv. Mater*., 1994, **6**, 854-855.

40 Mizukami, F.; Akiyama, Y.; Izutsu, H., *Supramol. Sci*., 1998, **5**, 433-437.

41 Reuter, H.; Brandherm, M-T., *Angew. Chem. Int. Ed. Engl*., 1995, **34**, 1578-1579.

42 Lange, C.; Storck, S.; Tesche, B.; Maier, W.F., *J. Catal*., 1998, **175**, 280-293.

43 Sheng, G.; Chu, L.; Zeltner, W.A.; Anderson, M.A., *J. Non-Cryst. Sol*., 1992, **147/148**, 548-553.

44 Sano, T.; Yanagishita, H.; Kiyozumi, Y.; Mizukami, F.; Haraya, K., *J. Membr. Sci*., 1994, **95**, 221-228.

45 Julbe, A.; Guizard, C.; Larbot, A.; Cot, L.; Giroir-Fendler, A., *J. Membr. Sci*., 1993, **77**, 137-153.

46 Yang, H.; Coombs, N.; Ozin, G.A., *Nature*, 1997, **386**, 692-695.

47 Huo, Q.; Margolese, D.I.; Ciesia, U.; Feng, P.; Gier, T.E.; Sieger, P.; Leon, R.; Petroff, P.M.; Schüth, F.; Stucky, G.D., *Nature*, 1994, **368**, 317-321.

48 Kobayashi, S.; Hanabusa; K.; Hamasaki, N.; Kimura, M.; Shirai, H., *Chem. Mater*., 2000, **12**, 1523-1525.

49 Ichinose, I.; Senzu, H.; Kunitake, T., *Chem. Mater*., 1997, **9**, 1296-1298.

50 Khimyak, Y.Z.; Klinowski, J.; *J. Chem. Soc. Farad. Trans.*, 1998, **94**, 2241-2247.

51 Nakamura, H.; Matsui, Y., *J. Am. Chem. Soc.*, 1995, **117**, 2651.

52 Bagshaw, S. A., *Chem. Comm.* 1999. 767-768

53 Bagshaw, S.A.; Kemmitt, T.; Milestone, N.B., *Mesopor. Macropor. Mat*., 1998, **22**, 419-433.

54 Pfeifer, P.; Avnir, D.; Farin, D., *J. Chem. Phys*., 1983, **79**, 3666.

55 Pfeifer, P.; Avnir, D., *Nature*, 1984, **208**, 261.

56 Ehrburger-Dolle, F.; Holz, M.; Lahaye, J., *Pure&Appl. Chem.*, 1993, **65**, 2223.

57 Rigby, S.P.; Gladden, L F., *J. Catal*., 1998, **180**, 44.

58 Avnir D., Ed. „*The Fractal Approach to Heterogeneous Chemistry*"; Wiley: New York, 1992.

59 Conner, W.C.; Bennett, C.O., *J. Chem. Soc. Farad. Trans.*, 1993, **89**, 4109.

60 Giona, M.; Giustiniani, M., *J. Phys. Chem.*, 1996, **100**, 16690.

61 Ehrburger-Dolle, F., *Langmuir*, 1997, **13**, 1189.

62 Fadeev, A.Y.; Borisova, O.R.;. Lisichkin, G.V, *J. Coll. Int. Sci*., 1996, **183**, 1.

63 Wang, F.; Li, S., *Ind. Eng. Chem. Res.*, 1997, **36**, 1598.

64 Sermon, P.A.; Wang, Y.; Vong, M.S.W., *J. Coll. Int. Sci*., 1994, **168**, 327.

65 Drake, J.M.; Levitz, P.; Klafter, J., *New J. Chem.*, 1990, **14**, 77.

66 Gottsleben, F.; Hesse, D., *Hung. J. Ind. Chem.*, 1991, **19**, 283.

67 Thomas, J.M.; Thomas, W.J., "*Principles and Practice of Heterogeneous Catalysis*", VCH: Berlin, 1997.

68 Oberlin, A.; Endo, M.; Koyama, T., *J. Cryst. Growth*, 1976, **32**, 335-349.

69 Iijima, S., *Nature (London)*, 1991, **354**, 56.

70 Iijima, S.; Ichihashi, T., *Nature (London)*, 1993, **363**, 603.

71 Ando, Y.; Iijima, S., *Jpn. J. Appl. Phys*., 1993, **32**, 107.

72 Guo, T.; Nikolaev, P; Thess, A.; Colbert, D.T.; Smalley, R.E., *Chem. Phys. Lett.*, 1995, **243**, 49.

73 Ivanov, V.; B.Nagy, J.; Lambin, P.; Lucas, A.; Zhang, X.B.; Zhang, X.F.; Bernaerts, D.; Van Tendeloo, G.; Amelinckx, S.; Van Landuyt, J., *Chem. Phys. Lett.*, 1994, **223**, 329

74 Ivanov, V.; Fonseca, A.; B.Nagy, J.; Lucas, A.; Lambin, P.; Bernaerts, D.; Zhang, X.B., *Carbon*, 1995, **33**, 1727.

75 Li, W.Z.; Xie, S.S.; Qian, L.X.; Chang, B.H.; Zou, B.S.; Zhou, B.Y.; Zhao, R.A.; Wang, G.; *Science*, 1998, **274**, 1701.

76 Mukhopadhyay, K.; Koshio, A.; Sugai, T.; Tanaka, N.; Shinohara, H.; Kónya, Z.; B.Nagy, J., *Chem. Phys. Lett*., 1999, **303**, 117.

77 March, J., "*Advanced Organic Chemistry*", 4th Edition, Wiley&Sons, New York, 1992.

78 Oppolzer, W., *Angew. Chem.*, 1984, **96**, 840-854.

79 Ishihara, K.; Kurihara, H.; Matsumoto, M.; Yamamoto, H., *J. Am. Chem. Soc*., 1998, **120**, 6920-6930.

80 Narasaka, K.; Tanaka, H.; Kanai, F., *Bull. Chem. Soc. Jpn*., 1991, **64**, 387-391.

81 Endo, K.; Koike, T.; Sawaki, T.; Hayashida, O.; Masuda, H.; Aoyama, Y., *J. Am. Chem. Soc.*, 1997, **119**, 4117-4122.

82 Fraile, J.M.; Garcia, J.I.; Gracia, D.; Mayoral, J.A.; Tarnai, T.; Figueras, F., *J. Mol. Catal. A*, 1997, **121**, 97-102.

83 Eklund, L.; Axelsson, A-K.; Nordahl, A.; Carlson, R., *Acta Chim. Scand*., 1993, **47**, 581.

84 Bautista, F.M.; Campelo, J.M.; Garcia, A.; Luna, D.; Marinas, J.M.; García, J.I.; Mayoral, J.A.; Pires, E., *Catal. Lett*., 1996, **36**, 215-221.

85 Meuzelaar, G.J.; Maat, L.; Sheldon, R.A., *Catal. Lett*., 1998, **56**, 49.

86 Klier, K., *Cat. Rev*., 1967, **1**, 207.

87 Brunauer, S.; Emmet, P.H.; Teller, E., *J. Am. Chem. Soc.*, 1938, **60**, 309.

88 Wheeler, A., „*Catalysis*", Vol. 2, Reinhold, New York, 1952.

89 Barrett, E.P.; Joyner, L.G.; Halenda, P.P., *J. Am. Chem. Soc.*, 1951, **73**, 373.

90 Dubinin, M.M., *Quart. Rev. Chem. Soc.*, 1955, **9**, 101.

91 Gregg, S.J.; Sing, K.S.W., "*Adsorption, Surface Area and Porosity*", Academic Press: London, 1982. (2nd Edition)

92 Pfeifer, P.; Cole, M.W., *New J. Chem*., 1990, **14**, 221.

93 Neimark, A., *Physica A*, 1992, **191**, 258.

94 Kukovecz, A.; Kónya, Z.; Mönter, D.; Reschetilowski, W.; Kiricsi, I., *J. Mol. Struct.*, 2001, **563/564**,

403-407.

95 Prakesh, A.M.; Sung-Suh, H.M.; Kevan, L., *J. Phys. Chem. B*, 1998, **102**, 857.

96 Ballhausen, C.J., "*Introduction to Ligand Field Theory*", McGraw-Hill, New York, 1962.

97 Kukovecz, A.; Kollár, T.; Kónya, Z.; Kiricsi, I., *J. Mol. Struct*., 1999, **482-483**, 39-42.

98 Kukovecz, A.; Fudala, A.; Kiricsi, I., in (i) 41st Annual Meeting of Hungarian Spectroscopists, Budapest, 1998, Book of Abstracts, (ii) XXV. Annual Lecture Series of the Association of Hungarian Chemists, Szeged, 1998, Book of Abstracts. (both in Hungarian)

99 FKFP 0102/2001, 4.800 ezer Ft, *"Heterogén fotokatalitikus reakciók alkalmazása környezeti szennyezõk fotokémiai eltávolítására és a napsugárzás energiájának tárolására"*

100 Kukovecz, A.; Kónya, Z.; Nagaraju, N.; Willems, I.; Tamási, A.; B.Nagy, J.; Kiricsi, I, *Phys. Chem. Chem. Phys*., 2000, **2**, 3071-3076

101 Willems, I.; Kónya, Z.; Colomer, J-F.; Van Tendeloo, G.; Nagaraju, N.; Fonseca, A.; B.Nagy, J, *Chem. Phys. Lett*., 2000, **317**, 71.

102 Schwegler, M.A.; Vinke, P.; van der Eijk, M.; van Bekkum, H., *Appl. Catal. A,* 1992, **80**, 41-57.

103 Izumi, Y.; Ogawa, M.; Urabe, K., *Appl. Catal. A*, 1995, **132**, 127.

104 Boschen, I.; Buss, B.; Krebs, B., *Acta Cryst. B*, 1974, **30**, 48.

105 Brown, G.M.; Noe-Spirlet, M-R.; Busing, W.R.; Levy, H.A., *Acta Cryst. B*, 1977, **33**, 1078.

106 West, S.F.; Audrieth, L.F., *J. Phys. Chem.*, 1955, **59**, 1069.

107 Hayashi, H.; Moffat, J.B., *J. Catal*., 1982, **77**, 473.

108 Martínez, J.R.; Ruiz, F.; Vorobiev, Y.V.; Pérez-Robles, F.; González-Hernandez, J., *J. Chem. Phys*., 1998, **109**, 7511-7514

109 Borwn, D.H., *Spectrochimica Acta*, 1963, **19**, 585.

110 Rocchiccioli-Deltcheff, C.; Thouvenot, R.; Franck, R., *Spectrochimica Acta A*, 1976, **32**, 587.

111 Rocchiccioli-Deltcheff, C.; Fournier, M.; Franck, R., *Inorg. Chem.*, 1983, **22**, 207.

112 Miller, J.M.; Lakshmi, L.J., *J. Phys. Chem. B*, 1998, **102**, 6465-6470

113 Kapustyn, G.I.; Brueva, T.R.; Kljacko, A.L.; Timofeyeva, M.N.; Kulikov, S.M.; Kozevnikov, I.V., *Kinet. Katal*. 1980, **31**, 1017.

114 Kukovecz, A.; Kónya, Z., Kiricsi, I., *J. Mol. Struct.*, 2001, **565/566**, 121-124.

115 Varga, M.; Török, B.; Molnár, A., *J. Therm. Anal*., 1998, **53**, 207.

116 Stober, W.; Fink, A.; Bohn, E., *J. Coll. Int. Sci*., 1968, **26**, 62.

117 Kiricsi, I.; Kukovecz, A.; Fudala, A.; Kónya, Z.; Willems, I.; B.Nagy, J., *Stud. Surf. Sci. Catal*., 2000, **130**, 1115-1120

118 Kukovecz, A.; Kónya, Z.; Pálinkó, I.; Mönter, D.; Reschetilowski, W.; Kiricsi, I., *Chem. Mater*. 2001, **13**, 345-349.

119 Kukovecz, A.; Kónya, Z., Kiricsi, I., *J. Mol. Struct.* 2001, **563/564**, 409-412.

# 8. APPENDIX

In this Appendix I shall present a comprehensive table containing data about each and every sample mentioned in this thesis.

| Label | Matrix | Modifier | Properties | Mentioned in Section |
|---|---|---|---|---|
| *Co,Fe,Si,Ti-ME-AS-2.5* | 50 % $SiO_2$<br>50 % $TiO_2$ | 2.5 % Co<br>2.5 % Fe | Amorphous, mesoporous.<br>As synthesised. | 4.1.1.1 |
| *Co,Fe,Ti-ME-AS-2.5* | $TiO_2$ | 2.5 % Co<br>2.5 % Fe | Amorphous, mesoporous.<br>As synthesised. | 4.1.1.1 |
| *Co,Fe,Si-ME-AS-2.5* | $SiO_2$ | 2.5 % Co<br>2.5 % Fe | Amorphous, mesoporous.<br>As synthesised. | 4.1.1.1 |
| *Fe,Ni,Si,Ti-ME-AS-2.5* | 50 % $SiO_2$<br>50 % $TiO_2$ | 2.5 % Fe<br>2.5 % Ni | Amorphous, mesoporous.<br>As synthesised. | 4.1.1.1 |
| *Fe,Ni,Ti-ME-AS-2.5* | $TiO_2$ | 2.5 % Fe<br>2.5 % Ni | Amorphous, mesoporous.<br>As synthesised. | 4.1.1.1 |
| *Fe,Ni,Si-ME-AS-2.5* | $SiO_2$ | 2.5 % Fe<br>2.5 % Ni | Amorphous, mesoporous.<br>As synthesised. | 4.1.1.1 |
| *Co,Ni,Si,Ti-ME-AS-2.5* | 50 % $SiO_2$<br>50 % $TiO_2$ | 2.5 % Co<br>2.5 % Ni | Amorphous, mesoporous.<br>As synthesised. | 4.1.1.1 |
| *Co,Ni,Ti-ME-AS-2.5* | $TiO_2$ | 2.5 % Co<br>2.5 % Ni | Amorphous, mesoporous.<br>As synthes ised. | 4.1.1.1 |
| *Co,Ni,Si-ME-AS-2.5* | $SiO_2$ | 2.5 % Co<br>2.5 % Ni | Amorphous, mesoporous.<br>As synthesised. | 4.1.1.1 |
| *Co,Fe,Si,Ti-ME-C-2.5* | 50 % $SiO_2$<br>50 % $TiO_2$ | 2.5 % Co<br>2.5 % Fe | Amorphous, mesoporous.<br>Calcined at 770 K | 4.1.1.1 |
| *Co,Fe,Ti-ME-C-2.5* | $TiO_2$ | 2.5 % Co<br>2.5 % Fe | Amorphous, mesoporous.<br>Calcined at 770 K | 4.1.1.1 |
| *Co,Fe,Si-ME-C-2.5* | $SiO_2$ | 2.5 % Co<br>2.5 % Fe | Amorphous, mesoporous.<br>Calcined at 770 K | 4.1.1.1 |
| *Fe,Ni,Si,Ti-ME-C-2.5* | 50 % $SiO_2$<br>50 % $TiO_2$ | 2.5 % Fe<br>2.5 % Ni | Amorphous, mesoporous.<br>Calcined at 770 K | 4.1.1.1 |
| *Fe,Ni,Ti-ME-C-2.5* | $TiO_2$ | 2.5 % Fe<br>2.5 % Ni | Amorphous, mesoporous.<br>Calcined at 770 K | 4.1.1.1 |
| *Fe,Ni,Si-ME-C-2.5* | $SiO_2$ | 2.5 % Fe<br>2.5 % Ni | Amorphous, mesoporous.<br>Calcined at 770 K | 4.1.1.1 |
| *Co,Ni,Si,Ti-ME-C-2.5* | 50 % $SiO_2$<br>50 % $TiO_2$ | 2.5 % Co<br>2.5 % Ni | Amorphous, mesoporous.<br>Calcined at 770 K | 4.1.1.1 |
| *Co,Ni,Ti-ME-C-2.5* | $TiO_2$ | 2.5 % Co<br>2.5 % Ni | Amorphous, mesoporous.<br>Calcined at 770 K | 4.1.1.1 |
| *Co,Ni,Si-ME-C-2.5* | $SiO_2$ | 2.5 % Co<br>2.5 % Ni | Amorphous, mesoporous.<br>Calcined at 770 K | 4.1.1.1 |
| "2.5% Co on silica" | $SiO_2$ | 2.5 % Co | Commercial $SiO_2$-60 from Acros Chemicals | 4.1.1.2 |
| "2.5% Co on alumina" | $Al_2O_3$ | 2.5 % Co | $Al(OH)_3$ obtained by hydrolysis of $Al(iOC_3H_7)_3$ | 4.1.1.2 |
| "2.5% Fe on alumina" | $Al_2O_3$ | 2.5 % Fe | $Al(OH)_3$ obtained by hydrolysis of $Al(iOC_3H_7)_3$ | 4.1.1.2 |
| "2.5% Ni on alumina" | $Al_2O_3$ | 2.5 % Ni | $Al(OH)_3$ obtained by hydrolysis of $Al(iOC_3H_7)_3$ | 4.1.1.2 |

Table 16. A summary of the materials mentioned in this thesis.

| Label | Matrix | Modifier | Properties | Mentioned in Section |
|---|---|---|---|---|
| *Co,Si-ME-C-5.0* | $SiO_2$ | 5 % Co | Amorphous, mesoporous. Calcined at 770 K | 4.1.1.2 |
| *Fe,Si-ME-C-5.0* | $SiO_2$ | 5 % Fe | Amorphous, mesoporous. Calcined at 770 K | 4.1.1.2 |
| *Ni,Si-ME-C-5.0* | $SiO_2$ | 5 % Ni | Amorphous, mesoporous. Calcined at 770 K | 4.1.1.2 |
| *Si-ME-C-0* | $SiO_2$ | — | Amorphous, mesoporous. Calcined at 723 K. | 4.1.2.1 |
| *PW12,Si-ME-AS-5* | $SiO_2$ | 5 % $H_3PW_{12}O_{40}$ | Amorphous, mesoporous. As-synthesised. Acid built in by sol-gel method. | 4.1.2.1 |
| *PW12,Si-ME-AS-20* | $SiO_2$ | 20 % $H_3PW_{12}O_{40}$ | Amorphous, mesoporous. As-synthesised. Acid built in by sol-gel method. | 4.1.2.1 |
| *PW12,Si-ME-AS-50* | $SiO_2$ | 50 % $H_3PW_{12}O_{40}$ | Amorphous, mesoporous. As-synthesised. Acid built in by sol-gel method. | 4.1.2.1 |
| *PW12,Si-ME-AS-80* | $SiO_2$ | 80 % $H_3PW_{12}O_{40}$ | Amorphous, mesoporous. As-synthesised. Acid built in by sol-gel method. | 4.1.2.1 |
| *PW12,Si-ME-C-5* | $SiO_2$ | 5 % $H_3PW_{12}O_{40}$ | Amorphous, mesoporous. Calcined at 873 K. | 4.1.2.1 |
| *PW12,Si-ME-C-20* | $SiO_2$ | 20 % $H_3PW_{12}O_{40}$ | Amorphous, mesoporous. Calcined at 873 K. | 4.1.2.1 |
| *PW12,Si-ME-C-50* | $SiO_2$ | 50 % $H_3PW_{12}O_{40}$ | Amorphous, mesoporous. Calcined at 873 K. | 4.1.2.1 |
| *PW12,Si-ME-C-80* | $SiO_2$ | 80 % $H_3PW_{12}O_{40}$ | Amorphous, mesoporous. Calcined at 873 K. | 4.1.2.1 |
| *PW12,Si-ME-IM-5* | $SiO_2$ | 5 % $H_3PW_{12}O_{40}$ | Amorphous, mesoporous. Dried at 313 K. Acid built in by wet impregnation. | 4.1.2.1 |
| *PW12,Si-ME-IM-20* | $SiO_2$ | 20 % $H_3PW_{12}O_{40}$ | Amorphous, mesoporous. Dried at 313 K. Acid built in by wet impregnation. | 4.1.2.1 |
| *PW12,Si-ME-IM-50* | $SiO_2$ | 50 % $H_3PW_{12}O_{40}$ | Amorphous, mesoporous. Dried at 313 K. Acid built in by wet impregnation. | 4.1.2.1 |
| *PW12,Si-ME-IM-80* | $SiO_2$ | 80 % $H_3PW_{12}O_{40}$ | Amorphous, mesoporous. Dried at 313 K. Acid built in by wet impregnation. | 4.1.2.1 |
| "pure PW12" | $H_3PW_{12}O_{40}$ | — | Commmercial, from Aldrich Chemicals. | 4.1.2.1 |
| *Al,Si-ME-C-20* | $SiO_2$ $Al_2O_3$ | Si/Al=20 | Amorphous, mesoporous. Sol-gel ref. material. Calcined at 873 K. | 4.1.2.3 |
| *Si-NT-C-0* | $SiO_2$ | — | Angular nanotube. Calcined at 773 K. | 4.2.1.1 |
| *PW12,Si-NT-C-5* | $SiO_2$ | 5 % $H_3PW_{12}O_{40}$ | Angular nanotube. Dried at 423 K. Acid built in by wet impregnation. | 4.2.1.2 |
| *PW12,Si-NT-C-20* | $SiO_2$ | 20 % $H_3PW_{12}O_{40}$ | Angular nanotube. Dried at 423 K. Acid built in by wet impregnation. | 4.2.1.2 |

Table 16. continued.

| Label | Matrix | Modifier | Properties | Mentioned in Section |
|---|---|---|---|---|
| Si-FO-AS-0 | $SiO_2$ | — | As-synthesised foam. Dried at 313 K. | 4.2.2.1 |
| Si-FO-C-0 | $SiO_2$ | — | Foam calcined at 673 K after drying at 313 K. | 4.2.2.1 |
| Si-FO-HTC-0 | $SiO_2$ | — | Foam calcined at 673 K after hydrothermal treatment at 413 K. | 4.2.2.1 |
| *PW12,Si-FO-C-5* | $SiO_2$ | 5 % $H_3PW_{12}O_{40}$ | Foam calcined at 673 K after drying at 313 K. | 4.2.2.2 |
| *PW12,Si-FO-HTC-5* | $SiO_2$ | 5 % $H_3PW_{12}O_{40}$ | Foam calcined at 673 K after hydrothermal treatment at 413 K. | 4.2.2.2 |
| *PW12,Si-FO-C-20* | $SiO_2$ | 20 % $H_3PW_{12}O_{40}$ | Foam calcined at 673 K after drying at 313 K. | 4.2.2.2 |
| *PW12,Si-FO-HTC-20* | $SiO_2$ | 20 % $H_3PW_{12}O_{40}$ | Foam calcined at 673 K after hydrothermal treatment at 413 K. | 4.2.2.2 |
| *Al,Si-FO-C-20* | $SiO_2$ $Al_2O_3$ | Si/Al=20 | Foam calcined at 673 K after drying at 313 K. | 4.2.2.2 |
| *Al,Si-FO-HTC-20* | $SiO_2$ $Al_2O_3$ | Si/Al=20 | Foam calcined at 673 K after hydrothermal treatment at 413 K. | 4.2.2.2 |
| *Al,Si-FO-C-5* | $SiO_2$ $Al_2O_3$ | Si/Al=5 | Foam calcined at 673 K after drying at 313 K. | 4.2.2.2 |
| *Al,Si-FO-HTC-5* | $SiO_2$ $Al_2O_3$ | Si/Al=5 | Foam calcined at 673 K after hydrothermal treatment at 413 K. | 4.2.2.2 |

Table 16. continued.